University of Dublin, Trinity College

Doctoral Thesis

Synthesis and applications of large-area graphene stacks

Author:

Christian Wirtz

Supervisor:

Prof. Georg S. Duesberg

A thesis submitted in fulfilment of the requirements for the degree of Doctor of Philosophy in Chemistry

in the

ASIN group

School of Chemistry

December 2015

Declaration of Authorship

I, Christian Wirtz, declare that this thesis, titled "Synthesis and applications of large-area graphene stacks", and the work presented in it are my own. I declare that:

- This work has not been previously submitted as an exercise for a degree at this or any other University.

- Where I have consulted the published work of others, this is always clearly attributed.

- Where the thesis is based on work done by myself jointly with others, I have made clear exactly what was done by others and what I have contributed myself.

- I agree to deposit this thesis in the University's open access institutional repository or allow the library to do so on my behalf, subject to Irish Copyright Legislation and Trinity College Library conditions of use and acknowledgement.

Signed:

Date:

Abstract

Doctor of Philosophy in Chemistry

Synthesis and applications of large-area graphene stacks

by Christian Wirtz

Research of two-dimensional nanomaterials has been significant since the discovery of graphene in 2004. Really one or few atoms thick but often micrometres in lateral size, these materials exhibit unique properties such as high mechanical strength, transparency, uncommon electric and thermal conductivity and previously unexplored quantum effects. Several hundreds of these materials have now been isolated.

This field of research is still very young and a lot of work has yet to be done to fully explore the properties of these materials to allow for their incorporation into new and existing technology. This thesis describes work performed in pursuit of that goal. The main focus was on graphene but some work was also done on MoS_2 and WS_2.

Firstly, a method for synthesising large areas of high-quality graphene was investigated. This was done by chemical vapour deposition from ethene. The method was optimised by statistical design and yielded a process at 850 °C, 200 °C lower than standard processes, that produced patterned monolayer graphene on copper with large sample size. The graphene films consisted of flakes approximately 1 μm in diameter, showed Raman signatures close to the ideal values and exhibited hole and electron mobilities of 1100 $cm^2V^{-1}s^{-1}$ and 700 $cm^2V^{-1}s^{-1}$, respectively. The reduced temperature allowed for better reproducibility and reduced cost.

Secondly, this graphene was used to fabricate effective oxygen gas diffusion barriers. In contrast to discouraging reports on large-area graphene coatings published

in the past, a modified stacking method allowed three layers of graphene (∼1 nm thick) to perform on par with 150 μm PET, a well-established barrier polymer. Its inherent barrier performance was 1.10×10^{-7} barrer which is equal to the standard coating materials SiO_2 and Al_2O_3 of that thickness. Its other extraordinary properties like conductivity, transparency and flexibility, should easily find applications, for example in organic light emitting diodes which require extremely good diffusion barriers that are transparent and ideally conduct electricity. In collaboration with Philips corporation, the graphene stacks were shown to outperform the industrial standard electrode ITO.

Further investigation towards functional stacks with 2D materials led to the discovery of signal enhancement in Raman scattering of graphene intercalated with perylene-based molecules. This effect had not been reported previously and though it can be consistently reproduced, its origins remain unclear.

Finally the processability of MoS_2 and WS_2 single crystal layers was investigated. A layer-dependent atomic layer deposition process was developed which allows for coverage of all layers except for the monolayer with Al_2O_3. This paves the way for vertical device structures that require the unique properties of the monolayer only. In addition, a reliable seeding mechanism via non-covalent functionalisation with perylene bisimides was developed for anchoring deposition even on the monolayer, providing a major step forward in the integration of two-dimensional materials in modern electronics.

Acknowledgements

There are many people who have helped me throughout my thesis, by scientific support or otherwise. Firstly, I thank Prof. Georg Duesberg for the opportunity to do a PhD in his research group, his support over the years, political insights into the workings of the university and CRANN and of course the funding provided through him by Science Foundation Ireland on a PI grant and the EU via the Grafol project. I joined the group in September 2011 and am certain I made an excellent choice.

Many of the group members provided me with instructions and guidance over the years for which I am very thankful. These are especially Drs. Toby Hallam, Niall McEvoy, Nina Berner, Kangho Lee, Hugo Nolan, Chanyoung Yim and Ravi Joshi. Their expertise on many topics and knowledge of equipment provided much help in challenging times. Also Chris Murray, Intel RiR, has to be mentioned here for his help, especially in terms of equipment training.

Other people from the group and schools of chemistry and physics who have my gratitude for scientific and other help include Dr. Hye-Young Kim, Ehsan Rezvanie, Maria O'Brien, Sinéad Winters, Riley Gatensby, Sarah Hurch, Trevor Woods as well as members of the AML and CRANN staff.

On the social side the group has to be commended for the extreme engagement, especially Niall McEvoy for pushing karaoke nights, Toby Hallam and Nina Berner for the regular parties at their house and Maria O'Brien and Hugo Nolan for random entertaining conversations and bitching.

The people who shared my office over the years also deserve to be mentioned as they made the four years very entertaining. That also counts for the people who usually meet for lunch in the breakout area, including many people from my group and office as well as Brendan O'Dowd, Hugh Manning, Sam Torsney, Shaun Mills and Stephen Connaughton, who provided much humour over the years.

The social aspect of this work was very important to me so I also thank those who organised the school of chemistry weekly basketball meet and summer tag rugby team: Niamh Fox, Beth Kelly, Michelle Browne and many others.

The university water polo team needs to get an honourable mention for keeping me sane and giving me a very efficient and legal method for letting off steam and frustration that may have built up over failed experiments.

Finally, there is my family who always supported me. My parents, Kirsten and Conny, who always encouraged me to pursue the education I desire even though it meant permanently leaving home at age 17. I think I will only really understand their sacrifice once I have a family of my own. My sister Sarah, my brother Daniel, my brother-in-law Markus, and my grandmother Evi, who always made sure there were plenty of entertaining things going on in the family. And my second family here in Dublin, Sive and her family, who have made me feel very much at home in this city.

ASIN group, March 2015. Front row: Kay Lee, Hye-Young Kim, Sinéad Winters, Maria O'Brien, Niall McEvoy, Kim Dümbgen, Chanyoung Yim. Middle row: Hugo Nolan, Chris Murray, Georg Duesberg, Ehsan Rezvanie, Christian Wirtz. Back row: Riley Gatensby, Nina Berner, Toby Hallam

Contents

Abbreviations

AFM	**A**tomic **F**orce **M**icroscopy
ALD	**A**tomic **L**ayer **D**eposition
APCVD	**A**tmospheric **P**ressure **C**hemical **V**apour **D**eposition
CAB	**C**ellulose **A**cetate **B**utyrate
CM	**C**hemical **M**echanism
CMOS	**C**omplementary **M**etal-**O**xide-**S**emiconductor
CVD	**C**hemical **V**apour **D**eposition
DoE	**D**esign **o**f **E**xperiment
DOS	**D**ensity **O**f **S**tates
EM	**E**lectromagnetic **M**echanism
FET	**F**ield **E**ffect **T**ransistor
FWHM	**F**ull **W**idth at **H**alf **M**aximum
GERS	**G**raphene **E**nhanced **R**aman **S**cattering
HOMO	**H**ighest **O**ccupied **M**olecular **O**rbital
HOPG	**H**ighly **O**riented **P**yrolytic **G**raphite
HPLC	**H**igh **P**erformance **L**iquid **C**hromatography
IPA	**I**so-**P**ropyl **A**lcohol
ITO	**I**ndium **T**in **O**xide
LED	**L**ight **E**mitting **D**iode
LPCVD	**L**ow **P**ressure **C**hemical **V**apour **D**eposition
LUMO	**L**owest **U**noccupied **M**olecular **O**rbital
OLED	**O**rganic **L**ight **E**mitting **D**iode
PECVD	**P**lasma **E**nhanced **C**hemical **V**apour **D**eposition
PET	**P**oly (**E**thylene **T**erephthalate)

PMMA	**P**oly (**M**ethyl **M**eth**a**crylate)
SEM	**S**canning **E**lectron **M**icroscopy
SERS	**S**urface **E**nhanced **R**aman **S**cattering
TEM	**T**ransmission **E**lectron **M**icroscopy
TMA	**T**ri **M**ethyl **A**luminium
TMD	**T**ransition **M**etal **D**ichalcogenide
UV	**U**ltra **V**iolet
XPS	**X**-ray **P**hotoelectron **S**pectroscopy

Chapter 1

Introduction to materials

This chapter serves as general introduction to the materials used and investigated in this thesis. The main focus lies with graphene which is used for the work outlined in chapters 3, 4 and 5. Other materials like MoS_2 (chapter 6) and perylene bisimides (chapters 5 and 6) are also described.

1.1 Graphene and few-layered graphite

Graphene is the "miracle material" of the last decade.[1] It consists of a sheet of carbon atoms arranged in a hexagonal honeycomb lattice, shown in figure 1.1. Used as a model by theoreticians for the last 60 years, it was experimentally isolated for the first time in 2004 by André Geim and Konstantin Novoselov.[2–4] Their work on "groundbreaking experiments regarding the two-dimensional material graphene" was awarded the Nobel Prize in physics in 2010.[5]

There are many properties that give graphene the special place it holds in current scientific research: Its electronic properties make it the best electronic and thermal conductor useful to man, all while retaining optical transparency.[6–8] It is also mechanically extremely strong and yet highly flexible.[9] It exhibits an unusual quantum hall effect and its structure, which places all atoms at the surface, allows for extremely strong electrostatic doping.[10,11] That also means it is an extremely

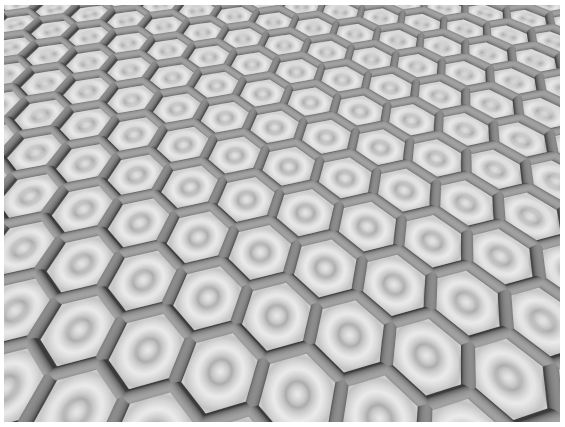

FIGURE 1.1: Representation of the honeycomb structure of graphene

good material for sensing applications to the point that individual molecules have been sensed with graphene.[12,13]

With only two instead of three spatial degrees of freedom, its electronic structure is remarkably different from that of any three-dimensional material. Its energy surface takes the form of six double-cones that have a linear dispersion close to the intersection point (Dirac point) at which the Fermi energy lies, as shown in figure 1.2. Even several eV from the Dirac point the dispersion is still linear. As the effective mass of charge-carriers is inversely proportional to the curvature of the bands and this curvature is extremely high at the Dirac point, the effective mass goes close to zero in this regime, making all charge carriers near-massless Dirac fermions near the Fermi energy.[10]

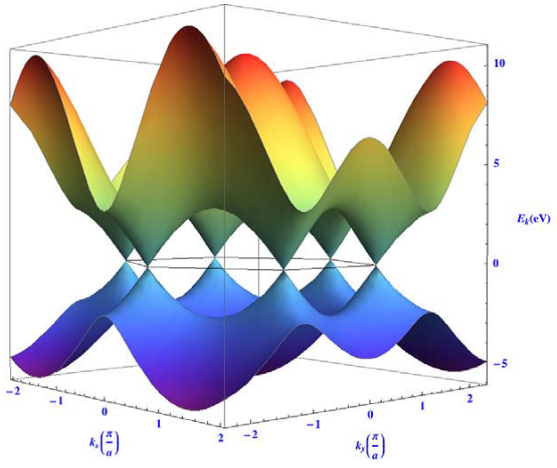

FIGURE 1.2: Graphical representation of the energy surface of undoped graphene. The black ring represents the Fermi energy at the so-called Dirac point where the density of states is zero. Taken from[5]

With such low mass the electron mobility in graphene is theoretically limited to about 200,000 $cm^2V^{-1}s^{-1}$ and results in a theoretical sheet resistance of 31 Ω/sq. which is better than even copper at room temperature. However, it is not possible to achieve both this moblility and sheet resistance at once as the theoretical sheet resistance assumes contribution from all charge carriers which will in turn reduce the mobility due to charge-carrier interactions. In addition to this excellent electrical conductivity the highly regular lattice allows for high phonon mobility and therefore thermal conductivity close to 5000 $Wm^{-1}K^{-1}$ has been measured.[7]

Even though graphene has such high mobility and excellent conductivity, it is still 97.7 % transparent to light.[8] That is due to the very short optical path available for electron-photon interaction and makes it a very good candidate for applications in transparent conductors.

The electronic structure of graphene also leads to an effect that may not immediately be associated with electronics: The graphene hexagons have a diameter of 2.84 Å which should easily allow for helium atoms of typical diameter 0.98 Å to pass through the centre of the ring. However, the arrangement of the electron density in graphene leads to the circumstance that even helium cannot pass through the ring centre and thus pristine graphene is completely impermeable to any material whatsoever.[14]

Finally graphene, like several other carbon materials, is mechanically very strong. The strength of a monolayer of graphene is about 42 Nm^{-1}. That would allow a 1 m^2 sheet of graphene, weighing 0.77 mg, to freely support a mass of about 4 kg.[9] Whether these numbers will ever be attained remains subject of speculation.

1.1.1 Graphene applications

With such a wide range of extraordinary properties it is easy to see that there are many potential applications for graphene. Its mechanical strength combined with low mass makes it an excellent candidate for reinforcing materials polymers. The high surface to volume ratio makes it an excellent sensor for all kinds of analytes,

from gas molecules to biological species after adequate functionalisation. High charge-carrier mobilities allow for the production of ultrafast electrical devices which gets really interesting when graphene's flexibility is also exploited. Combining this with its impermeability to gases and transparency makes it an ideal candidate for devices like OLEDs which require a transparent electrode and protection from oxygen and moisture. Transparent, flexible, bio-compatible electrodes are of huge interest for neural research which is a field with a lot of potential. A modified graphene surface can lead to some very interesting electrochemistry and a huge area of research is in supercapacitors.[15–19]

1.1.2 Methods of obtaining graphene

All these future applications mean the demand for graphene will be significant. However, obtaining high-quality graphene cheaply remains a challenge that has to be surmounted before it can find any use in industrial and commercial applications. Several methods of production are known but none of them manage to yield perfect graphene in large-area, easy to handle, affordable quantities. Depending on the desired application, it is not necessary to preserve all properties. Several important production methods are listed below.

1.1.2.1 Mechanical exfoliation

The simplest method of obtaining graphene, used by Geim and Novoselov, is the so-called "scotch-tape" method.[3] It is a mechanical cleavage technique that involves the use of adhesive tape to thin down layers of graphite, graphene's 3D structure, until only one layer is left. It is advantageous to start with high quality starting material so a good HOPG crystal is normally utilised. This thinning process gives a wide variety of graphite flake thicknesses and somewhere among them are some pristine monolayer graphene flakes. They are a few microns in size and exhibit most, if not all, of graphene's extraordinary properties. For obvious reasons the

throughput for this method is so small that it can only provide individual small samples for research.

1.1.2.2 Sublimation of silicon carbide

A completely different method is the sublimation of solid SiC.[20,21] This material has a diamond-like tetragonal structure with Si and C atoms. In certain crystal directions it therefore has a structure made of alternating layers of Si and C. It was shown early in graphene reasearch that when heated to very high temperatures of $>1100\ ^{\circ}C$ under very low pressure ($\sim 10^{-6}$ mbar), graphene will form out of the bulk as a Si layer is evaporated. Emtsev *et al.* showed that this graphene's properties are highly dependent on the crystal face of SiC from which it precipitates.[22] This technique is often difficult to stop once monolayer graphene has been obtained and multilayers are frequently formed. When monolayers are produced they often exhibit many of the ideal properties of graphene and a lot of these properties were first experimentally measured on samples obtained by this method. Later, Emtsev *et al.* also developed an atmospheric pressure synthesis.[23] It is technically upscalable and can theoretically be integrated into existing microelectronic processing. However, high quality SiC is very expensive as a 4" wafer costs several thousand euro, making it a costly technique.

1.1.2.3 Molecular self-assembly

Another potentially upscalable, but currently very expensive method, is molecular surface self-assembly.[24] Small precursor molecules are deposited on a surface and naturally arrange into a favourable pattern. They are subsequently polymerised to give graphene-like structures. This technique does not readily yield graphene sheets yet but can make nanoribbons which are only a few nm wide but hundreds of nm long.

1.1.2.4 Liquid exfoliation & reduced graphene oxide

A method that yields smaller and potentially more defective graphene than any other one mentioned so far, but does so in huge quantities, is liquid exfoliation by physical processes.[25–27] It involves dispersing large quantities of graphite, usually in powder form, in a solvent or surfactant stabilised aqueous medium and applying vast amounts of sonic or shear energy. This method is quick, upscalable and yields solutions with tens of mg/ml graphene in liquid which makes it useful for applications like polymer reinforcement.[28] However, the exfoliation process is never complete, so the average flake thickness in these dispersions is commonly around 4-6 layers. Also the flakes themselves often get damaged and shredded to small, sub-micron dimensions with their electronic properties heavily diminished. Removing solvent and surfactant residues for further processing is also not trivial.

A different liquid exfoliation process is by chemical means. Graphene is not well-soluble in any solvent as such but can be chemically modified to change that. This is achieved by converting it to graphene oxide with strong oxidising agents like $KMnO_4$.[29–32] Graphene oxide is graphene with many hydroxyl, carboxyl, keto or carboxylic acid groups attached to it. They rend it electrically insulating but this graphene oxide can be dispersed and dissolved in water to yield individual graphene oxide flakes which can be implemented in desired applications. The flakes can then be reduced with strong reducing agents to yield a form of graphene called "reduced graphene oxide" (rGO). This method has high throughput and is very cheap but the aggressive chemical treatments leave the graphene defective and with several percent functional groups after reduction.

1.1.2.5 Chemical vapour deposition

Finally, there is synthesis via chemical vapour deposition.[33–40] This technique has seen a lot of attention as it is easily upscalable and gives high-quality graphene compared to the liquid exfoliation techniques but is still inferior to mechanical cleavage. In essence, this technique works by passing carbon-containing gaseous

species over a substrate at high temperatures (∼1000 °C) and low pressures (<10 mbar). Depending on the process conditions like temperature, pressure, carbon precursor and substrate, the deposition can give layers of perfect graphene, multi-layer graphene or highly disoriented nanocrystalline graphene stacks. The largest graphene flakes reported from this process are up to mm in size. All the graphene used in the pursuit of this project was synthesised using a CVD process. Chapter 3 explains this process in detail.

1.2 Transition metal dichalcogenides

In recent years graphene has not been the only layered, 2D material, to get significant attention. Other layered materials have attracted a lot of attention, among which the transition metal dichalcogenides (TMDs) are most notable.[41] Their basic structure is MX_2, where M is a transition metal (often Mo, W, Re, Ta, Nb) which is sandwiched between two layers of X, a chalcogen (S, Se, Te). This is shown in figure 1.3. Just like graphene, these materials exhibit very different properties in a single layer or few-layer arrangement compared to when they are in their bulk form.[42–46] Most are semiconductors rather than metallic. Even individual materials may have several crystal structures which have different properties. For example, in MoS_2 the 2H phase is semiconducting but the 1T phase is metallic.[47] Also chalcogen deficiencies can lead to different band structures and ensuring consistent stoichiometry is a significant challenge in this field. These semiconducting properties makes TMDs even more valuable than graphene in some aspects as their semiconducting properties mean they can be used for logic computing which is almost impossible with the zero-bandgap semiconductor graphene as its on-off current ratio is too small. Some TMDs are inherently n-type semiconductors and some p-type, so together with graphene as metal, they provide the full toolset required for CMOS electronics.[48] Many methods for fabricating graphene, like mechanical or liquid exfoliation and CVD can be applied to TMDs.

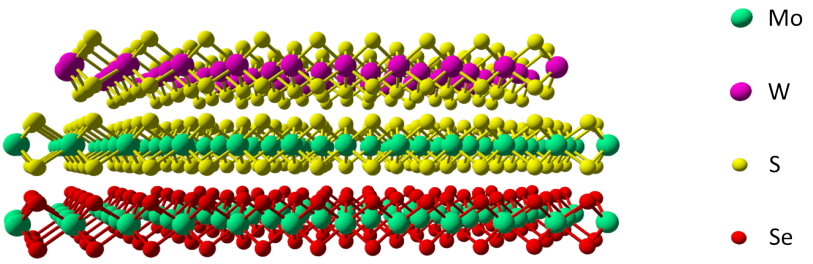

FIGURE 1.3: Ball-and-stick model representation of some transition metal dichalcogenides. The transition metal is sandwiched between two chalcogens. Even though they are all structurally similar and often even share some elements, each TMD is different and its properties may differ significantly even from its closest relative.

1.2.1 MoS_2 and WS_2

MoS_2 and WS_2 are two TMDs that were among the earliest ones studied. They are readily obtainable, either by exfoliation from ore or from chemical synthesis.[49–52] Hence, much of the knowledge in the young field of 2D TMDs comes from studying these two materials. One of their features is that, while bulk MoS_2 and WS_2 are indirect bandgap semiconductors, the monolayer has a direct bandgap, leading to many interesting electronic and optical effects. The reason for this change from indirect to direct bandgap was explained by Splendiani *et al.* and their calculated band structures for perfect MoS_2 are shown in figure 1.4.[53]

The optical bandgap changes from 1.2eV and 1.3eV to 1.9eV and 2.0eV for MoS_2 and WS_2, respectively, upon reducing them to monolayers. A direct bandgap has immediate effects on their optical properties as it allows for strong photoluminescence which is heavily suppressed by an indirect gap. That makes these materials interesting for applications like LEDs, optical sensors and solar cells.[54–56] Even in the few-layer limit there are some interesting optical properties as there is significant exciton confinement up to 5-6 layers. The basal plane, like that of graphene, does not have any dangling bonds and is therefore chemically inert except for at the edges which can be a huge advantage for device stability.

A major application currently investigated for MoS_2 and WS_2 are electronic circuits. The flat structure and semiconducting electronic properties are ideal for integration into integrated circuit technology. Their uniformity and lack of basal

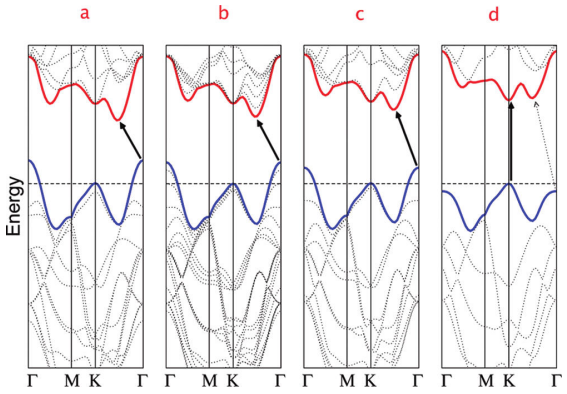

FIGURE 1.4: Theoretically calculated electronic band structure of MoS_2. a) The band structure of bulk MoS_2; b) the band structure of quadlayer MoS_2; c) the band structure of bilayer MoS_2 and d) the band structure of monolayer MoS_2. Blue is the valence band edge and red the conduction band edge. The black arrow indicates the lowest energy transition for exciting an electron from the valence to the conduction band. In the bulk the indirect transition is much smaller in energy than any direct transitions but as the layer number is reduced the indirect transition becomes larger whereas the direct one stays the same. For the monolayer case the indirect transition requires more energy than the direct one. Taken from [53]

plane reactivity helps avoid short-channel effects which are becoming a severe problem in extremely small silicon-based transistors as silicon-doping statistics do not apply any more at those length scales. That of requires the right contact metal in order to make ohmic contacts rather than schottky contacts. A promising candidate for this is scandium.[57] Like any other semiconductor, TMDs become very interesting when doped. Using adsorbate-enabled doping, full logic circuits have been demonstrated on single flakes of WSe_2.[58]

Similarly to graphene, monolayer TMDs are very good sensing materials due to their extremely high surface to volume ratio. Their semiconducting properties potentially make them more sensitive as their response to doping from analytes is exponential rather than linear, as it is for graphene. Extremely high sensitivities have been demonstrated.[59,60]

1.3 Perylene bisimides

Perylene is a polycyclic aromatic hydrocarbon with the chemical formula $C_{20}H_{12}$. A bisimide version of perylene exists and has been heavily researched by Andreas Hirsch's group in the university of Erlangen-Nürnberg.[61] Their derivatives of these molecules contain a perylene bisimide core and variable functional end-groups, as shown in figure 1.5. Originally developed for carbon nanotube exfoliation, those molecules can also be used for the exfoliation and functionalisation of graphene and TMDs.[62–65]

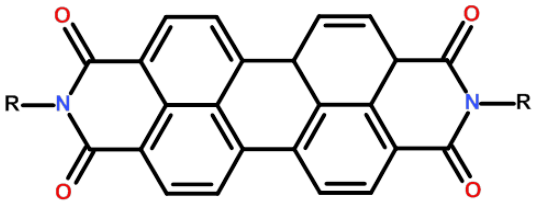

FIGURE 1.5: Moleculare structure of perylene bisimide. The end-groups, denoted by "R", can be varied to give the molecule different properties.

These perylene derivatives work very well at exfoliating and functionalising low-dimensional materials because the seven-ringed perylene bisimide core can non-covalently adsorb onto the surface of the 2D material and the end-groups can be modified to give specific properties. The non-covalent functionalisation does not disturb the underlying lattice but can lead to electronic doping. Modifying the end-groups allows for attachment of selective chemical species which may be used for specific and selective sensing. Alternatively, they can contain groups that enhance solubility in certain solvents, hence making them an effective surfactant. They can be very easily detected by Raman spectroscopy as they have some very intense characteristic peaks which are also enhanced by contact with graphene and TMDs (see section 2.5.5).[61]

Chapter 2

Theoretical and experimental background to experimental and analytical techniques

This chapter gives general information about the theory behind many of the experimental methods used in research for this thesis and gives the general experimental conditions for standard processes.

2.1 Material procurement

All chemicals were purchased from Sigma-Aldrich and used as-received unless specified otherwise. Aqueous solutions were made using millipore water (18.2 MΩ) from a Barnstead Nanopure system fed by deionised water. Polished Si(001) wafers of thickness 545 μm were purchased from Si-Mat and Dasom RMS. Those with oxide had 300 nm polished dry thermal SiO_2 coatings. All gases were purchased from BOC Gases except for N5-grade nitrogen and hydrogen, which was supplied in-house by a DALCO N_2 generator and a Schmidlin PG-250 H_2 generator respectively. Cu foils (18-25 μm, 99.99 %) were kindly provided by Gould Electronics GmbH (liquidated Dec. 2014).

2.2 Chemical vapour deposition

Chemical vapour deposition is a very prominent technique for depositing thin-films of materials in both research and industrial settings.[66] It has many advantages over other deposition techniques, namely uniformity, conformity, adhesion, compositional stoichiometry, low defect levels and low cost with scalability. Several types of CVD exist and the most common ones are atmospheric-pressure CVD (APCVD), low-pressure CVD (LPCVD), plasma-enhanced CVD (PECVD) and atomic layer deposition (ALD). There are arguments that put ALD separate from CVD but in this dissertation it is included in this section for convenience.

In principle, all CVD processes operate in a similar fashion: Gaseous precursor materials enter the CVD chamber, often at elevated temperatures, and decompose or react to deposit on the desired substrate, possibly via an intermediate species. The material is deposited directly onto the substrate, with speed and conformity determined by the exact conditions. The different types of CVD describe the conditions, as detailed below:

APCVD takes place at atmospheric pressures. The molecular mean free path is very short and the exposure very high. This can lead to excellent coverage with high deposition rates but also requires high gas flows. A major advantage is the avoidance of vacuum equipment and short chamber preparation time.

LPCVD is similar but takes place at reduced pressures, commonly <1 mbar. Therefore the molecular free path is much longer and the overall flow regime somewhere between viscous and molecular flow, depending on the specific system. The reaction is often slower and can be more controlled than in APCVD, leading to less defects and better conformity but often lower uniformity. Both LPCVD and APCVD commonly take place at elevated temperatures, anything between 300 °C and 1100 °C. This can be very expensive and create environments unsuitable for many substrates. The different thermal expansion coefficients of the materials involved can also cause buckling and cracking upon cooling, something best avoided if at all possible.

To avoid such high temperatures, PECVD can be used. In this process the molecules do not gain their reactivity due to thermal energy as much as plasma energy. Energising molecules that way leads to very high rates of reaction and often produces non-stoichiometric films with high defect densities that deposit in a non-conformal manner. These may not be suitable for high-performance applications.

A material that can be produced using all these methods is Si_3N_4 for example, although the precursors, product quality and reaction rates can be vastly different.

APCVD: $SiH_4 + 4\,NH_3 \xrightarrow{700°C\text{ - }900°C} Si_3N_4 + 12\,H_2$

LPCVD: $3\,SiCl_2H_2 + 4\,NH_3 \xrightarrow{700°C\text{ - }800°C} Si_3N_4 + 6\,HCl + 6\,H_2$

PECVD: $3\,SiH_4 + 2\,N_2 \xrightarrow{\text{plasma energy}} Si_3N_4 + 6\,H_2$

ALD is different from these techniques in that only one of two or more complimentary precursors is flowed through the reactor at any given time. The growth substrate is exposed to cycles of different precursors, each reacting with the surface groups left by the previous precursor's exposure. This yields a highly conformal, low defect film but has an extremely slow growth rate as the chamber has to be fully evacuated after each exposure. That also allows the reaction to be stopped at any given time, giving ultimate control, potentially down to a monolayer of the material deposited. One of the best known and most studied ALD reactions is the deposition of Al_2O_3 which is illustrated in figure 2.1. This reaction is commonly done with Tri-Methyl Aluminium (TMA, $Al(CH_3)_3$) and H_2O or O_3 according to the scheme:

$2\,Al(CH_3)_3 + 3\,H_2O \longrightarrow Al_2O_3 + 6\,CH_4$

This is only one example of a very wide range of industrially-used ALD reactions.

ALD of Al_2O_3 is used at several stages during this dissertation. It was performed in a custom-built cold-walled thermal processing tool from ATV technology GmbH. Growth took place at 80-200 °C and utilised $Al(CH_3)_3$ (TMA) procured from Sigma-Aldrich High Tech and H_2O. Growth took place at 2 mbar chamber pressure

with constant nitrogen flow at 60 sccm. Each growth cycle consisted of 0.5 s TMA at 5 sccm, 20 s N_2 flush, 0.7 s H_2O at 5 sccm and another 20 s N_2 flush.

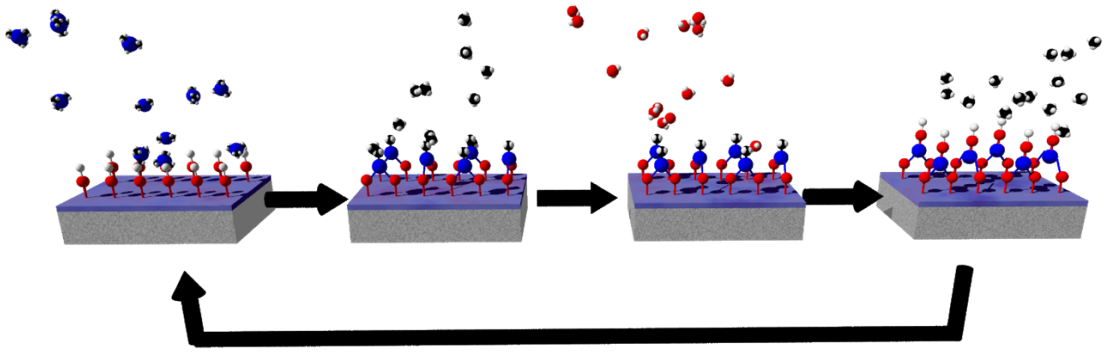

FIGURE 2.1: Schematic representation of Al_2O_3 ALD from TMA and water. TMA is introduced into the chamber and reacts with -OH groups, forming Al-O bonds and releasing methane. This reaction is self-limiting as it stops once all reaction sites are gone. The chamber is emptied and water is introduced, reacting with the unreacted parts of the TMA, releasing methane again. This forms new -OH species attached to the Al atoms and the cycle can be started again.

2.2.1 CVD of graphene

The chemical vapour deposition of graphene is a very popular method of graphene production for device applications.[33–40] The CVD of graphene came about soon after the first isolation of graphene and works by thermally and/or catalytically decomposing carbon-rich gases on metal catalysts (though there are some reports of growth on insulators), usually in a LPCVD setting. Many metals can decompose carbon-rich gases at high temperatures (∼1000 °C). Indeed, some gases like acetylene do not require a catalyst to decompose but deposit mixtures of graphitic carbon species when heated. A general schematic of the different surface processes occurring during graphene growth is shown in figure 2.2.

Initially the catalysts used were Ir(111) or Pt(111) as they yield excellent graphene due to surface structures that match graphene's hexagonal structure and their catalytic activity.[37,67] Ni is very popular as well because it is catalytically active enough to decompose the carbon-containing gases into graphitic sheets on

its surface while being much cheaper than any of the other good catalysts.[34,68,69] However, it has a high carbon solubility at elevated temperatures, leading to significant carbon precipitation upon cooling, forming multi-layers. These multi-layered structures are still useful for some applications but only with a lot of effort is it possible to produce monolayer graphene on Ni.[70,71] The material that most research is now concentrated on is Cu. In contrast to Ni it has very low carbon solubility, even close to its melting temperature of ∼1085 °C.[72] Its crystal structure and catalytic activity are not as suitable as that of Ni so it is more difficult to initiate graphene growth but it is much easier to produce monolayer graphene on Cu than on Ni. Combined with the low cost of acquiring high-quality Cu it is probably the best catalytic candidate for large-scale graphene CVD. Early processes of graphene CVD on Cu took place at 1050 °C with a mixture of methane and hydrogen as carbon feedstock.[35] Much work has since been done on this subject and a much wider spectrum of precursors has been investigated, the Cu foil surface optimised, and the temperature reduced.[73–82] Chapter 3 of this dissertation describes the results of one such investigation.

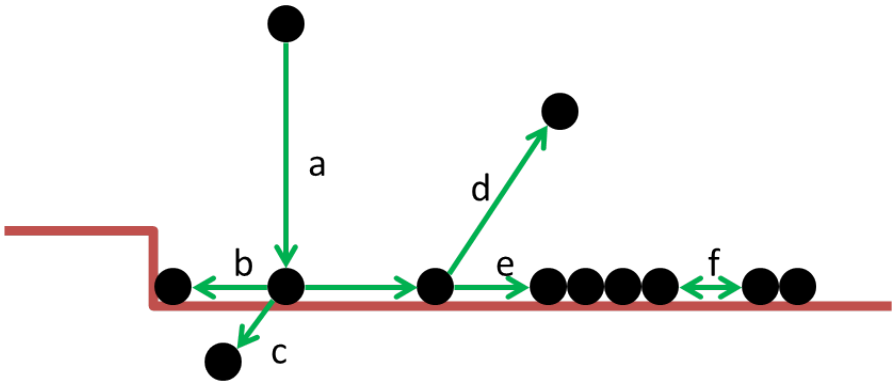

FIGURE 2.2: General carbon deposition: a) incoming carbon-containing radical adsorbs onto the catalytic surface; it diffuses until it b) gets stuck at a surface feature, c) dissolves into the bulk substrate, d) desorbs or e) encounters and joins a stable island; f) islands merge if they encounter each other and are crystallographically compatible

2.3 Graphene transfer to arbitrary substrates

All graphene used in the pursuit of this dissertation was grown by CVD on copper foils. In order to fabricate anything useful from this kind of graphene it had to be transferred from its Cu growth substrate to the desired application substrate. For example, a transistor requires the graphene to be on an insulating substrate and Raman spectroscopy gives much clearer signals if the graphene is on a 300 nm Si/SiO_2 substrate. Therefore techniques have been developed to achieve relatively defect-free transfers of large graphene areas from the growth substrate to the final one. The one used exclusively in this study is polymer-assisted transfer. Originally presented by Reina *et al.* on Ni and subsequently by Suk *et al.* for Cu, it was optimised for this thesis work by Dr. Toby Hallam.[69,83–85] It involves several steps: Firstly, the graphene is pre-cleaned while still on Cu. This is necessary as the cooling process inside the furnace leaves various physisorbed carbon species on the surface. These contaminate the surface and can act as anchors for dirt and polymer residues. The cleaning is a short, mild sonication in HPLC acetone followed by a rinse with IPA.

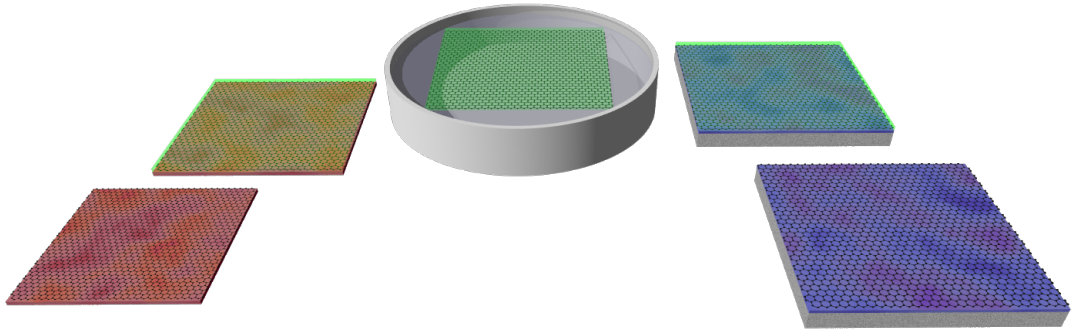

FIGURE 2.3: Schematic representation of polymer-assisted graphene transfer. From left to right: Graphene as grown by CVD on Cu is covered with a handling polymer. This is transferred to an etchant solution where the Cu dissolves and the graphene-polymer film remains. That film is dredged onto the substrate of choice where it dries and adheres. Finally the polymer is dissolved.

Secondly, the graphene is covered with the transfer polymer of choice. This is done by spin-coating a low concentration polymer solution onto the graphene. Common

options are 2 % PMMA in anisole or 3 % cellulose acetate butyrate in ethyl-L-lactate, spun on at a speed of several 1000 rpm. The polymer thickness tends to be in the region of 100s of nanometres. To ensure there is as little strain as possible in the polymer film it is re-flowed above its glass transition temperature for a short amount of time. The strain may have arisen from imperfect spin-coating and the heating step lets the polymer flow and removes any remaining solvent. The copper growth substrate is then wet-etched and the polymer film with graphene beneath it remains floating on the etching solution. It can then be fished out with the final substrate, usually after transfer to a water bath to remove excess etchant. Finally, the polymer is removed by dissolution and the graphene remains on the final substrate. This overall transfer is usually done over the period of several hours but can be done in less than one hour if necessary.

For all experiments performed in pursuit of this work graphene was transferred using either poly(methyl methacrylate) 960 k (molecular weight 960,000 g/mol) or cellulose acetate 65 k. They were respectively dissolved in anisole and ethyl-L-lactate to make 3 % w/V solutions. The solutions were spin-coated onto graphene on copper at 3000 rpm for 60 s followed by 1000 rpm for 60 s. Subsequently the polymers were re-flowed at ∼160 °C for 5 minutes. The copper substrate was dissolved in 1 M $(NH_4)_2S_2O_8$ and the remaining film transferred to water. It was then dredged onto the final substrate and let dry in air. The polymer was removed with HPLC grade acetone and propan-2-ol.

2.4 Photolithography

Photolithography ("writing with light") is a technique widely employed by the microprocessing industry. It is a very reliable, fast and cheap method of repeatedly transferring a given pattern from a mask to a substrate.[66] The advanced optics used lead to parallel light beams uniformly treating the substrate which minimises spatial differences.

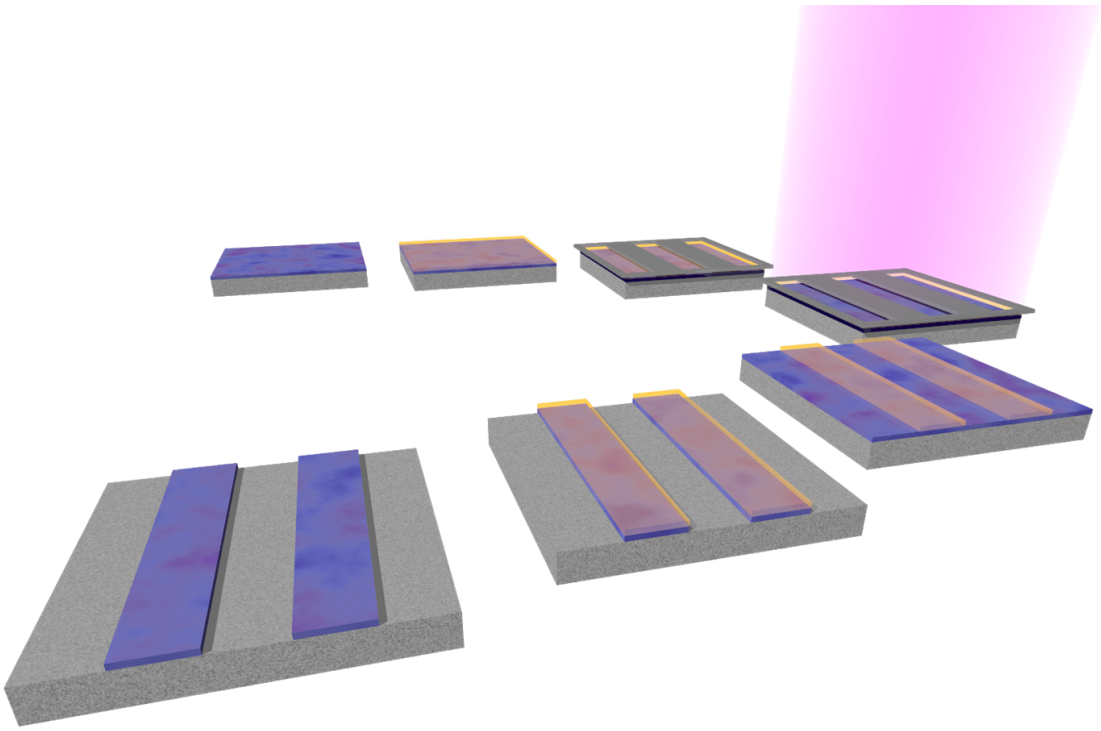

FIGURE 2.4: General principles of photolithography, shown for Si/SiO_2 patterning (from back to front): A silicon substrate with oxide is covered with photoresist. A mask with the desired pattern is put on top. This assembly is exposed to UV light, selectively altering the photoresist. This is then dissolved (in this case the resist is positive) to leave the transferred pattern behind. The remaining photoresist acts as etch mask against the HF used to etch SiO_2 and is removed once all etching is done.

In general, the substrate to be patterned is covered with a thin layer of photosensitive chemical, the so-called photoresist. An optical mask with a pre-defined pattern defined in Cr is then put between the substrate and a light source. The areas where the photoresist is exposed to light are chemically altered and gain properties that differ from the unexposed parts. Commonly solubility with respect to certain solvents is altered upon exposure, allowing for one part to be removed by dissolution while the other one remains. This pattern can then be used to selectively etch the underlying substrate or deposit material. Conventionally a resist is called "positive" if the exposed area is removed and "negative" if the exposed area remains behind. Depending on the feature size desired, the wavelength of light used as well as the chemicals utilised have to be adjusted but the principle stays the same regardless of what is being made.

Standard photolithography uses near UV light (400 nm - 300 nm) but many industrial processes use up to extreme UV light (121 nm - 10 nm) in liquid with high refractive index to make the wavelength, and hence the resolution, as short and small as possible. The photoresist often consists of monomers that are polymerised under UV light or polymers that decompose under UV light.

2.5 Raman spectroscopy

2.5.1 General Raman scattering

Raman spectroscopy has recently become an extremely powerful technique for material characterisation. It non-destructively probes certain vibrational levels of molecules and crystals, yielding significant amounts of information about their structure.[86] First observed in the late 1920s, its discovery was awarded the Nobel Prize in physics in 1930. Initially rather awkward to use, it required the development of lasers (1960s), notch filters, and fast CCD light detectors (Nobel Prize 2009) to make it the standard laboratory technique it is nowadays.

The principle working is that of inelastic light scattering processes. When a photon excites an electron and promotes it to a higher energy level, the electron usually relaxes within a given amount of time, re-emitting the photon. This is called elastic scattering as the photon energy does not change but its direction of travel may. It is also known as *Rayleigh Scattering* after its discoverer, Lord Rayleigh. Occasionally (about 1 in 10^7), the electron may emit or absorb a phonon to or from its host lattice just before re-emitting the photon, thereby decreasing or increasing the photon's energy, respectively. The case where a phonon is emitted is called *Stokes Scattering* and the case in which a phonon is absorbed *Anti-Stokes Scattering*, both shown in figure 2.5. The phonon can be emitted/absorbed either before or after the photon.

There are several conditions that have to be met in order to observe Raman scattering effects. The most important one is the nature of the phonon involved.

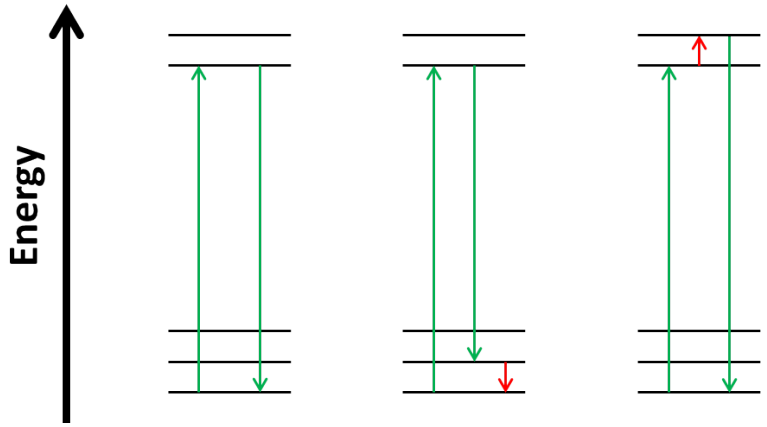

FIGURE 2.5: Representation of different processes possible when light interacts with a molecule. From left to right: The most common possible process is *Rayleigh Scattering* during which an electron gets excited by absorbing a photon (green) and re-emits the same photon upon relaxation. *Stokes Scattering*, the second case here, involves emission of both a photon and a phonon(red) upon relaxation. *Anti-Stokes Scattering* occurs when a phonon is already present in the system and adds its energy to the photon.

It is only "Raman active" if the phonon causes a change in polarisability. This is opposed to phonons that involve a change in dipole moment which are IR active. The different phonons are explained here by the modes of CO_2, shown in figure 2.6. CO_2 has four vibrational modes: A symmetrical stretch, an asymmetrical stretch and two degenerate bending modes. The carbon atom is polarised and hence carries a $\delta+$ charge and the oxygen atoms have a $\delta-$ charge but there is no net dipole due to the molecule's symmetry. However, the asymmetrical stretching and the two bending modes cause a disturbance in the symmetry and give rise to a temporary net dipole moment. Hence those modes are IR active but not Raman active. The symmetrical stretching mode does not give rise to a change in dipole moment but to a change in polarisability. It is therefore Raman active but not IR active. The combinations of these modes and their overtones are more complicated but ultimately always fall into the pattern.

Another important condition for successful Raman scattering is the wavelength of the laser used to excite the electron. Depending on the exact quantum nature of the molecule probed, there may not be a suitable state that the electron can occupy when excited with a given laser energy. Only if there are one or more

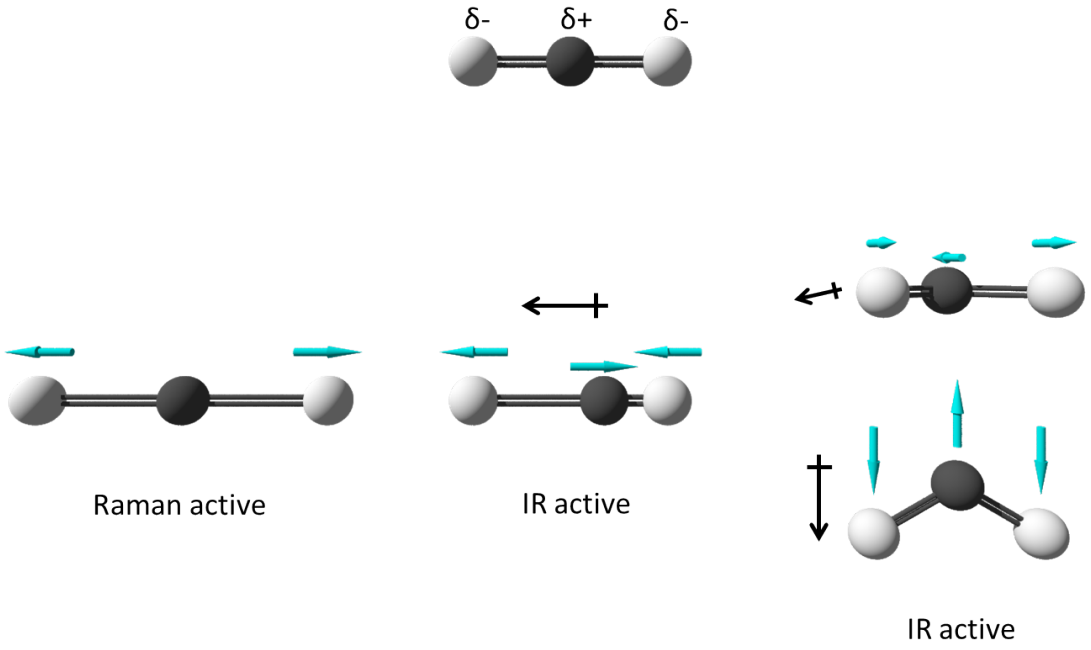

FIGURE 2.6: Ball and stick model representation of the vibrational modes in CO_2. The molecule itself is shown on top, the different modes on the bottom. From left to right: Symmetrical stretching, asymmetrical stretching and two degenerate bending modes. The asymmetrical stretching and the bending modes are IR active whereas the symmetrical stretching mode is Raman active.

states accessible can the Stokes Raman process occur at an appreciable rate and a change in the light be observed. Perfectly matched systems where the laser energy exactly matches that of the gap between the molecule's HOMO and an unoccupied level (often, but not necessarily, the LUMO) are called *resonant Raman* systems.

2.5.2 Scanning Raman spectroscopy

When using a modern confocal Raman microscope one can obtain local information with spatial resolution of the size of the laser point which is ∼300 nm diameter for a 532 nm laser with a numerical aperture of 0.95. This is useful for inspecting inhomogeneous materials like nanorods and nanotubes as well as graphene and other 2D materials which vary over length scales of microns. The spectrum taken is not representative of the whole sample but only contains local information. In these cases of samples with spatial inhomogeneities, scanning Raman spectroscopy can be employed. This is a method where the laser point is moved across the

sample and a spectrum is taken at regular spatial intervals. This spatially resolved information can be used to map out peak intensities and peak shifts or generate average spectra, displaying spatial inhomogeneities in the sample. An example of scanning Raman spectroscopy is shown in figure 2.7. It shows a MoS_2 flake which is much bigger than the laser spot of 300 nm. A random spot scan would yield a spectrum like in figure 2.7b) which is not fully representative of the sample as there are many variations, as the maps in c) and d) outline. The mapped area is 30 × 45 μm in size and contains the information of 20,000 spatially resolved spectra.

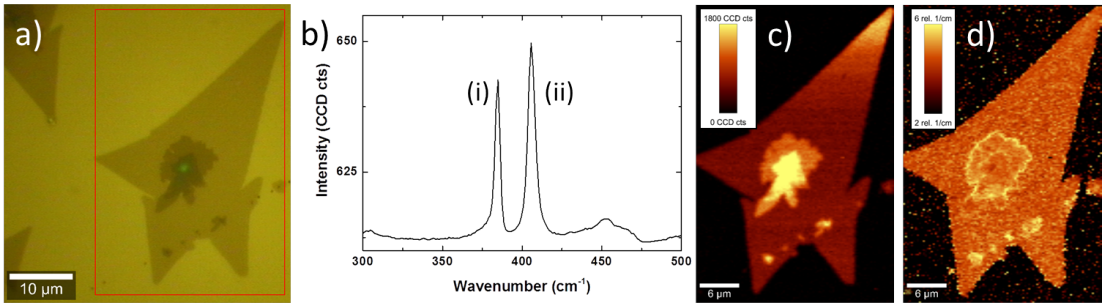

FIGURE 2.7: Example of scanning Raman spectroscopy on a MoS_2 flake. a) The optical image shows a flake of MoS_2 on a Si/SiO_2 substrate. The flake itself consists of several regions with different layer numbers and thicknesses. b) The average Raman spectrum of this sample contains two features, labelled (i) and (ii). c) A map of the sum of (i) and (ii) reflects the different features seen in a). d) A map of the width of peak (ii) highlights the boundary areas of the flakes.

All Raman spectroscopy for this work was performed using a WiTec Alpha R300 confocal Raman system with a 532 nm diode laser. Unless stated otherwise, an objective with 100× magnification and numerical aperture 0.95 was used. The laser power was up to 40 mW for graphene scans and 250-500 μW for MoS_2 and WS_2. The grating was set to either 600 lines/mm or 1800 lines/mm. For scanning Raman spectroscopy the sample and stage were moved by a piezoelectric motor in the x and y directions. Typically, a spatial scan resolution of at least 3 measured points per micrometer was employed.

2.5.3 Raman spectroscopy of graphene

Raman spectroscopy can be very effectively used for the analysis of graphitic materials like graphite, amorphous carbon, fullerenes, carbon nanotubes and of course graphene.[86–93] The Raman response of graphene has been analysed in detail in literature and there are several characteristic phonons present that are easy to detect. A Raman spectrum of graphene recorded with an excitation wavelength of 532 nm laser is shown in figure 2.8. The most important features are labelled as D, G and 2D band which are explained in detail below.

The phonon that all graphitic materials have in common is the so-called G band which is a vibration of the hexagonal lattice, shown in figure 2.9a). This phonon is always present as long as there is a hexagonal lattice. For pristine graphene the signal arising from this phonon is centred at 1583cm^{-1} but shifts with doping and lattice strain. Its intensity however is unaffected by many factors and it is therefore often taken as reference signal when comparing Raman spectra.

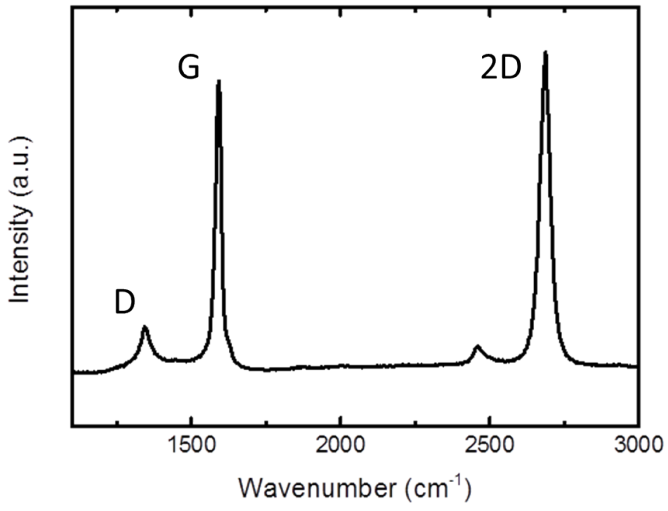

FIGURE 2.8: Raman spectrum showing Raman active graphene signals on 300 nm Si/SiO_2 accessible by 532 nm laser. The D signal is ideally not present at all as it can only arise from defects. The G peak at 1583 cm^{-1} is commonly used as a reference while the 2D peak at ∼2700 cm^{-1} indicates long-range order.

A phonon that most graphitic structures also possess is the so-called D band. This vibration is a breathing mode of the individual hexagonal rings of carbon atoms, shown in figure 2.9b). It is an indicator of defectiveness as this vibration cannot

exist in a perfect lattice. In a perfect graphene sheet the D signal only exists at the flake edges whereas nanocrystalline graphitic carbon shows a significant D band signal. The ratio of the D:G band intensity is commonly used as an indicator of the defectiveness of the lattice. If it is close to 1:1 the lattice is very disordered or the flakes are extremely small. If one assumes all D band intensity arises from the flake edges it can be used to estimate the crystallite size.[26]

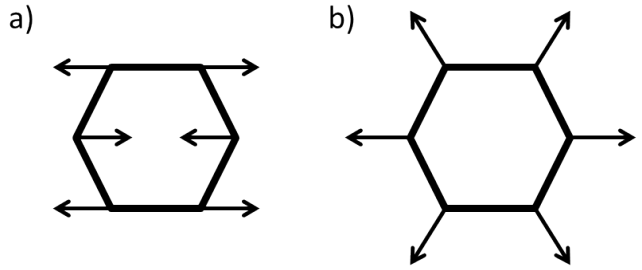

FIGURE 2.9: Simple representation of two Raman active vibrational modes in hexagonal carbon lattices. a) This movement mode is always present in hexagonal structures and is called the G mode for carbons; b) This ring-breathing mode is called the D mode. It can only occur when there are defects nearby as otherwise it will not be able to expand into anything.

Another very important phonon for graphene is the so-called 2D signal, sometimes also called G' signal, positioned around $\sim$2700cm^{-1}. There is no straightforward molecular representation for it like in the cases of the D and G mode in figure 2.9. It arises from an intervalley transition between the two sub-lattices of graphene as shown in figure 2.10b). The phonon's wavevector is too large to pick up with light but if a second phonon with opposite momentum is created, the net momentum change is zero. The energy difference is that of twice the phonon energy which can be picked up by the light. If long-range order is not present, the electron that has been scattered from the K point to the K' point will be deactivated by a defect and the energy difference will only be that of one phonon. This is picked up as the D peak. Hence the 2D signal is an extremely good indicator of the graphene quality. On a standard 300 nm Si/SiO_2 substrate the ideal ratio of the 2D:G signals is $\sim$3 and its full width at half maximum (FWHM) is between 30 cm^{-1} and 32 cm^{-1} or narrower.

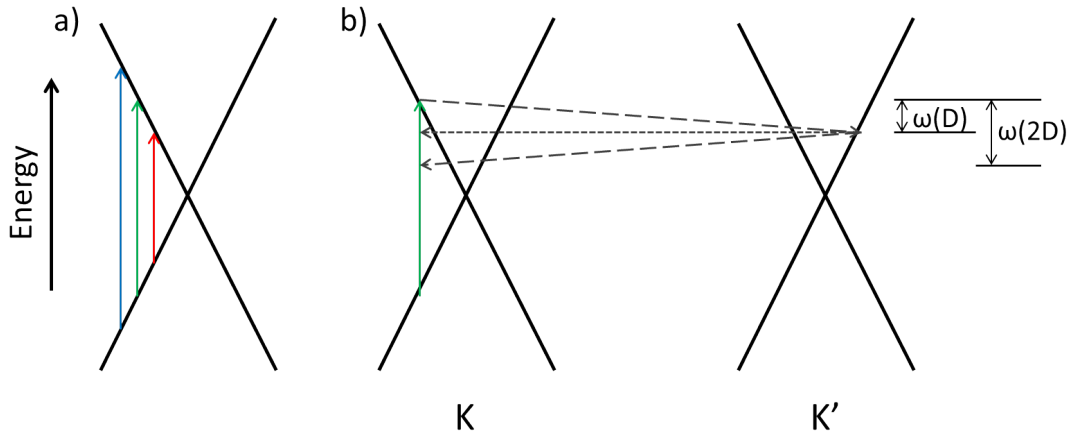

FIGURE 2.10: Solid-state description of Raman scattering for graphene. a) Due to graphene's peculiar band structure, every transition from the valence to the conduction band can be resonant. Therefore the spectrum tends to give very strong signals, regardless of excitation wavelength. b) The 2D peak originates from a scattering process from the K point to the neighbouring K' point and back. The phonon's wavevector is too large to be picked up by light so only the phonon pair with zero net momentum can be detected. If the electron is scattered back by a defect (dotted line) the signal gives rise to the D peak instead.

Both the D and 2D peak are always resonant with visible light because there is always a perfectly matching direct gap transition available for all photon energies as shown in figure 2.10a). As the process giving rise to them is an intervalley process, they are dispersive with laser energy, i.e. the phonon energy and hence the peak position in the spectrum shift with laser excitation energy. This shift is $\sim$50 cm^{-1}/eV for the D peak and therefore double that for the 2D peak as it is the D peak's overtone. In this work a 532 nm (2.33 eV) excitation laser was used and hence the D peak was always positioned at 1346 cm^{-1}.

Graphene flakes are nowadays often larger than the 300 nm laser spot size so the application of scanning Raman spectroscopy is a very powerful tool for visualising inhomogeneities. A map of the intensity of the G peak can give information about the number of layers and its position tells about doping and strain. The ratio of the D:G peaks can not only give an idea of the general defectiveness of the film but also outline regions like grain boundaries, hence allowing for easy assessment of grain size. The intensity and shape of the 2D band can be used to infer information about the number of layers and even the stacking order. For ideal monolayer

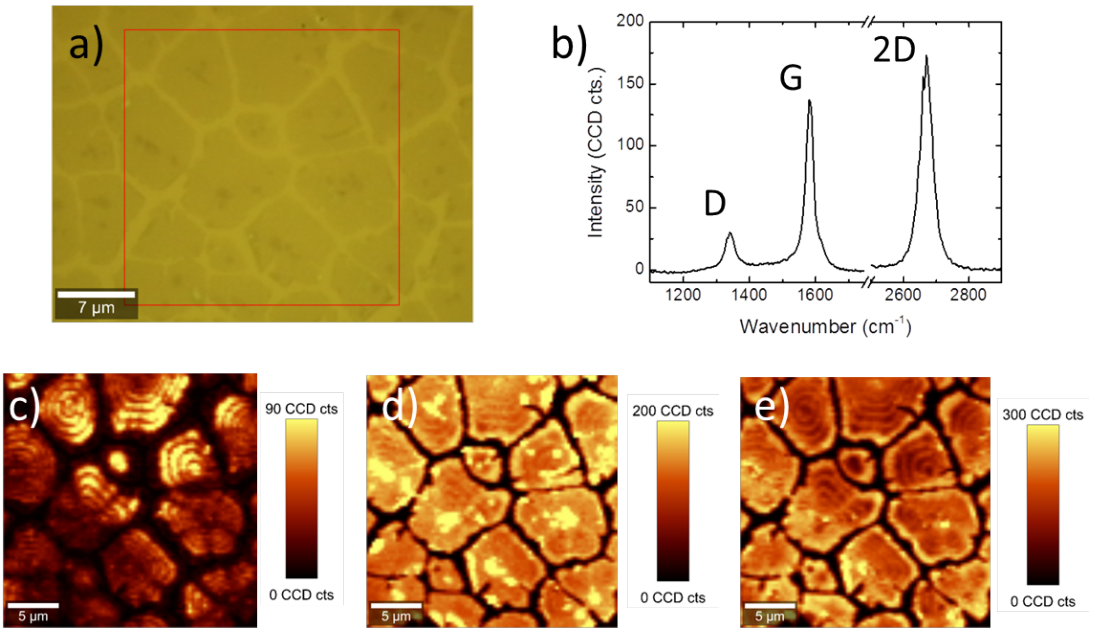

FIGURE 2.11: Scanning Raman spectroscopy of an incomplete graphene film on 300 nm Si/SiO_2. a) Optical micrograph with the area inspected inside the red box. The darker areas are graphene flakes. b) The average Raman spectrum of the area, taken from 5000 point spectra. c) This map of the D peak intensity reveals that the optically homogeneous graphene film has periodic defects in a concentric fashion. d) A map of the G peak intensity confirms the location of the graphene flakes and e) a map of the 2D peak intensity shows that, in the areas where the D peak is strong, long range order is suppressed.

graphene the 2D peak follows a Lorentzian function. The addition of a second layer in an AB stacking order changes the band structure to give four distinct Lorentzian contributions to this peak. Turbostratic packing however will simply reduce the peak intensity and possibly widen it but not add distinct contributions. An example of a rather peculiar incomplete graphene film is shown in figure 2.11.

There are some more peaks in the graphene Raman spectrum that are less important for this thesis and are therefore not covered in detail. Examples of these are the D' peak which is similar to the D peak but arises from an intravalley transition rather than an intervalley transition and the C peak which is a very low-wavenumber mode arising from interlayer vibrational modes.[89,94]

2.5.4 Raman spectroscopy of MoS_2 and WS_2

MoS_2 and WS_2 have similar Raman spectra as their active modes arise from the

same kind of vibrations with the only difference being the reduced mass of the systems due to the different transition metal atoms present. A representative spectrum of monolayer MoS_2 is shown in figure 2.12a). The peak at 385 cm^{-1}

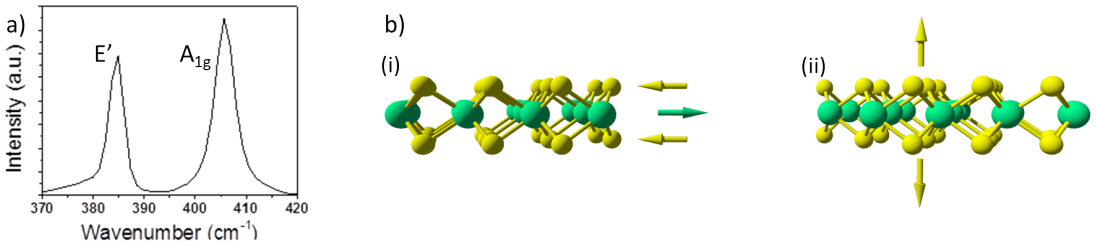

FIGURE 2.12: Most important Raman active modes in TMDs. a) Raman spectrum of monolayer MoS_2. The two peaks are the E' and $A_1^{'}$ modes which are present in many TMDs. They shift for different materials. b) Ball-and-stick model representations of the vibrations giving rise to the peaks seen in a), (i) E' mode and (ii) the $A_1^{'}$ mode.

(MoS_2) and 356 cm^{-1} (WS_2), called the E' peak for monolayer, E_g^1 for bilayer and E_{2g} for bulk, arises from an in-plane vibration of the sulfur atoms against the transition metal atoms. Conversely, the peak at 403 cm^{-1} (MoS_2) and 417 cm^{-1} (WS_2), called $A_1^{'}$ for monolayer and A_{1g} for multilayer, is caused by an out-of-plane vibration.[95–97] Both types of vibration are illustrated in figure 2.12b). Like graphene's G peak which arises from an in-plane vibration, the E' peak shifts with strain.[98] The $A_1^{'}$ peak shows a slight shift with electrical doping.[43] An increase in layer number from monolayer to multilayer and bulk leads to a redshift of the E peak and a blueshift of the A peak, yielding an overall increase in peak separation.[43,99] Also the monolayer of both materials, exhibiting a direct bandgap, shows significant photoluminescence in its spectrum.[44,53]

2.5.5 Surface-enhanced Raman scattering

Surface-enhanced Raman scattering (SERS) is an important mechanism for enhancing Raman scattering as it allows for studying the vibrations of molecules usually too weak to register.[100] Discovered several decades ago, it is mainly performed with rough metal surfaces and nanoparticles connected to the probe.[101,102] The majority of the enhancement is due to the so-called electromagnetic mechanism (EM). This mechanism can give enhancements by up to a factor of 10^{10},

allowing for single-molecule detection.[103–107] The EM is well-understood and extremely large enhancements can be reproducibly demonstrated.[108] It works by exciting surface plasmons (electrons oscillating vertically at the metal surface). These plasmons can couple very strongly to the analyte molecule. If the surface plasmon frequency, ω_p, is equal to the incident light frequency, ω_i, the incident electric field E that causes the excitation in the molecule is significantly enhanced. After a scattering event the outgoing field can again be enhanced, leading to an electric field enhancement of up to E^4 in resonant processes. For this dissertation the EM is not relevant as it does not apply to 2D materials.[109] This is because the plasmon resonance frequency of graphene is in the terahertz region, far from the IR and visible photons required for Raman spectroscopy.[110]

A second enhancement mechanism is called the chemical mechanism (CM).[111] Ignored for a long time as it is several orders of magnitude weaker than the EM, it gained a lot of attention recently with the rise of 2D materials which do not allow for the EM to occur but still exhibit significant Raman scattering enhancement by a factor of 10-100. There is no single, all-encompassing theory for the CM as it encompasses everything that is not the EM.

For 2D materials some advances have recently been made for explaining components of the CM. One factor that seems to be of major importance for enhancement to happen is the alignment of the molecule's highest occupied molecular orbital (HOMO) or lowest unoccupied molecular orbital (LUMO) with the 2D material's Fermi level.[109] If the difference between the Fermi level and the HOMO or LUMO is exactly the energy of the phonon concerned, there can be significant enhancement as illustrated in figure 2.13. That mechanism can be confirmed by modulating the height of the Fermi level, for example by electrostatic gating or electrochemical doping of the sample which will alter the significantly alter the enhancement.[112]

This mechanism works as such because 2D metals have a constant density of states (DOS) and therefore an equal number of states above and below the energy level to which the phonon scatters. From the Heisenberg uncertainty principle,

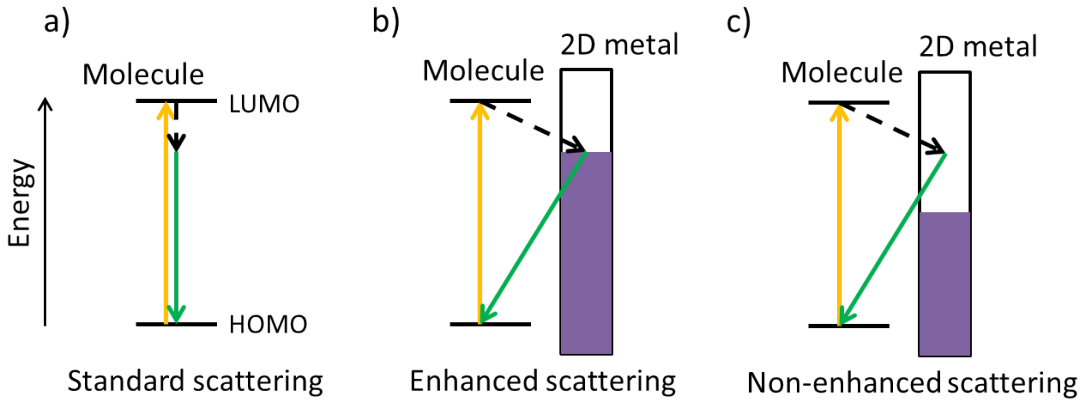

FIGURE 2.13: Energy level representation of the SERS CM. a) The standard Stokes scattering process involves an incident photon (yellow), a phonon (black) and an emitted photon (green). If the energy levels are not aligned well the scattering probability may be very low. b) If the molecule is in touch with a 2D metal and the filled states (purple) bring the Fermi energy to a point where the phonon energy is equal to the difference between the HOMO and the Fermi energy the scattering can be greatly enhanced. c) If the Fermi energy is far from both the HOMO and the LUMO there is no enhancement from this mechanism.

($\Delta E \times \Delta t \geq \hbar/2$), there is a small but finite uncertainty in the phonon energy and it can hence access energy levels slightly above and below its destined energy level. Accessing extra energy levels should lead to an enhancement, but by the Ward identity, the enhancement from these levels, symmetrical about the one central level, cancel out.[113] If, however, the Fermi energy is near this energy level, the states below the Fermi level cannot be accessed due to Pauli blocking. Hence the symmetry is broken and an enhancement observed.

2.5.5.1 Graphene-enhanced Raman scattering

Graphene, a 2D metal, exhibits the 2D SERS CM but not the EM.[114] In contrast to an ideal 2D metal which has a constant DOS, graphene exhibits a linear band dispersion and therefore there is always broken symmetry about any energy level but the Dirac point. The broken symmetry means that the effect of the levels accessible by ΔE above and below the level to which the phonon scatters does not cancel completely. Therefore there is always some SERS, even if the Fermi energy is not near the HOMO or LUMO. As it is such a useful material for SERS, its use has been given the name graphene-enhanced Raman scattering (GERS). As

outlined in the previous section, there are many effects that can cause and modify an enhancement and several of these have been discovered for graphene, including, but not limited to, the layer number, the Fermi level, laser energy, proximity of the molecule to the surface, molecular orientation and matching ring structures in the analyte's structure to graphene's hexagonal lattice.[115–120]

2.6 Scanning electron microscopy

Scanning electron microscopy (SEM) is an important experimental technique for visualising micro- and nanostructures.[121] A schematic representation of the setup and the different processes occurring in an SEM is shown in figure 2.14. An electron beam is accelerated toward and focused on the sample investigated. The electron emission is either thermionic or field emission and the focusing is done with two or more sets of electromagnetic lenses. There are several types of detector in place depending on the make and model of SEM.

The electron beam, once columnated and focused, hits the sample and interacts with it. Depending on the acceleration voltage (up to 20 kV) and the nature of the sample, the electrons can be transmitted, reflected or diffracted. They may also transfer their energy to the sample which in turn gives rise to Auger electrons, secondary electrons and X-rays from the sample. Auger electrons come only from the top 1 nm of the sample, secondary electrons from about 50 nm, backscattered electrons from $\sim$1-2 μm and x-rays from 5-10 μm. All these different processes can be monitored with different detectors. In the standard detection mode (in-lens), reflected electrons are collected. Also common, yet very different in its operation, is collection of the secondary electrons (SE2); both of these modes allow for reconstruction of the surface where the electrons interacted. X-rays may be collected for elemental analysis of the sample (EDX) and Auger electrons can serve the same purpose but are more surface specific. In order to avoid interference of gases with the electron beam SEM is commonly done in vacuum. Also, as the electron beam tends to accumulate charge on the sample, conducting samples are

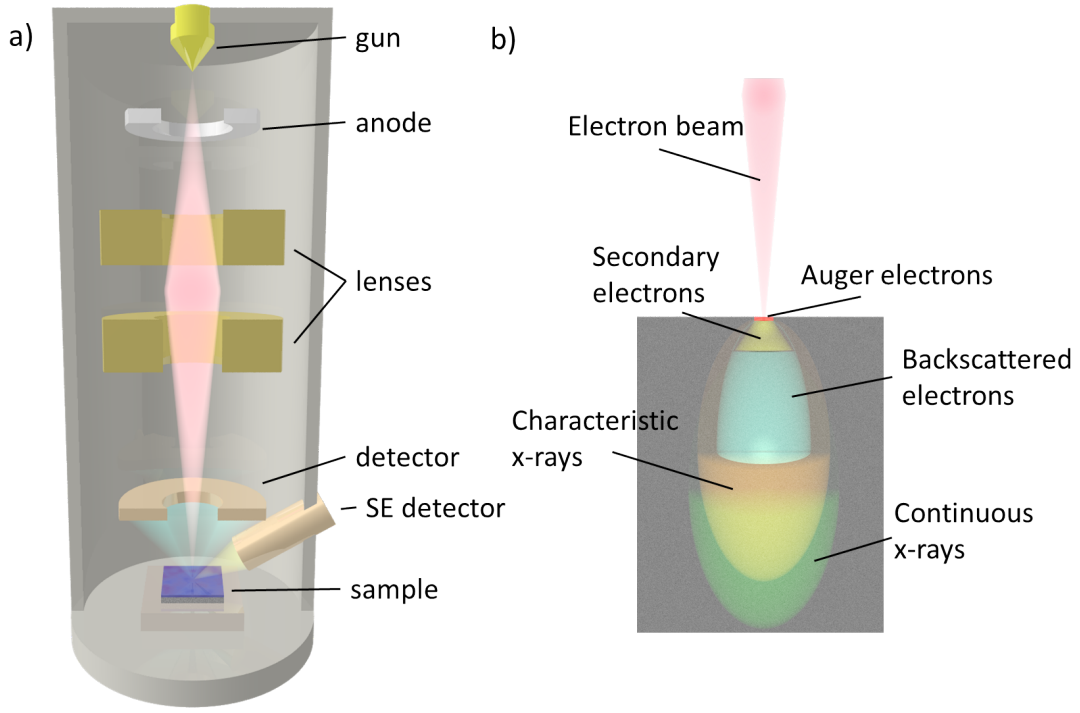

FIGURE 2.14: Schematic representation of scanning electron microscopy. a) Cross-section showing the most important components of a SEM. b) Sample cross-section showing the depth and origin of the different signals observable. Auger electrons come from the top 1 nm of the surface, secondary electrons from up to 50 nm depth, backscattered electrons up to ~2 μm and x-rays up to 5-10 μm. The exact numbers depend on the electron beam energy and the nature of the sample.

much easier to measure. Insulating samples are usually covered with a thin layer of conducting metals in preparation or have to be imaged with a very low electron current and accelerating voltage.

For this work scanning electron microscopy was performed with a Zeiss Ultra field emission SEM. The acceleration voltage was typically 2 kV and the detector used the in-lens detector.

2.7 X-ray photoelectron spectroscopy

X-ray photoelectron spectroscopy (XPS) is a very powerful technique for elemental analysis of surfaces.[122,123] It can reveal what kind of atoms are present and how they are bound to neighbouring atoms. It is based on the photoelectric effect

which was first reported in 1887 by Hertz and later fully explained by Einstein, earning him the Nobel Prize.[124,125] A schematic of the scientific principle is shown in figure 2.15. In principle, x-rays of known energy are absorbed by the electrons in

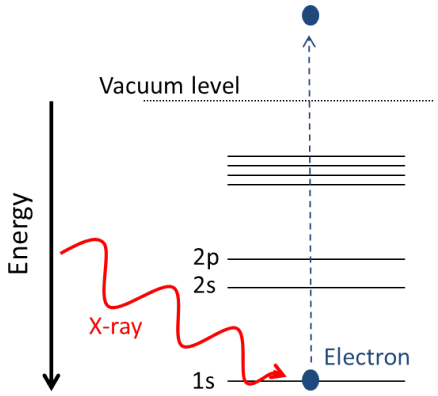

FIGURE 2.15: Energy schematic of XPS. An incoming x-ray excites an electron from its energy level into vacuum. As energy is conserved, the kinetic energy of the electron, which is measurable, is equal to the incidental x-ray energy minus the electron binding energy. This is different for every element.

the sample surface, to only a few nm depth. Those electrons are excited and as the x-rays are high in energy, the electrons are promoted out of their system entirely and into vacuum. Measuring the electron kinetic energy after this interaction allows for calculation of the binding energy of its orbital of origin according to Einstein's photoelectric effect formula:

$$E_b = \hbar\omega_i - E_k \tag{2.1}$$

E_b is the binding energy of the electron, $\hbar\omega_i$ the energy of the incoming x-ray photon and E_k the kinetic energy of the ejected electron. Binding energies are specific to elements and therefore allow for precise determination of the elements present. Shifts in the energies of binding orbitals, for example the carbon 2p orbital, can give information about what other element an atom is bound to and even whether it is a single or a double bond.

The standard x-rays used for XPS are the Cu K_α line with 8047 eV and the Al K_α line with 1486 eV. A wider range of energies and intensities is provided by purpose-built synchrotrons.

2.8 Electrical measurements

Electrical measurements give insight into the electrical properties of a material.[66] Usually resistivity, conductivity and charge carrier mobility are investigated. There are many more properties that can be investigated but those are beyond the scope of this thesis.

Bulk resistivity is defined as

$$\rho = R\frac{A}{L} \tag{2.2}$$

where ρ is the resistivity in Ωm, R is the resistance in Ω, A the cross-sectional area of the conducting sample and L the length of the channel measured. For 2D materials determination of the cross-sectional area A is challenging or even impossible so instead the sheet resistance is used:

$$R_S = R\frac{W}{L} \tag{2.3}$$

R_S is the sheet resistance and W the channel width. The unit of R_S is Ω but to distinguish it from bulk resistance it is usually written as Ω/sq. Note that sq. (square) is not actually a dimension but purely notation. Both bulk and sheet resistivity only give information about the majority carrier of the material measured.

Sheet resistance is measured using a four-point probe. In this kind of setup four probes are connected to the film to be measured. The probes have a known spacing and a current of known strength is forced through the outer two probes (source and drain). The potential difference between the inner two probes is then measured and the sheet resistance calculated from these values. The advantage of this approach is that it eliminates contact resistance of the probes with the sample. The sheet resistance is calculated according to the formula

$$R_S = \frac{\pi}{ln(2)}\frac{W}{L}\frac{V}{I} \tag{2.4}$$

Conductivity, σ, is the inverse of resistivity and the same applies to sheet resistance. It depends on the number of carriers $n_{e,h}$ in the material and their mobilities $\mu_{e,h}$ according to the relation:

$$\sigma = \frac{1}{R_S} = e(n_e\mu_e + n_h\mu_h) \tag{2.5}$$

One of the most common ways of determining the carrier mobility μ is by fabricating a field-effect transistor (FET). In this kind of device, shown in figure 2.16, there is an additional electrode separated from the sample by a thin dielectric, the so-called gate. Applying a voltage to this electrode causes capacitive action and can draw carriers in and out of the channel material. Monitoring the rate of change of source-drain current with applied gate voltage allows for calculation of the majority carrier mobility.

$$\mu = \frac{1}{C_{ox}}\frac{L}{W}\frac{\delta I_{DS}}{\delta V_{GS}}\frac{1}{V_{DS}} \tag{2.6}$$

C_{ox} is the gate oxide capacitance, I_{DS} the current between source and drain, V_{GS} the gate voltage and V_{DS} the source-drain voltage.

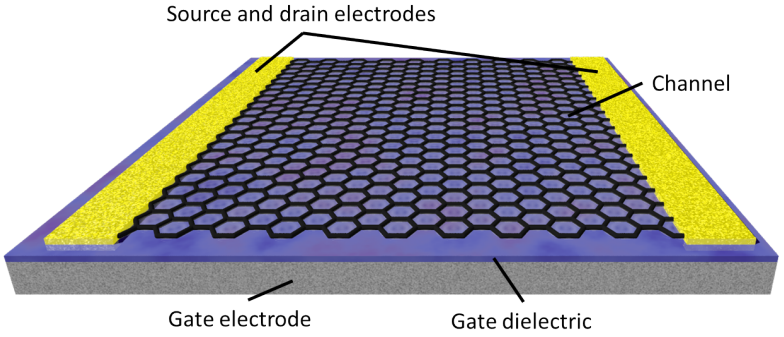

FIGURE 2.16: Schematic representation of a field-effect transistor. Current flows through the channel material between the source and drain electrodes. By applying a voltage to the gate electrode carriers are forced in and out of the channel, changing its properties.

In this specific case four-point probe measurements were performed using either a prober by Jandel with 1 mm probe spacing for large samples or Ti/Au electrodes were evaporated onto the sample and contacted with a needle prober by Süss.

Both probers were connected to Keithley 2400 source meters and controlled by LabView software.

2.9 Experimental design

Experimental design is a statistical method for optimising multi-variable processes.[126] It does not necessarily lead to a physical understanding of the process but works well for quantifying and optimising complex systems which is why it is very common in industrial settings. However, like any approach, one should not blindly rely on it as unexpected phase transitions or changes of reaction mechanism will thwart simple models.

In a standard intuitive optimisation process, a starting set of parameters and an output parameter are chosen. Process optimisation takes place by changing one variable at a time, thus making the effect of this one parameter visible until the output parameter appears maximised. A second parameter is then improved until again the output parameter is maximised and this pattern is continued until all parameters have been covered. This however ignores any possible relations between parameters and assumes they are orthogonal, i.e. independent of each other and varying one does not affect any of the others. This is rarely true for complex processes. Local minima and saddle points can also cause confusion.

An alternative to the standard process is the so-called "Design of Experiment" (DoE). It is a statistical method in which many parameters are varied at once and the entire parameter space is swept out. Common data points are the corners of the parameter space and some other high-symmetry points like the space centre. Results are fed into a statistical analysis program which yields a response surface through the parameter space. The mathematical description of the response surface can give an insight into the contributions of individual factors but full scientific understanding is not necessary for process optimisation. This has the advantage that it works even when the parameters are non-orthogonal and often requires a lot less experiments to be executed for statistically significant results.

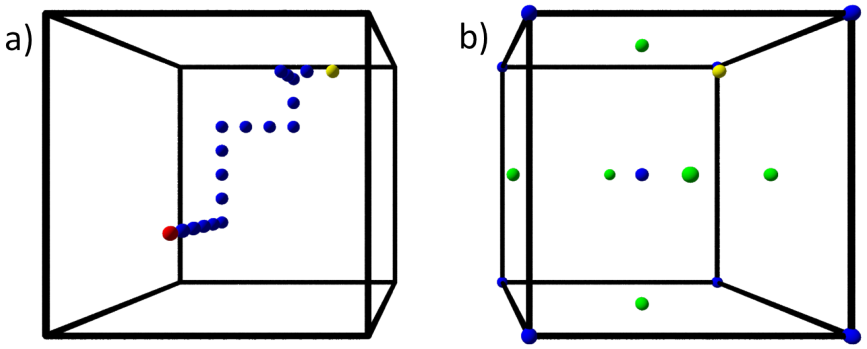

FIGURE 2.17: Schematic representation of the difference between a classical investigation and DoE. a) In a classical investigation a starting point (red) is chosen and one parameter is changed at a time (blue). Eventually the optimum parameter combination may be found (yellow) but if the parameters are not orthogonal this can be very difficult. b) In the DoE approach previous knowledge is almost irrelevant as extreme points of the parameter space are tried. This can be enough to yield statistically significant results but other optional points (green) may also be investigated.

A schematic illustration of the two different methods sweeping out a parameter space is given in figure 2.17. In this illustration the parameter space consists of three variables, shown as three-dimensional space. The standard approach (figure 2.17a)) involves picking a starting point (red), possibly based on previous knowledge, and varying one parameter at a time (blue points) to improve the process and eventually reach the optimal process (yellow). Large volumes of the parameter are left untouched even though they could yield other interesting results. In the DoE approach (figure 2.17b)), no previous knowledge is required. Points measured usually involve the corners of the parameter space and its centre. This is often enough to give a statistically significant model but further points of high symmetry can be investigated (green points). Not only does the DoE approach require less experiments, it investigates all parameters in more depth and tends to be more accurate. Because it is not based on any pre-conceived physical model it can spot unexpected things like phase transitions or inflection points much more easily although the inclusion of such encounters in the model requires significantly more advanced algorithms. A four-dimensional parameter optimisation is used in chapter 3 to optimise a graphene growth process.

2.10 Atomic force microscopy

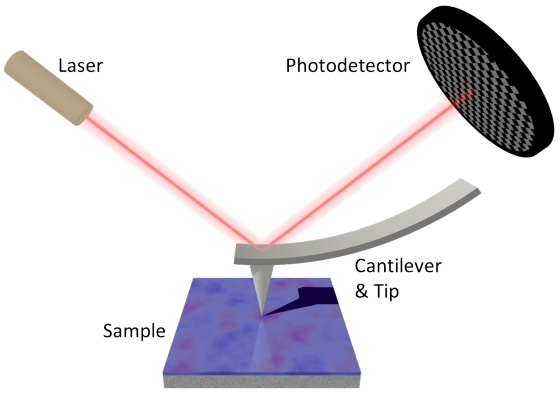

FIGURE 2.18: Basic AFM setup. A sharp cantilever moves slowly moves across the sample surface. Any time it encounters surface features it will be deflected, which is picked up by a photodetector as the laser reflecting off the tip will also move.

Atomic force microscopy (AFM) is an analysis technique that, in its simplest form, provides topological information of a surface.[127] A very sharp tip (∼30 nm at point) is dragged across the surface and its deflection as it encounters surface features is measured by a laser as shown in figure 2.18. This information can be used to reconstruct a topological map of the surface. There are three modes of AFM: Contact mode, non-contact mode and tapping mode. In contact mode, the tip is in very close contact with the surface and measures the repulsive forces, like a vinyl record player. This mode is also used for conductive AFM in which conductivity of the sample is measured. Contact mode can damage the surface and is therefore preferably avoided, especially for soft samples like biological tissue. In non-contact mode, the tip is very far from the surface and measures the attractive forces from the surface. Tapping mode is a compromise between the two where the tip is constantly oscillated up and down and experiences both attractive and repulsive forces which alter its mean height and phase. The phase information was historically ignored for a long time but actually provides interesting information like elasticity or adhesion forces. Nowadays tapping mode tends to be most commonly used for standard analysis.

Atomic force microscopy was either done with an Asylum MFP-3D AFM or a Dimension 3100 AFM. All scans were taken in tapping mode with Si tips with a tip radius of ∼50 nm and resonant frequency of 300 Hz.

2.11 Gas diffusion barriers

Diffusion is the net transport of a substance along a concentration gradient.[128] It is governed by Fick's laws of diffusion:

$$J = -D\nabla\phi \tag{2.7}$$

$$\frac{\delta\phi}{\delta t} = D\nabla^2\phi \tag{2.8}$$

The first law, equation 2.7, is for the steady state case where the supply is infinite. J is the flux in amount per unit area per unit time, D is the diffusion coefficient in area per unit time and ϕ is the concentration in amount per volume.

The second law, equation 2.8, is for the finite supply case where the concentration at the point of origin decreases as time passes.

For gas diffusion barriers, D should be as small as possible. Gas diffusion D is usually measured in $cm^3/m^2/day$. This measures how good the barrier is, but not how inherently good the barrier material is, as thickness is not taken into account. A bad material can make a good barrier if it is thick enough and *vice versa*. For a given material the permeability is hence given in units of cm^3cm/cm^2s (cm Hg) which also takes barrier thickness and partial pressure into account. 1×10^{-10} cm^3cm/cm^2s (cm Hg) is also called 1 barrer. A low-quality commercial barrier used for food packaging requires a permeability of <10 $cm^3/m^2/day$ and a high-quality one for OLEDs $<10^{-5}$ $cm^3/m^2/day$.

In the pursuit of this work, oxygen gas diffusion measurements were done in a Systech 8001 gas permeation tool. Films were cut to a circular shape of size somewhat bigger than 5 cm^2 and fixed in place with vacuum grease and a metal

clamp with an O-ring, exposing only an active area of diameter 2.5 cm. All measurements were taken at 23 °C at 0 % humidity with an oxygen partial pressure difference of 1 atm.

2.12 Organic light-emitting diodes

An organic light-emitting diode (OLED) is a type of light-emitting diode (LED) which uses an organic compound as active emission source.[129] This emission layer consists of an organic emitter molecule that is sandwiched between two electrodes, one of which injects electrons and one holes into the emission layer. The electrons and holes, separated by a defined energy gap, recombine in the emission layer and give off light corresponding to the energy gap as a result. In order for the light to escape the device, at least one of the electrodes has to be transparent. A schematic representation of such a device is shown in figure 2.19. It shows two electrodes, a hole transport layer, an electron transport layer and the emission layer. Real devices often contain more layers than that, including barrier, planarisation, and doping layers. A real OLED structure is discussed in chapter 4.

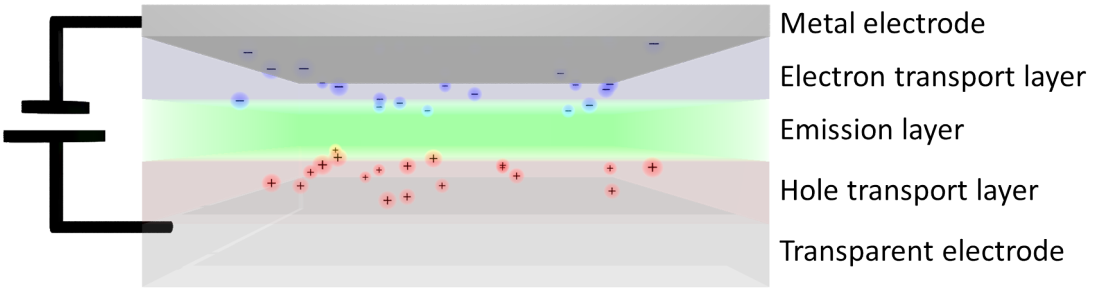

FIGURE 2.19: Structure of a generic LED/OLED. There is always a transparent electrode, an emission layer and a second electrode, usually not transparent. The electron and hole transport layers are not always separate from the electrodes.

There are several major advantages OLEDs have over conventional LEDs. Conventional LEDs employ GaAs or GaN as conduction and emission layers, which are rigid crystals whereas OLEDs often employ polymers that tend to exhibit a certain degree of flexiblility. The latter can be printed whereas the former have to be grown in specialised equipment. That opens a wide range of applications for

OLEDs and makes them potentially much cheaper than crystalline LEDs. Flexible OLED displays have already been demonstrated. However, due to the nature of the materials involved, the OLED requires airtight encapsulation as the highly energised organic emission layer easily reacts with oxygen and water, significantly shortening the device lifetime. Also, both OLEDs and conventional LEDs require at least one transparent electrode. There are very few materials that conduct electricity well and exhibit transparency. One of them is indium tin oxide (ITO), a rigid amorphous material from which the transparent electrode is usually made. Due to fluctuating costs of indium and constantly increasing demand in recent years, the search for an alternative is becoming more attractive every year and its lack of flexibility limits some of the OLEDs' potential. Hence graphene is being considered as one of the replacement materials as it is flexible, transparent, conducting, a good gas barrier, and will be cheap and abundant in future.

There are many reports of graphene-based OLEDs.[130–137] They vary widely in quality, efficiency and size but there are some encouraging reports. Many show that with the right doping and band alignment graphene can perform as well as ITO, at least on the small areas investigated (often the device area is not stated). However, even though it appears possible to make a graphene-based device, there are still problems: Often the graphene is rough which requires a planarisation layer. This can be very expensive as it is often a wet-chemical step whereas the other layers can be evaporated. Also there is no long-term study yet that shows the OLEDs actually survive for long, a crucial factor that has to be investigated before any integration can be attempted.

When analysing and comparing OLED performance there are several characteristics to take into account but most of them are related to the amount of light gained for the electric power put in. Firstly, there is the current or current density through the device vs. the voltage applied. As the energy is put out as light with quantised energy, there will be a threshold voltage above which current can actually flow. The minimum voltage that has to be applied is that which corresponds to the bandgap of the emitter. For a green emitter at 555 nm this corresponds to 2.2 V as the photon has 2.2 eV quantised energy. Any current which flows

below this threshold is leakage current, like in a diode. Other parasitic effects and internal loss mechanisms may also increase the threshold.

Secondly, the luminance per volt is important. Luminance is measured in cd/m^2 which is the amount of visible light put out per unit solid angle per device area. The solid angle component means it is a vector property and the visible light component means that a human-eye sensitivity correction curve is applied which has a maximum in the green light and reduces towards red and violet and disappears in the IR and UV regions. Hence a red OLED may produce more photons but still have a lower luminance than a green one as the human eye is more responsive to green light.

Power efficiency measures the overall amount of light produced per unit energy put in. This is in lumen per watt. This can be measured against luminance. Most light sources are more efficient in low luminance regimes and become less power efficient as they emit more and more light. This can be due to resistance increases from heating, capacitive effects or other processes.

Current efficiency is a measure similar to power efficiency and measures the amount of light produced per unit current, in candela per amp. When measured against luminance this gives an indication of whether other processes than the desired light emission from recombination occur as the device emits more and more light. Ideally this number should remain the same regardless of luminance but there can be a reduction with increasing luminance.

Chapter 3

CVD of graphene from ethene

This chapter covers and expands on the content of the publication "Growth optimisation of high quality graphene from ethene at low temperatures", *Chemical Physics Letters*, **2014**, 595, 192-196.[40]

3.1 Introduction

As outlined in chapter 1, graphene is shaping up to be a material that can have a huge impact on many areas of technology.[1,13,15,34,39,138–140] Section 1.1.2 gives a general overview of the various methods used to obtain graphene and the advantages and disadvantages of each. This chapter outlines a CVD method developed for growing large areas of graphene at a reduced temperature of 850 °C from readily-available ethene gas. The target was to produce large areas (10s of cm^2) of good-quality monolayer graphene at a temperature below 1000 °C, suitable for further processing into many applications, including, but not limited to, barriers, electrodes and sensors. This requires low-defect, closed films with reasonable flake size (>1 μm diameter), high transparency, sheet resistance below 1 kΩ/sq. and mobilities of several hundred $cm^2V^{-1}s^{-1}$. CVD is one of the most important methods for obtaining graphene as it is easily upscalable in a cost-effective manner and gives large-area and reproducible results while the graphene quality is

still high.[39,69] Out of all the different techniques, it is probably the one that best balances cost, yield and quality of the graphene obtained. However, even though it strikes the best balance, it is currently still too expensive and the quality of graphene leaves room for significant improvements.[10,33,83,141] Both of those metrics, cost and quality, are heavily influenced by the growth temperature which is very high in most cases.

The most common monolayer graphene CVD catalyst is copper with purity of 99.9% or higher. CVD on copper foil has been shown to give full coverage of mostly monolayer with flake sizes up to mm which is owing to the low carbon solubility in Cu, even at elevated temperatures.[33,35,142] Currently, most high-quality CVD graphene on Cu is grown at temperatures exceeding 1000 °C at low pressure using methane gas as carbon precursor.[83,143] Such a high temperature, which is close to the melting point of Cu (∼1085 °C), causes significant Cu evaporation, especially at the reduced pressure that many processes employ. The effects of the vapourised copper are not fully understood yet but some aspects are known: It leads to irregularities in the Cu surface structure as areas that are covered by graphene already cannot evaporate and hence become elevated islands on a lowering surface. Upon cooling the vapour condenses on both the sample and the furnace walls, degrading the sample quality and reducing furnace lifetime. These processes can severely affect the reproducibility of growth and are therefore best avoided.

Vapour pressures follow exponential trends with respect to temperature so even a small reduction in temperature can have a significant impact on the amount of Cu in the growth atmosphere.[144] More specifically, the vapour pressure of solid copper follows the equation: $log(p) = 14.129 - 17748/T - 0.7317log(T)$. Hence the vapour pressure at 1050 °C is $p = 0.0270$ Pa and that at 850 °C is $p = 0.000124$ Pa, a reduction by a factor of 218.[145] Reduced temperature also means lowered heating costs which become very important when moving to an industrial scale. However, reduction in temperature without a change in other process parameters would only lead to a reduction in quality as nucleation density increases and therefore the size of individual graphene flakes decreases. Multilayer growth is also more likely. There are many ways to avoid or at least reduce

the extent of quality reduction. One method involves electropolishing the copper surface before growth.[77,146] A smoother surface has less features that give rise to nucleation and hence the number of flakes is kept to a minimum. Changing the growth precursor can have a huge impact, especially if it is less stable than the methane used by Li *et al.* and therefore decomposes at a lower temperature.[35] Examples of this include ring structures like hexane, benzene or toluene and even alcohols like ethanol or propanol.[78–80,146,147] Continuous graphene films on copper have been reported at growth temperatures as low as 650 °C from toluene but need impractical liquid precursor handling and show significantly reduced electrical mobility in comparison to other reports of CVD graphene.[146] The lowest observed graphene island growth is at 300 °C from benzene but no continuous film was reported and the quality was not conclusive.[147]

This chapter presents a study to produce large areas of monolayer graphene on copper at temperatures below 1000 °C. This was necessary as the furnace used could only reach a maximum temperature of 1000 °C. The graphene should be cheap, show good electronic and optical properties, i.e. high charge carrier mobilities, and be produced in large quantities over a short time period. This was achieved by using ethene (C_2H_4), a cheap and easy to handle gas as carbon source. The eventual growth temperature used was 850 °C. The development of this process was helped by the use of experimental design (see section 2.9) for which the partial pressures of the process gases H_2, N_2 and C_2H_4, as well as the growth time were varied. Furthermore, a method of patterning the copper pre-growth to selectively mask graphene growth was investigated.

3.2 Growth patterning

In order to make devices from graphene, it has to be patterned into useful structures like FET channels or Hall bars.[3] This can be done by plasma etching or other aggressive chemical approaches but those can leave the graphene defective and may damage other components already deposited. Lithography of graphene

involves polymer deposition which leaves residues. An alternative is pre-structured growth that only allows the graphene to grow in certain areas on the copper catalyst. A masking mechanism investigated here involves defining a pattern on the copper foil by photolithography followed by Al_2O_3 ALD and subsequent lift-off. This masks areas of the copper which are subsequently unavailable for graphene growth in an approach similar to that used by Safron *et al.*[148]

3.3 Experimental

3.3.1 Furnace details

Growth was performed in an ATV PEO 604 LPCVD thermal processing system. This system is capable of processing 20 4" wafers at a time and can ramp from room temperature to its maximum temperature of 1000 °C in less than 20 minutes and actively cool back to room temperature in one hour. It is a hot-wall reactor with a quartz tube and platform. A schematic diagram is shown in figure 3.1. The minimum pressure in the current configuration is about 0.4 mbar and its maximum operating pressure is 10 mbar. It has connections and MFCs for several gases: Hydrogen (0-161 sccm), Nitrogen (0-10 slm), oxygen (0-1000 sccm) and ethene (0-85 sccm). The suppliers guarantee a variation of less than 5% in the MFC flow. Nitrogen, oxygen and ethene come from bottles of at least 99.95% purity (99.99995% in case of nitrogen). Hydrogen is provided by a Schmidlin PG-250 generator. All gases are fed through stainless steel gas lines of 10 m or less length and mixed and heated in the injector before entering the main chamber. The chamber is 30 cm long, 15 cm in diameter and heated by resistive heating from 15 heating coils around the centre as well as one big coil at each end. Temperature is measured by three thermocouples, one at the centre of the chamber beneath the sample and one at each end. Samples were usually placed in the furnace centre.
As the furnace opens up to atmosphere every time it is opened, there is a significant first-run effect. Hence the first run of every day produces different results from its

norm. Therefore it was seasoned by with a one hour 600 °C step with 10 sccm H_2, 5 sccm C_2H_4 and 300 sccm N_2 at the beginning of day it was used.

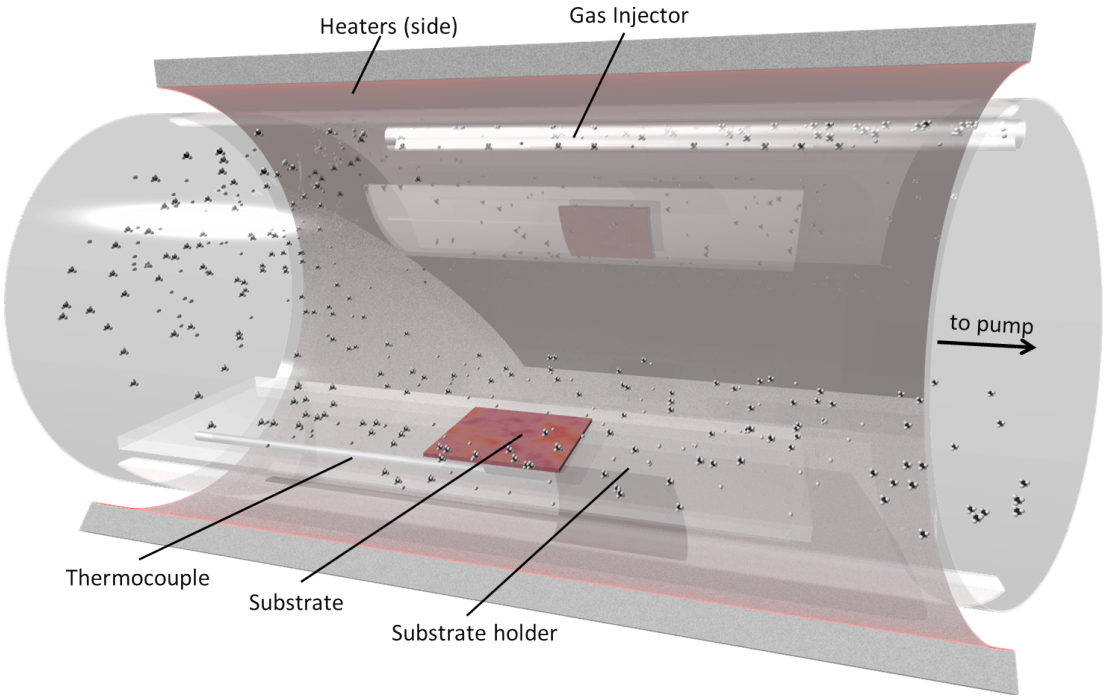

FIGURE 3.1: Schematic representation of CVD chamber in ATV PEO 604 tool. The chamber is 30 cm long and about 15 cm in diameter. It is heated all around, from the walls and the front and back end. Gases are pre-mixed and heated in the injector to ensure homegeneity. The main thermocouple is situated directly under the sample but there are two more, one at each end of the chamber.

3.3.2 Graphene growth

Graphene was grown using ethene gas as carbon precursor on 18 μm thick copper foil (99.99% pure, provided by Gould Electronics). This foil has a surface rms roughness of 0.176 μm and the sample size was usually around 3×3 cm or more. The foils were cleaned in HCl for 30 s to remove a protective zinc-chromate passivation applied by the supplier and subsequently sonicated mildly in acetone for 5 minutes.

Pre-growth patterning of the copper foil was done by defining a pattern on the copper foil using standard UV photolithography with positive photoresist. 30 layers of Al_2O_3 were deposited by ALD, yielding an approximately 3.3 nm thick

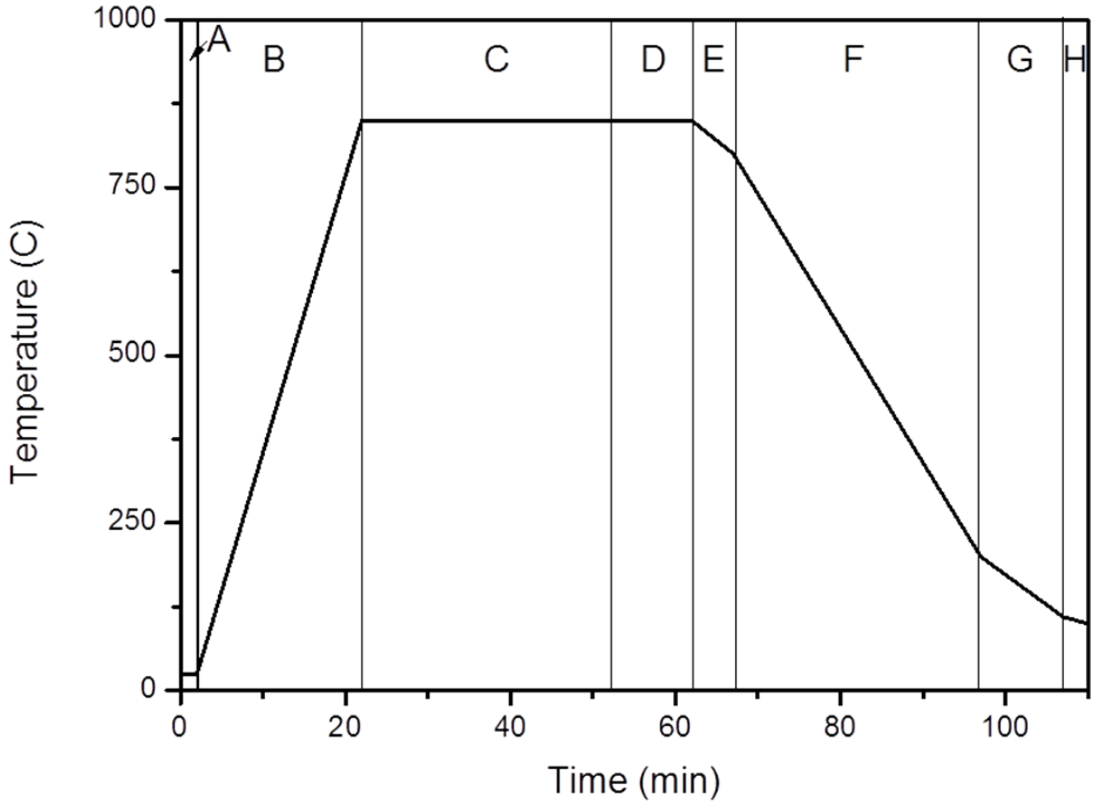

FIGURE 3.2: Growth conditions for graphene growth in the ATV PEO 604 furnace. The conditions for each step are:

Step	end T/°C	time/ min	H_2/ sccm	C_2H_4/ sccm	N_2/ sccm	Pressure/ mbar
A	-	2	0	0	0	0.4
B	850	20	15	0	0	1
C	850	30	15	0	0	1
D	850	5-20	0-161	1-85	0-500	2
E	800	5	2	0	0	1
F	200	20 (45)	0	0	0	1
G	110	10	0	0	0	1
H	100	3	0	0	5000	1000

film. The photoresist was lifted off and behind remained the Al_2O_3 pattern which marked the areas where no graphene would grow. A schematic of the growth conditions is shown in figure 3.2. The foils were loaded into the furnace, heated to 850 °C under 15 sccm H_2 flow at 1 mbar pressure and annealed at 850 °C for 30 min, also under 15 sccm H_2. The subsequent growth step consisted of a single step exposure of C_2H_4, H_2 and N_2. The composition varied from 0.85 sccm-42 sccm for C_2H_4, 1.6 sccm-160 sccm for H_2 and 0 sccm-500 sccm for N_2 while the overall pressure was kept constant at 2 mbar. The time of this step was varied between 5 and 20 minutes. Cooling took place under a small amount of residual H_2 at

2 mbar and took approximately one hour. After completed growth the deposited graphene or other carbonaceous film was transferred onto Si/SiO_2 substrates and analysed.[84]

3.4 Results & Discussion

The main objective in this process optimisation was reduced temperature graphene growth while still maintaining high material quality as ascertained by Raman spectroscopy and charge-carrier mobility measurements. 850 °C appeared to sufficiently suppress copper evaporation as optically significantly less copper was deposited on the furnace walls. In order to navigate the entire parameter space offered by the furnace used in terms of gas flows and growth time, DoE was employed.[126,150] The four parameters varied were the partial pressures of H_2, N_2 and C_2H_4 (expressed through a variation in flow rate), and growth time. With the parameters used there was always some kind of growth but the outcome varied significantly. The control parameter that defined quality was the average FWHM of the 2D peak of the sample's Raman spectrum, taken in 10,000 spectra over an area of 20 × 20 μm after transfer to 300 nm Si/SiO_2. This was chosen because the width of a Lorentzian curve fitted to the 2D peak can be directly related to the existence and quality of monolayer graphene (see section 2.5.3).[88,89,151–153] The narrower the peak, the better, with monolayer graphene around FWHM of ∼31 cm^{-1}, a value reported for mechanically exfoliated graphene and some cases of CVD graphene.[92,93] The exact experiments performed and a graphical representation and response surface plotted through the results of 23 experiments is shown in table X and figure 3.3, respectively.

Some general trends were observed: High amounts of H_2 compared to N_2 and C_2H_4 led to incomplete growth and many small islands. Similar results were observed for too much N_2 when sometimes next to no growth was observed but the nucleation density was also very low. Too much C_2H_4 yielded thick graphitic films that were more like pyrolytic carbon than graphene. Examples of these various types

H_2/ sccm	C_2H_4/ sccm	N_2/ sccm	time/ min	2D FWHM/ cm^{-1}
103	53	100	5	73
5	5	500	20	69
31	16	100	16	106
31	20	0	12	87
65	17	500	10	70
32	9	500	10	60
84	1	0	20	80
5	5	500	5	47
48	13	500	10	75
31	20	0	5	76
31	20	0	20	74
103	53	100	12	61
102	3	100	5	77
102	3	100	12	72
103	53	100	20	96
31	16	100	9	117
5	5	500	10	42
21	8	500	10	60
84	1	0	5	77
84	1	0	12	81
5	5	500	12	52
8	8	500	10	65
135	38	100	2	108

TABLE 3.1: Table of experimental conditions tested in pursuit of the graphene growth optimisation. The last column gives the measured Raman 2D FWHM for these conditions.

of growth are shown in figure 3.4. They show the optical micrographs of the films grown after transfer to 300 nm Si/SiO_2 and the average Raman spectra corresponding to the areas marked in red. Figure 3.4a) shows a film grown with little N_2, much H_2 and some C_2H_4. This film is thick and graphitic but also defective as seen from the Raman spectrum's large D:G ratio and small 2D:G ratio. The film in figure 3.4b) was grown with a high amount of N_2, little H_2 and also little C_2H_4. It is incomplete and the quality of what is present leaves room for improvement as seen from the 2D:G ratio. The D:G ratio implies that it is not too defective. Finally, figure 3.4c) shows a film grown with no N_2 but lots of H_2 and C_2H_4 for a long time. It is thick and very defective, implying it is more like pyrolytic carbon than graphene or graphite.

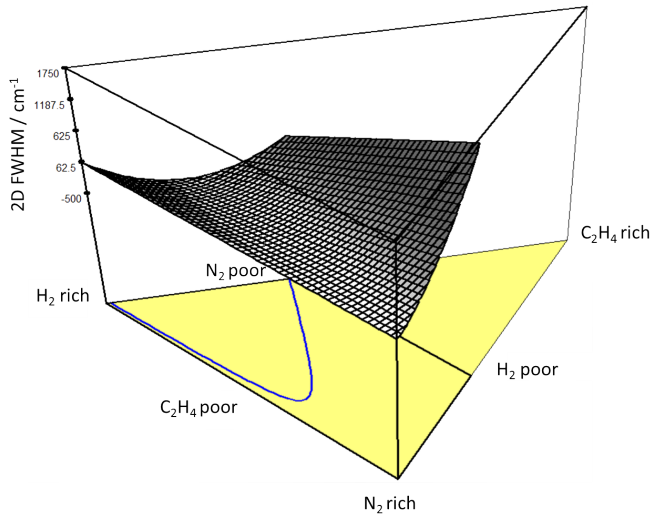

FIGURE 3.3: Graphical representation of the extrapolated effect of the different parameters H_2, N_2 and C_2H_4 at 12 minutes growth time on the output variable, the FWHM of the 2D Raman peak. Some of these numbers are impossible as the 2D peak width is never more than ~150 cm^{-1} but it serves as a good method for excluding certain parameter areas. The blue line represents a FWHM of 33 cm^{-1}.

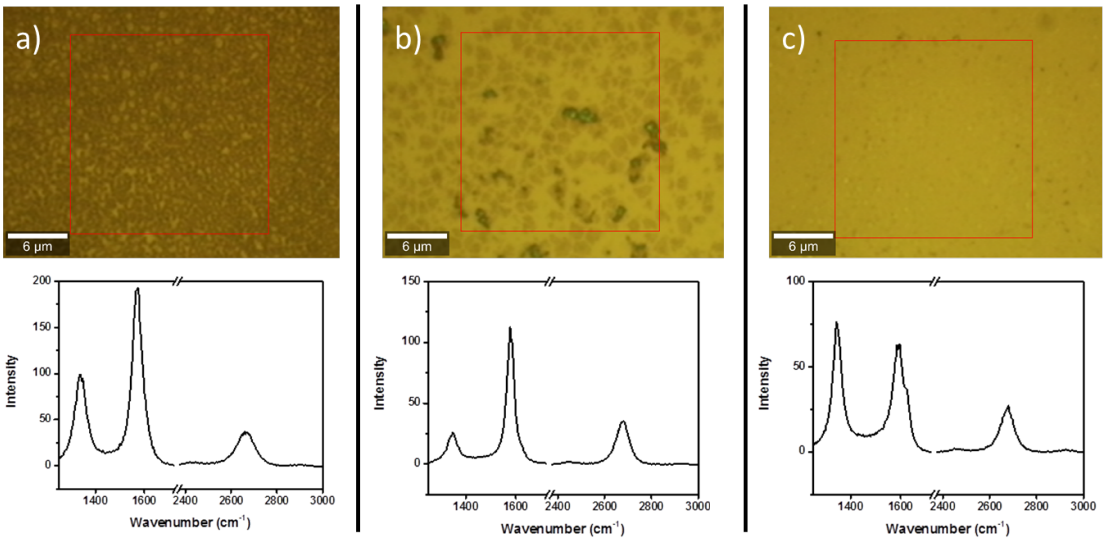

FIGURE 3.4: Examples of different types of growth observed as result of the DoE. a) Optical micrograph of the film after transfer to Si/SiO_2 and average Raman spectrum resulting from 16 sccm C_2H_4, 30 sccm H_2 and 100 sccm N_2 for 16 minutes. It is very thick and more like graphite than graphene. b) Optical image of film and average Raman spectrum resulting from 5 sccm C_2H_4, 5 sccm H_2 and 500 sccm N_2 for 20 minutes. The growth is evidently incomplete and the flake quality leaves room for improvements. c) Optical image of film and average Raman spectrum as result of 20 sccm C_2H_4 and 30 sccm H_2 with no N_2 for 20 minutes. The film looks homogeneous but the Raman spectrum shows that it is heavily defective and more like pyrolytic carbon than graphene or graphite.

The plot in figure 3.3 is only useful as an indication for what parts of the parameter space to exclude as can be seen upon closer inspection of the vertical axis which ranges from -500 to 1750 cm^{-1}. That is because the material deposited varies widely in quality. Some areas have no growth at all, some have far too much deposition and lead to multilayer growth and some deposit highly defective or even amorphous "graphene". Examples of those can be seen in figure 3.4. Unfortunately the 2D peak cannot widen indefinitely and also cannot distinguish between multilayers, tiny flakes (smaller than the laser spot) and amorphous material, all of which broaden the peak. The actual width of the peak is of course always positive and never broader than $\sim$150 cm^{-1}. By excluding the areas with predicted impossible values a narrow region remains which can be explored manually. By doing so the final parameter set was 10 minutes growth with 3.2 sccm H_2, 1.7 sccm C_2H_4 and 300 sccm N_2. An analysis of a film grown by this final parameter set is shown in figure 3.5. It shows an optical image of the graphene after transfer to SiO_2 which displays some darker regions which are interpreted to be onset of multilayer growth, a SEM image that confirms a flake size of $\sim$1 μm, Raman maps of D/G and 2D/G signal intensity ratios and 2D FWHM (d)-f)), all of which confirm a low defect density and high monolayer coverage. The average Raman spectrum (c)) is almost ideal and individual spectra from flake centres reflect the ideal graphene spectrum on SiO_2. Using optical and SEM contrast it was ascertained that these samples are about 80% monolayer with 20% multilayer growth onset.

For the use of graphene in electronic devices the electron and hole mobilities are key parameters. In long-channel devices (longer than the graphene grain size), the mobility is mostly reduced by grain boundaries. In order to determine the field-effect mobilities of this graphene, FET structures were fabricated. This was easiest done by pre-growth patterning: A line pattern was defined on the copper foil using standard UV photolithography with a positive resist. The exposed lines were 10 μm wide and spaced 100 μm apart. The copper foil was exposed to 30 cycles of Al_2O_3 ALD and lifted-off afterwards to leave behind Al_2O_3 lines of width 100 μm, spacing 10 μm, on the copper. This passivation is stable under the harsh

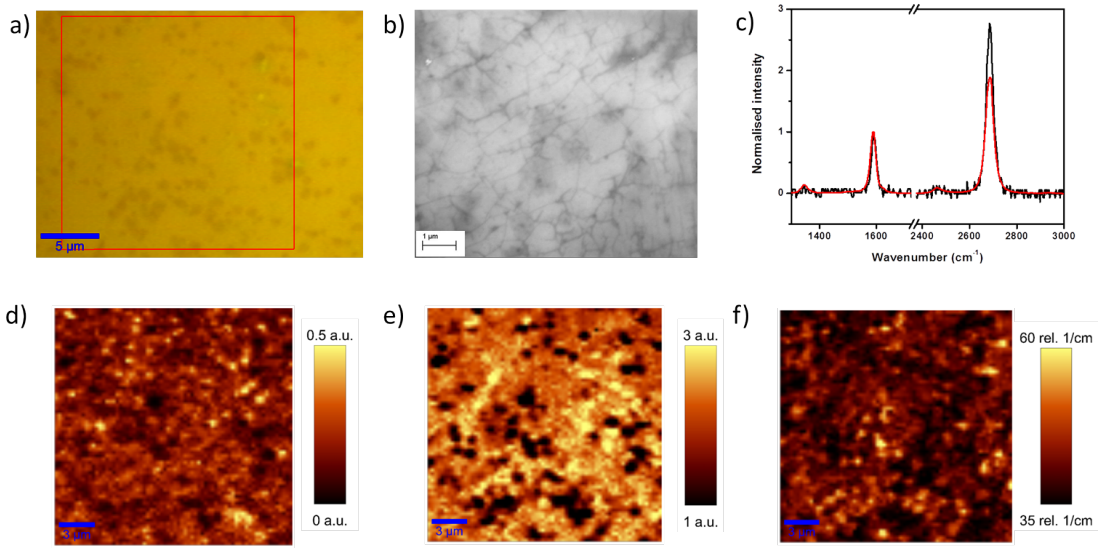

FIGURE 3.5: Analysis of graphene film grown according to final recipe. a) Optical image of graphene film after transfer onto Si/SiO_2. The darker patches are onsets of multilayer growth. b) SEM image of the same graphene film, showing uniform flake areas of ~1 μm. c) Raman spectra of the sample: Average (red) and flake centre (black). d) Mapped intensity of the area marked in a) showing the graphene D/G Raman peaks. The low intensity implies low defect density; e) Mapped intensity of the graphene 2D/G peaks showing mostly a ratio of ~2.5-3, corresponding to monolayer regions. The darker regions correspond to the multilayer patches. f) Mapped FWHM of the 2D peak after a lorentzian fit. Most regions have a width ~35-40 cm^{-1} which is desired for good monolayer graphene on 300 nm Si/SiO_2

graphene growth conditions. Growth was executed as previously described and no graphene grew on the Al_2O_3. This is schematically illustrated in figure 3.6.

The graphene lines were transferred onto a 300 nm Si/SiO_2 chip by standard transfer. The surface of the SiO_2 was treated with very mild base piranha solution (1% NH_4OH + H_2O_2 in water) to be hydrophobic and the Al_2O_3 lines did not stick. 40 nm thick gold electrodes were evaporated through a shadow mask to contact the lines, schematically shown in figure 3.6b) and optically in figure 3.6c). Gated 4-point probe measurements at a source-drain bias of 20 mV and are shown in figure 3.6e). The Dirac point shift shows that the sample was strongly p-doped which is attributed to PMMA residue and water adsorption.[154] After a mild vacuum anneal (black line) the Dirac point was still shifted but not as strongly. Electron and hole mobilities can be extracted from these lines according to equation 2.6.[155,156] The gate capacitance was estimated for this device for a 300 nm

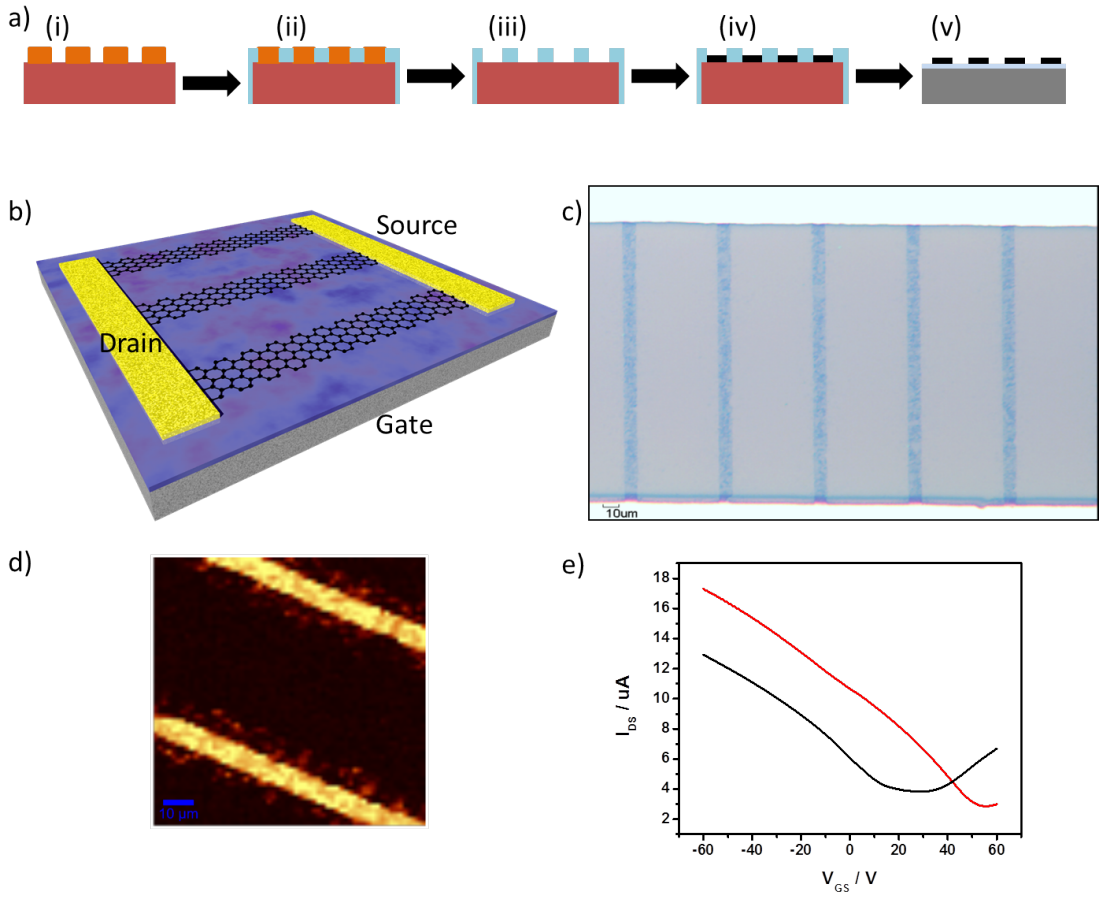

FIGURE 3.6: Illustrations of graphene growth patterning by Al_2O_3 deposition. a) A photoresist pattern is deposited on copper foil using UV photolithography. This is covered by 3.3 nm Al_2O_3 and lifted off. Graphene is grown but only covers the exposed copper areas. Finally this is transferred to an arbitrary substrate. b) Schematic illustration of what the GFET looks like. c) Optical micrograph of graphene lines after gold electrode deposition. The lines are 10 μm wide. d) Raman map of the G peak intensity showing graphene is only present along the lines. e) Electrical performance of the GFET, before vacuum anneal (red) and after vacuum anneal (black).

thick SiO_2 gate with relative dielectric constant 3.9. This yields 1100 $cm^2V^{-1}s^{-1}$ for holes and 700 $cm^2V^{-1}s^{-1}$ for electrons for the best sample and values between 500 $cm^2V^{-1}s^{-1}$ and 800 $cm^2V^{-1}s^{-1}$ for 5 other ones analysed.

The mobilities are often linked to the domain size of individual graphene flakes forming a film as the grain boundaries between flakes are commonly the points of highest electrical resistance.[157,158] Most important is to have well-connected domains, regardless of their sizes.[159] The results presented here reveal that even with comparatively small grain sizes and multilayer coverage of approximately

20 % high mobilities are still achievable.

These values do not reach those reported for exfoliated graphene or the best values reported for high temperature CVD graphene but are still suitable for most projected applications. As the measurements were taken on SiO_2 which limits mobility due to trapped charges the intrinsic mobility values should be higher than that. Thus low temperature graphene growth with ethene is an important step in making graphene more accessible and reproducible on a large scale for electronic and other applications, some of which are outlined in the next chapters.

3.5 Conclusion

In summary, a CVD synthesis for graphene grown from ethene at 850 °C was successfully developed. The final recipe allowed for samples many cm^2 in size to be grown with 80 % monolayer coverage and graphene domain sizes of $\sim$1 μm^2 as determined by optical and SEM image contrast. The monolayers have excellent quality with a Raman 2D peak FWHM of $\sim$35 cm^{-1} and 2D/G intensity ration greater than 2.75 with no D-band contribution inside the flakes. The average spectrum showed a D-band which is attributed to flake edges as it is not present in the flake centre and the broadening of the 2D-band to 40 cm^{-1} is attributed to bilayer growth onset, seen when mapping out these features over a large measurement area. Electrical characterisation of pre-growth patterned devices yielded an initial Dirac point of 55 V that shifted to 28 V after vacuum annealing. The field-effect mobilities were calculated to be 1100 $cm^2V^{-1}s^{-1}$ and 700 $cm^2V^{-1}s^{-1}$ for holes and electrons, respectively. These values indicate that the graphene produced by this method is potentially suitable for electronic and other applications.

Chapter 4

CVD graphene stacks for diffusion barriers and OLEDs

This chapter deals with an application of the large area graphene from the previous chapter in the field of barriers and electrodes. Parts of this chapter's content has been published as "Large scale diffusion barriers from CVD grown graphene", *Advanced Materials Interfaces*, **2015**.[160]

4.1 Introduction

It is a natural human urge to contain things or to restrict access to areas.[161] As a result, barriers are some of the most common components of just about anything in the world. There are very large ones in the shapes of walls and ship hulls, small ones like food packaging and display protection and microscopic ones like cell membranes and microchip back-contact separators. There are thousands of different barrier types all around us and each of them has different requirements. Properties like mechanical strength, transparency, electrical and thermal conductivity, flexibility or partial permeability vary from application to application.

In 2008 Bunch *et al.* experimentally showed that pristine graphene is the ultimate barrier after it had been theoretically postulated shortly beforehand.[14,162] A single

mechanically exfoliated flake of graphene, 4.75×4.75 μm in size, was demonstrated to be impermeable, even to helium, to the point that gas permeation rate could not be measured due to physical limitations of the setup. This has great potential as electronic devices such as flexible displays require transparent and conducting barrier layers, all of which are properties fulfilled by graphene.[130,137] Similarly, microchip back-contacts require a barrier to prevent the contact metal from diffusing into the chip. With the shrinking size of transistors on chips the barrier has to be scaled down and graphene, with its one-atom thickness, is the thinnest barrier possible. Its chemical inertness and mechanical robustness should allow graphene to endure as a barrier even under harsh conditions which a real display or biological would experience. However, that remains yet to be experimentally shown.

With such great potential it is in the interest of many industries to incorporate graphene as barrier. There is however a problem: While the outstanding properties of individual graphene flakes are astonishing, large-area films have shown no such performance. The lack of reports on the topic commensurate with those published by Bunch *et al.* conveys that making a large barrier is not as easy and straightforward as it may seem. This is mainly due to the fact that macroscopic samples of perfect graphene without defects are required for barriers but currently technologically impossible to achieve. There are plenty of reports of liquid or chemically exfoliated graphene or graphene oxide flakes blended with polymers to improve the barrier properties of said polymers but those are ultimately limited by the polymer's inherent properties which are vastly inferior to graphene itself.[28,163–165] Reports presenting effective graphene-only coatings are rare.[166,167] This can be attributed to the circumstance that CVD produced graphene has to be utilised for coatings on a larger scale. However, this graphene possesses grain boundaries and is not defect-free and its transfer from the growth catalyst can introduce cracks, holes and bubbles.[84]

At the time this study was performed and submitted for publication, the best report on a large-scale graphene coating barrier had been published by Kim *et al.* who showed that multiple graphene layers stacked on top of each other reduce the

Application	Max. allowed water + oxygen permeability	
	$g/m^2/day$	$cm^3/m^2/day$
General packaging	10	7000
Food packaging	0.1 - 0.5	70 - 350
Medical packaging	0.1	70
Wafer-based photovoltaics	10^{-2}	0.7
Thin-film inorganic photovoltaics	10^{-3} - 10^{-4}	0.07 - 0.7
Organic photovoltaics	10^{-4} - 10^{-5}	0.007 - 0.07
OLEDs	10^{-5} - 10^{-6}	0.0007 - 0.007

TABLE 4.1: General guidelines for the combined oxygen and water vapour barrier performance needed for various applications. They may vary significantly for specific systems and should ideally be lower than these values.

oxygen and nitrogen permeation through a polymer.[166] They covered 13.8 cm^2 of 100 μm thick poly(1-methylsilyl-1-propyne) (PTMSP) with five graphene layers using conventional polymer-assisted transfer. This resulted in a reduction of oxygen permeability from 730 barrer to 29 barrer (see section 2.11 for units) with respect to pristine PTMSP. This improvement may appear impressive but it has to be pointed out that PTMSP is highly permeable, hence pronouncing the barrier effect of graphene.[168] Even a very low quality barrier would lead to an improvement over PTMSP, hence a reduction by 96% is not too impressive. This was pointed out by the authors themselves as they came to the conclusion that stacked CVD graphene is not suitable for barrier applications. A list of some general oxygen and water barrier performance requirements is shown in table 4.1. The best barriers are made from aluminium-film laminates whith alternating layers of Al_2O_3 and polymers.[169]

In the study presented here, the oxygen barrier properties of CVD grown graphene stacks transferred onto poly(ethylene terephthalate) (PET) were investigated. PET is an inherently good barrier polymer and commonly used in food and sometimes medical packaging.[170] 150 μm of PET pass about 13 $cm^3/m^2/day$ of O_2 making it a good starting barrier. The graphene was grown according to the process outlined in chapter 3 with a second growth step containing slighly more ethene to ensure closed grain boundaries. Large-area samples of 5 cm^2 on 150 μm thick PET substrates were fabricated using both the conventional and a modified polymer-assisted transfer method, the latter avoiding polymer residues between layers and

yielding a tighter arrangement. This method of stacking was filed as a process patent.

At the same time that this study for oxygen permeation was performed, a very similar study was published by Choi *et al.* who used the same approach but tested for water permeation rather than oxygen permeation.[167] They also confirmed that this approach worked and stacked graphene barriers are feasible. They aimed to protect OFETs and managed to limit device decay to half its unprotected value over a time of 42 days. This is still far from a real device lifetime but a significant start.

The application that has some of the most extreme requirements for barriers are OLEDs. They are required to work for years but only need a tiny amount of oxygen or water in order to be completely destroyed. Additionally, the barrier has to be transparent so the light can get out of the device and if the barrier is also conductive it can serve as an electrode, saving one component. Graphene theoretically fulfils all of these requirements. However, it is unlikely that it will indeed make a good enough barrier for OLEDs. However, even as a transparent, flexible electrode it would be of significant value already. To check the viability of graphene stacks for electronic applications they were incorporated into OLEDs by Philips corporation and their performance compared to ITO electrodes, the current industrial standard. This is not the first study of graphene for OLED electrodes. As a matter of fact, almost immediately after the discovery of graphene and its extraordinary properties, the concept of a graphene-based OLED electrode was patented many times.[171–174] Making an OLED is not particularly difficult any more. The difficulty lies with making it efficient, large-area and, most importantly, lasting. The standard comparison is comparing the graphene electrode to an ITO electrode which is the current industrial standard. Even solution exfoliated graphene flakes have been shown to be comparable ITO in some cases but showed significant hysteresis in a relatively simple device structure.[135] The devices were of very small area in those cases and a large OLED (greater than a few cm^2) has yet to be demonstrated. CVD graphene tends to perform much better than solution-processed graphene. Using multilayer graphene and advanced

device structures, Sun *et al.* produced well-working green OLEDs with maximum output of 0.75 cd/A and 0.35 lm/W and Hwang *et al.* made ones with similar efficiency in the sky-blue colour regime.[136,175] Some of the best ones produced so far were developed by Philips as part of the "Grafol‘" project. They utilised monolayer CVD graphene and made green OLEDs with performance of 35-40 lm/W at 1000 cd/m^2.[130,134]

4.2 Experimental

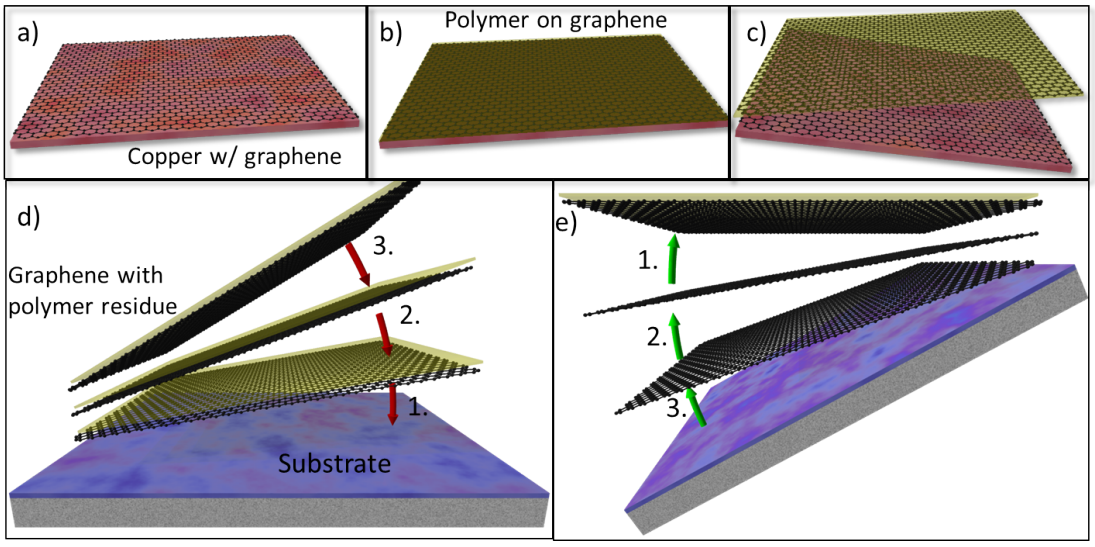

FIGURE 4.1: Schematic representation of the different transfer methods: a) Graphene is grown on copper and b) the graphene is covered with transfer polymer. c) The copper is dissolved and the graphene layer is either transferred onto the final substrate or onto another piece of graphene on copper (shown here). d) The standard polymer assisted transfer involves transferring one layer at a time onto the final substrate but leaves polymer residue between each layer. d) The modified stacking method transfers the graphene onto other graphene layers first and onto the final substrate last, thus avoiding polymer residue altogether.

Two types of barrier were made. Each consisted of a 150 μm PET substrate covered with one or several graphene layers but the method in which the graphene was added varied. The graphene used was produced as outlined in chapter 3 with a small alteration to the recipe that introduced an extra five-minute step with 10 sccm C_2H_4 instead of 1.5 sccm to deposit extra material at the grain boundaries. For the **conventional** transfer method, shown in figure 4.1d), graphene was

transferred onto the PET using the standard method described in section 2.3. The polymer used for this transfer was PMMA. After dissolving the handling polymer a second layer was transferred onto the first one and this process was continued until the desired number of layers had been reached as shown in figure 4.1a)-c)&e). The **modified** transfer involved first transferring the graphene onto another graphene layer still on copper without dissolving the polymer. These two combined layers could then be transferred onto a third layer and finally onto the destination substrate. This means only one polymer handling layer was used in the process and none is between the graphene layers.[133] To ensure good adhesion and conformity in the case of different topologies, the polymer was always re-flowed above its transition temperature of ∼150 °C and only dissolved after transfer onto the PET substrate. Oxygen gas diffusion measurements were done in a Systech 8001 gas permeation tool. Films were cut to a circular shape of size somewhat bigger than 5 cm^2 and fixed in place with vacuum grease and a metal clamp with an O-ring, exposing only an active area of diameter 2.5 cm. All measurements were taken at 23 °C at 0 % humidity with an oxygen partial pressure difference of 1 atm. A photograph of the clamp is shown in figure 4.2. The clamp is based between two chambers, one filled with oxygen and the other with nitrogen. The oxygen flux through the barrier into the nitrogen-filled chamber is measured by a coulorimetric sensor which functions by performing electrolysis with the incoming oxygen and measuring current produced. The detection limit on this specific tool is ∼0.01 $cm^3/m^2/day$.

4.2.1 OLED fabrication

The fabrication of OLEDs and their subsequent testing was done by Philips corporation. Graphene stacks were transferred onto glass using cellulose acetate as transfer polymer and they were turned into OLEDs by evaporating functional layers onto them. The final stack is schematically shown in figure 4.3. It consisted of a glass substrate, the graphene stack, 5 nm MoO_3, 135 nm MoO_3 doped 4,4'-Bis(N-carbazolyl)-1,1'-biphenyl (CBP) at 20 wt% loading, 5 nm intrinsic CBP,

FIGURE 4.2: Photograph of the clamp used to fix the film in place for oxygen permeability measurements. The active area is 2.5 cm in diameter, corresponding to 4.91 cm^2. This clamp is positioned between two chambers, one with oxygen and one with nitrogen.

15 nm CBP doped with the green phosporescent emitter fac-tris-2-phenylpyridine iridium ($Ir(ppy)_3$) at 10 wt% loading, a 65 nm 1,3,5-tris-phenyl-2-benzimidazolyl-benzene (TPBi) layer, a 1 nm LiF layer and a 100 nm Al cap. No planarisation layer was applied.

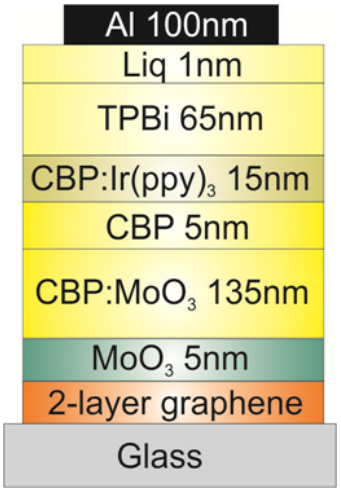

FIGURE 4.3: Schematic representation of the OLED structure. The graphene was transferred onto the glass and all subsequent layers were evaporated onto it. Everything but the graphene transfer was done by Philips corporation in Aachen, Germany.

4.3 Results & Discussion

4.3.1 Barriers

The results of the measurements are summarised in table 4.2. The PET substrate on its own showed oxygen permeability of 13.9 $cm^3/m^2/day$, corresponding to 3.18×10^{-2} barrer which is close to the literature value of $\sim 2 \times 10^{-2}$ barrer.[170,176] No enhancement of the barrier properties was observed when only a single layer of graphene was applied on top of the PET. This is most likely due to imperfections in the graphene and not surprising as it is well known that transferred graphene has holes and cracks as well as the inherent grain boundaries, all of which allow for gas transport through the layer. Optically no macroscopic holes could be seen, even under 100× magnification. However, not the entire film could be searched by eye so there may be some present which unlikely. Even though the graphene used had few defects, no air tight gas barrier could be achieved with a single layer.

No. of graphene layers on 150 μm PET	Conventional transfer permeability/ $cm^3/m^2/day$	Modified transfer permeability/ $cm^3/m^2/day$
0	13.9	13.9
1	13.8	13.8
2	13.4	7.8
3	-	4.6

TABLE 4.2: Oxygen permeation measurements through PET and graphene

Upon application of a second layer, which should statistically cover some of the holes and cracks of the first layer, no significant improvement was observed for the conventional transfer method. The modified transfer however, which does not allow for polymer residue between layers, displayed significant improvement to 7.8 $cm^3/m^2/day$. A third layer of graphene lowered this even further to 4.6 $cm^3/m^2/day$.

This major improvement over the unsuccessful conventional transfer is attributed to the lack of polymer residue between layers.[155] The conventional transfer will always result in residues which can never be removed completely. An optical image of such polymer residues on a single layer of transferred graphene is shown

in figure 4.4a). The modified transfer only gives polymer residues on top of the top layer where they do not interfere with diffusion through the stack. Alternatively it could be that the modified transfer leads to less overall damage of the graphene, thereby reducing the number of cracks and holes. As the samples were all handled in almost the same fashion this appears less likely. This could ultimately be determined by using the calcium method test where calcium is covered with the barrier and oxidised parts become opaque, hence highlighting areas with holes.[177]

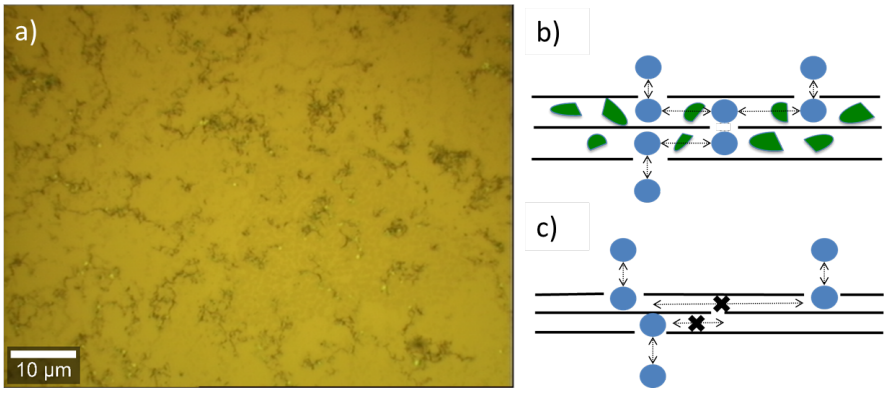

FIGURE 4.4: a) Optical micrograph of a graphene sample with much polymer residue after transfer to Si/SiO_2. b) Proposed model for gas diffusion through the stack: The polymer residue (green) prevents close contact between stacked layers and allows for oxygen (blue) diffusion through the layers. c) If no polymer residue is present the stacking is tighter and diffusion through the stack is significantly inhibited.

Standardising the graphene stack barrier performance to its thickness in order to assess the material's inherent barrier properties gives a permeability of 1.10×10^{-7} barrer; the calculations are shown below. This performance is comparable to many modern packing materials as it performs slightly better than SiOx and is on track for improving thin, conducting barriers to the point where they become useful for oxygen-sensitive devices, either in sensitive biomedical packaging or even some low-quality electronics.[178,179] It should be remarked that even though the graphene performs on par with SiOx, it is much easier and cheaper to scale up the thickness of SiOx. Graphene may still succeed though because of its transparency and flexibility.

The calculation for extracting the graphene's barrier properties is as follows:

$$\frac{1}{P_{PET}} + \frac{1}{P_{Graph}} = \frac{1}{P_{total}} \rightarrow \frac{1}{13.8} - \frac{1}{4.6} = \frac{1}{P_{Graph}} \rightarrow P_{Graph} = 6.9\ cm^3/m^2/day$$

Hence the 3 graphene layer thick film passed 6.9 $cm^3/m^2/day$. Adjusting this to a film thickness of ∼1 nm and a differential pressure of 1 atm yields:

$$\begin{aligned} p_{Graph} &= 6.9\ cm^3/m^2/day \times 10^{-7}\ cm \times \frac{1}{76\ cmHg} \times \frac{1\ day}{84600\ s} \times \frac{1\ m^2}{10000\ cm^2} \\ &= 1.10 \times 10^{-17}\ cm^3 cm/cm^2 s(cmHg) = 1.10 \times 10^{-7}\ barrer \end{aligned}$$

To thoroughly characterise these films and their properties they were analysed with SEM, Raman spectroscopy and XPS. An optical photograph of a 3 layer stack is shown in figure 4.5a). It confirms that the graphene is still very transparent and that this film can be used in some mid-range applications that require transparent barriers. Its transmission rate is too high for OLEDs but it may suffice for some wafer-based photovoltaics. A SEM image of a 5 layer stack on Si/SiO_2, shown in figure 4.5b), shows very few features, which is desirable for a graphene film.

Raman spectroscopy was used to analyse both the graphene used to make the stack and the stack itself. Figure 4.5c) shows the mapped intensity of the D/G peak ratio of a 20×20 μm area. The brighter regions outline grain boundaries and some other defects. Average Raman spectra are shown in figure 4.5d). The black spectrum is that of the original graphene. Its slighly increased D/G ratio and reduced 2D/G ratio compared to figure 3.5 is attributed to the extra material at the grain boundaries. The red spectrum is the average of the 5 layer stack. Even though the stacking is of random orientation, the 2D/G peak intensity ratio is decreased, indicating interactions between the layers, something that is only possible in close spacing, supporting the contaminant-free transfer method.

XPS on a 5 layer film on Si/SiO_2 showed the C 1s peak convolution expected for graphene with some PMMA residue, shown in figure 4.6. However, by comparing the strength of the silicon signal (figure 4.6a)) from the 5 layer stack to that of 1

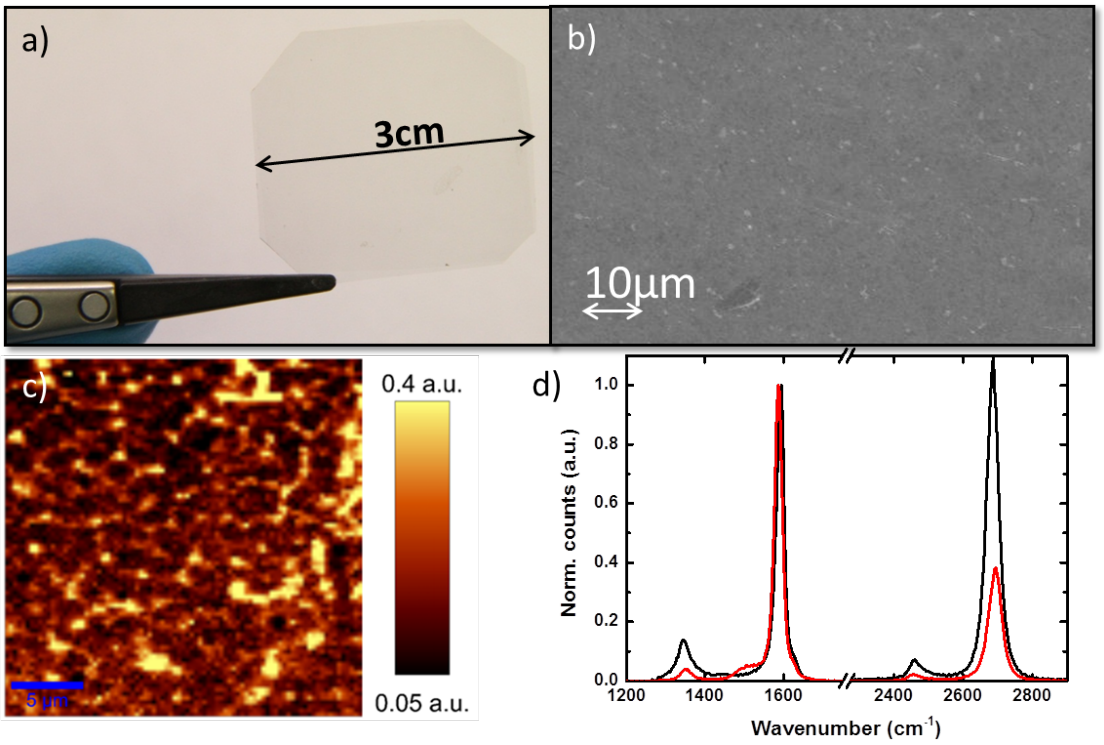

FIGURE 4.5: Analysis of a graphene stack made by the modified transfer method. a) Optical photograph of a 3 layer stack on 150 μm PET. b) SEM image of a 5 layer stack on Si/SiO_2. c) Mapped Raman intensity of the D/G peak intensities of the 5 layer stack on Si/SiO_2. d) The average Raman spectrum of the area analysed in c) is shown in red, that of a monolayer of the graphene used for making this stack in black.

layer, it is possible to calculate the thickness of the film which was found to be 2.5-3 nm. Nominally 5 layers of graphene should be 1.85 nm thick but considering these are not crystallographically aligned and there is some polymer residue on the top layer, this graphene seems to be tightly packed. The multiple scattering backgrounds in the region of 1200-600 eV in the survey scan also indicate multiple layers and disorder. The XPS work and interpretation was completed by Dr. Nina Berner.

4-point-probe measurements of a 3 layer stack with a large press-on probe yielded a sheet resistance of 536 Ω/sq., a value that makes these films viable for electronic applications. The graphene was not intentionally doped but the PMMA residue tends to p-dope it. Transparency measurements were skewed by the 150 °C heating step as it caused the PET to become cloudy. As this clouding effect varied from sample to sample it was not possible to obtain accurate % transmission results.

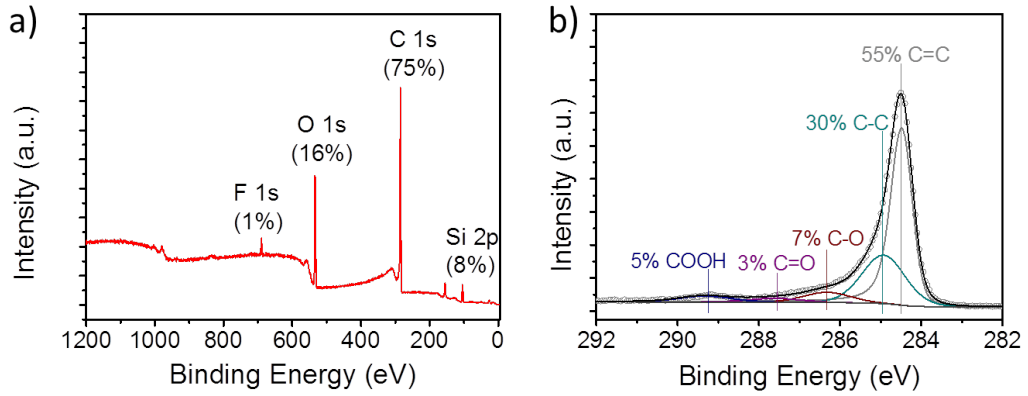

FIGURE 4.6: XPS spectra of a 5 layer graphene stack on Si/SiO_2. a) The survey scan shows the expected components of Si and O in an 1:2 ratio as expected from the SiO_2 substrate. From the decay of the Si 2p peak compared to uncovered SiO_2 the graphene film thickness can be estimated to be 2.5-3 nm. The multiple scattering backgrounds in the region of 1200-600 eV indicates multiple layers and disorder. b) The deconvoluted C 1s peak does not tell much other than that there is a large amount of C=C bonding and several components that are attributed to PMMA residue.

However, each graphene layer is almost exclusively monolayer so a transparency decrease of slightly over 2.3 % per layer is expected. Though these arguments are all coherent, experimental verification is much more valuable. Therefore OLEDs were produced with these graphene stacks as transparent electrodes, proving that both their conductivity and transparency made them suitable for applications.

4.3.2 OLEDs

The OLEDs were produced and measured by Philips Corporation. They developed a method of making OLEDs with graphene electrodes as part of the "Grafol" project. Photographs of the working devices produced with graphene stacks and their electronic characteristics are displayed in figure 4.7a)&b).

One of the most important parts to notice is that these OLEDs work at all without a planarisation layer. As the graphene has to be transferred from the growth catalyst to the OLED substrate, it usually exhibits significant surface roughness. The active layers deposited on it are often only 5 nm thick (see figure 4.3) meaning that a 10 nm tall fold can short-circuit the entire device. This can be avoided by

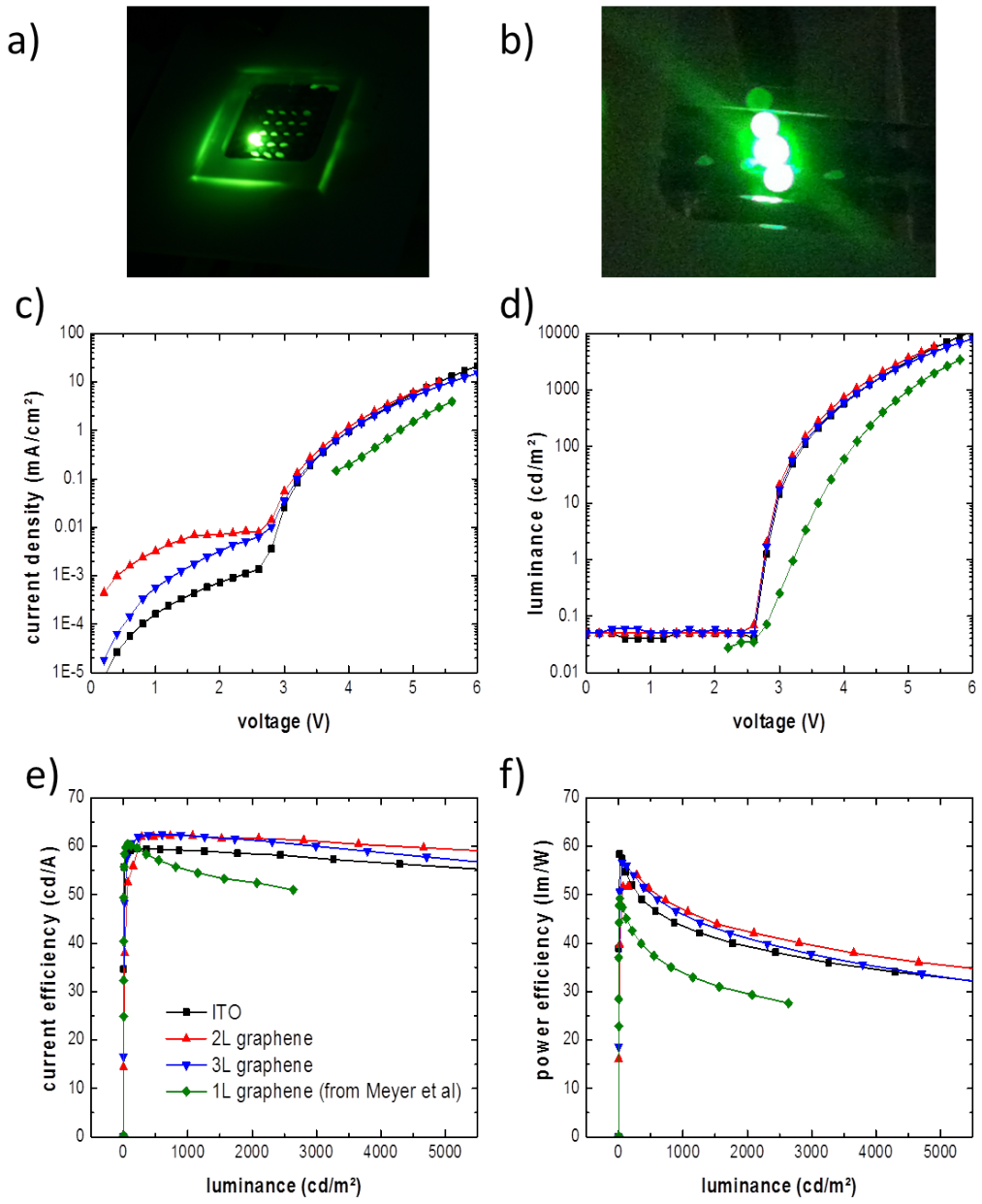

FIGURE 4.7: Performace of the OLEDs: a)&b) Photographs of the OLEDs performing. Intense green light is observed. c)-f) The electical performance of the OLEDs, comparing an ITO reference (black squares) to a two-layer and three-layer graphene stack electrode (red and blue). This is also compared to the performance of a monolayer graphene electrode from Meyer *et al.*'s publication. It is very evident that the two-layer graphene stack is superior to both the ITO and the other graphene stacks.

adding a 10s of nm thick planarisation layer that covers all of the graphene and presents one smooth surface to build on. This layer tends to consist of PEDOT:PSS (a conductive polymer mixture) that is be deposited in a wet-chemical step which is very expensive if everything else is evaporated. Many graphene OLEDs have been reported but they all require this planarisation layer that compensates for the film roughness and avoids short circuits.[135,180]

The graphs in figure 4.7c)-f) show a comparison between the different electrodes: Indium-tin oxide (ITO) which is the current industry standard, monolayer graphene from the publication of Meyer *et al.*, a two layer stack and a three layer stack fabricated by our modified stacking method.[130] The device structure used by Meyer *et al.* was not precisely the same, as it differed in some of the layer thicknesses, but it is the closest data that could be obtained. Even though there appears very little difference between the performance of the different graphene stacks, they are on par with ITO and the two layer stack performs best overall. This is likely because it has the best conductivity to transparency compromise of all the graphene electrodes. More importantly, the OLEDs produced with monolayer samples by Meyer *et al.* yielded less than half as many working devices than the 2 and 3 layer graphene stack based ones. This came from a private correspondence with Dr. Jens Meyer from Philips who made the OLEDs in both cases. However, not enough OLEDs were fabricated to allow for proper statistical analysis of yields.

The graph in figure 4.7c) shows the current density vs. voltage performance of the devices. A clear onset is observed around 2.7 V. Below this there was only leakage current with the ITO electrode showing the lowest of these. After the threshold is passed, the device actually emits light, as clearly seen in the luminance vs. voltage plot of figure 4.7d). The current efficiency vs. luminance plot in figure 4.7e) is extremely important as it shows that, with increasing luminance, the same amount of current goes into producing light and no other current-draining effects come in. Finally, the power efficiency vs. luminance plot in figure 4.7f) indicates that, at low luminance, the maximum amount of power is converted to light whereas at higher luminance other effects start consuming power. Those may be resistive heating or

other. However, the 2-layer graphene performs better than the industrial standard ITO.

This is a very important result as it shows that CVD graphene is not only good in theory, it can actually outperform indium-tin-oxide when it comes to electrical performance for optical devices. The reason for this may be due to the small area but that remains to be explored. Graphene has the additional advantage that it is flexible and can therefore be used in devices impossible to make with ITO. Overall the graphene OLEDs performed on par with some of the best ones published. They significantly outperformed the liquid-exfoliated graphene ones from ... and were on par with the CVD graphene ones by Meyer *et al.*, mainly because they were produced with the same method and tools.[130]

4.4 Conclusion

In summary, this chapter has shown that stacking CVD graphene the right way can produce much better functional devices than individual graphene monolayers. CVD graphene monolayers that are transferred from its growth catalyst appear to be of little use for the fabrication of effective oxygen diffusion barriers. Even several layers stacked on top of each other make no significant difference. The key issue with stacking appears to be polymer residue between the stacked layers but, by using the right method, this can be avoided. A stack of just three graphene layers, ∼1 nm thick, outperforms plastics 10,000 times thicker if it is assembled in the right fashion. This "right assembly" can be confirmed by Raman spectroscopy and XPS. Normalising the graphene's performance to thickness shows the graphene is on par with, if not better than, commercially used metal oxides like SiO_2 and Al_2O_3. The graphene used in this study had small domains of only about ∼1 μm diameter, and although care was taken to make the grain boundaries tight, larger domains are expected to perform even better. Hence in future graphene should easily be able to outperform these oxides. However, the cost of upscaling graphene

compared to SiO_2 and Al_2O_3 is huge so it may remain for niche applications in biological or flexible settings.

Electrical performance is also enhanced by stacking in the right fashion, as shown by the OLED results. The OLEDs produced were some of the most efficient ones to date, although that is more owed to the device structure than the graphene as those with ITO electrodes performed very similarly. Not only are two graphene layers better than one, a stack of those is even better than ITO, the material used to make transparent OLED electrodes in LED and OLED screens. Once graphene barriers, whose feasibility has been conceptually shown, are capable of protecting OLEDs, they can also act as transparent electrode at the same time, thus saving processing steps in the fabrication of OLEDs. Replacing brittle glass and ITO as barrier and electrode respectively will allow for the fabrication of flexible OLEDs which has been envisioned for decades.

Chapter 5

Selectively enhanced Raman scattering from aromatic molecules in graphene stacks

This chapter is mainly covered in the publication of the same name: "Selectively enhanced Raman scattering from aromatic molecules in graphene stacks", *submitted to JMCC*, 2015.

5.1 Introduction

Surface-enhanced Raman scattering (SERS) and its sub-category graphene-enhanced Raman scattering (GERS) have been theoretically covered in section 2.5.5. SERS is a very useful mechanism for making visible the signals of molecules that are usually too weak to detect or systems that do not allow high laser power (like biological ones).[100] One of its mechanisms, the electromagnetic mechanism (EM), is well-understood. It works by producing a surface plasmon that strongly couples to the analyte and can be mathematically described.[101,103–106,108,181] That is, it can be calculated for a given system and at this point it is possible to buy metal nanoparticles that provide a pre-determined enhancement factor for a given

wavelength of light. The alternate mechanism, the so-called chemical mechanism (CM), covers all other enhancement mechanisms, which are quite a few.[111] Those may for example be electronic band-alignment or structural factors. There is no unified theory for the CM as many aspects classed under it may not be related at all. One aspect used for describing it for some 2D material systems is outlined in section 2.5.5. As it is several orders weaker than the EM, it was mostly ignored for a long time. However, it gained a lot of attention recently as it is exhibited by 2D materials which concurrently do not allow for the EM to occur.[109,114] That is because their plasmon frequency is in the terahertz region and Raman spectroscopy is done in the visible light region, far off this resonance.[110] Hence graphene and TMDs are excellent candidates for studying aspects of the CM. Studies have shown that GERS is affected by many different factors. Some of those are the number of graphene layers making up the substrate, the Fermi level, laser energy, proximity of the analyte to the surface, molecular orientation and matching rings in the molecular structure with the graphene's hexagonal lattice.[114–120] The work presented in this chapter adds another factor to this list, that of surrounding the analyte with the graphene. It appears that in some cases bringing an analyte in contact with two layers of graphene, in a "sandwich"-like arrangement, can bring about additional signal enhancement compared to an arrangement with just one graphene layer.

5.2 Experimental

Two perylene bisimide derivatives **I** and **II**, only differing in their end-groups, were used in this study. Their structures are shown in figure 5.1.

Graphene-perylene bisimide stack structures were produced as illustrated in figure 5.2. Monolayer graphene grown on copper by CVD as outlined in chapter 3 was pre-cleaned by mild sonication in acetone. It was subsequently covered with either molecule species **I** or **II** by dip-coating it in a pH 7 aqueous buffer solution containing 0.1 wt% of the respective molecule. This was soaked in water to

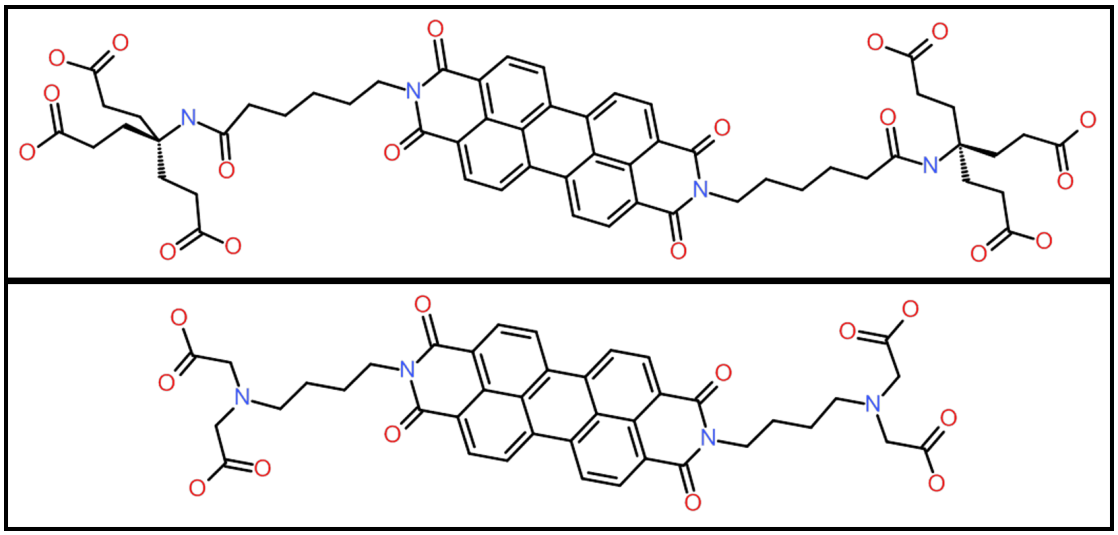

FIGURE 5.1: Structures of the perylene bisimide molecules used in this study. a) Molecule **I** and b) molecule **II**

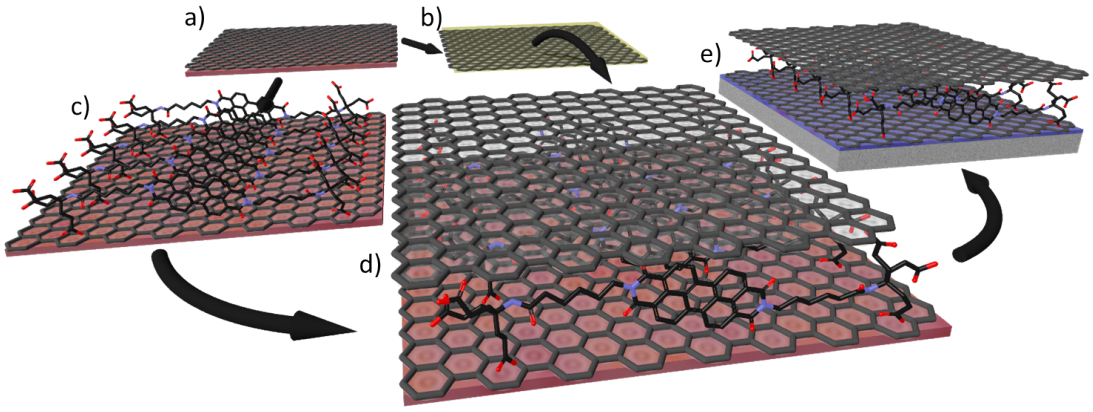

FIGURE 5.2: Schematic representation of graphene-perylene bisimide-graphene sandwich fabrication: a) CVD graphene is grown on coppper. b) The graphene is covered with transfer polymer and the copper substrate etched. c) A second piece of CVD graphene on copper is covered with either molecule **I** or **II** by dip-coating or solution-soaking. d) The graphene sheet from b) is transferred onto that from c), encapsulating the perylene bisimide molecules. e) This stack can subsequently be transferred to an arbitrary substrate like Si/SiO_2 or a TEM grid.

remove excess molecules from the graphene surface and leave only a single layer of molecules, a technique developed by Sinéad Winters and Nina Berner.[182,183]. Control samples without perylene bisimide molecules were also produced.
A second sheet of pre-cleaned graphene was transferred onto the first one by standard polymer-assisted transfer using cellulose acetate butyrate (3 wt% in ethyl-L-lactate). This was left to dry and completed the sandwich. The whole sandwich was then transferred to a substrate of choice, to Si/SiO_2 for Raman analysis and TEM grids for imaging purposes (in collaboration with group of Ute Kaiser, Ulm).

Areas inspected by Raman spectroscopy were those surrounding holes in one of the graphene layers as they allowed for direct comparison between the spectra of sandwiched molecules and those in contact with just one layer of graphene. The areas, shown in figure 5.4 were either 15×15 μm or 20×20 μm in size with 5000-15000 spectra taken.

5.3 Results & Discussion

The Raman spectrum of the perylene bisimide molecules on graphene was described in detail by Kozhemyakina *et al.*[61] As a thin layer (ideally monolayer) on graphene transferred to 300 nm Si/SiO_2 both molecule **I** and **II** exhibit a similar Raman spectrum as it is mostly caused by vibrations in the aromatic core of the molecule and the different end-groups only contribute much weaker signals. A representative spectrum of molecule **II** on monolayer graphene is shown in figure 5.3. There are two very strong signals from the molecule's core at $\sim$1300 cm^{-1} (Per-a) and $\sim$1380 cm^{-1} (Per-b), which are usually of similar strength, one slightly weaker signal at $\sim$1580 cm^{-1} (Per-c) and many weak signals from the end-groups in the region of $2550 - 3000$ cm^{-1} (Per-d). Additionally, a fluorescence background can be observed in the case of multilayer coverage, since the molecules' inherent fluorescence is only quenched in the immediate vicinity of graphene. It is important to note that the peak at 1580 cm^{-1} and the series of peaks between 2550 cm^{-1} and 3000 cm^{-1} are strong enough to at least partially overpower graphene's G

and 2D peak which are also found in those locations, respectively. Without the graphene substrate neither molecule exhibits a well-detectable Raman spectrum so both display some GERS.

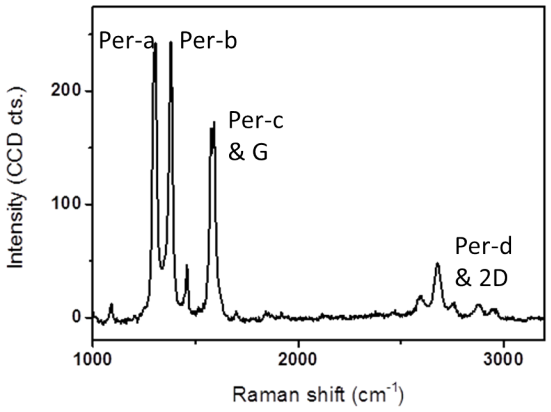

FIGURE 5.3: Representative spectrum of molecule **II** on graphene (molecule **I** exhibits almost the same spectrum). The strong signals at ∼1300 cm^{-1} (Per-a) and ∼1380 cm^{-1} (Per-b) are the most dominant. The sligthly weaker signal at ∼1580 cm^{-1} (Per-c) is in the same position as the graphene's G peak but stronger. Also the peaks between ∼2550 cm^{-1} and ∼3000 cm^{-1} (Per-d) are stronger than the graphene's 2D signal at ∼2700 cm^{-1}, therefore masking it.

On a single layer of graphene, molecules **I** and **II** showed very similar Raman spectra in terms of peak positioning. However, upon application of the second graphene layer to produce a "sandwich", the Raman signals changed. The changes are summarised in figure 5.4. The figure shows an optical image of each sample, a histogram of the peak intensity at 1580 cm^{-1} (G signal and Per-c mixed) and a histogram of the peak intensity at 1300-1380 cm^{-1} (Per-a & Per-b). The histograms allow for easy detection of abnormalities in signal intensities.

Firstly, a control sample of two graphene layers without sandwiched molecules shows that the graphene's G peak intensity increased when sandwiched with respect to the monolayer area (figure 5.4a) & f)). This is evident from the histogram in figure 5.4f) which shows two distinct peaks, indicating that there are two main signal strengths with a ratio of about 1.85. This effect was anticipated as double the graphene should give double the signal, minus a small amount due to absorption.[184]

Sandwiching molecule **I** did not appear to yield any change even though there are optically two regions visible (figure 5.4b)). Neither the histogram of signal

strength in the G & Per-c band region (figure 5.4g)) nor that of the Per-a & Per-b region (figure 5.4k)) shows more than one feature. The fact that the G band region does not show two features even though the control sample did implies that the perylene's signal at that point, Per-c, is much stronger than the graphene's G band.

Molecule **II** however, exhibited an unexpected behaviour upon sandwiching: In contrast to molecule **I**, both peaks monitored increased in intensity in the sandwiched regions. This is shown in the intensity histogram of the G & Per-c peak region (figure 5.4h)) and the Per-a & Per-b peak region (figure 5.4l)). The intensity of the G & Per-c signal region increases by a factor of ∼4.5 while the Per-a & Per-b signals' intensities have a ratio of ∼4.7 which cannot be explained by structural features alone.

To investigate whether it was only the Raman signal of molecule **II** that got enhanced by sandwiching or whether the graphene's signal was also altered, graphene made from ^{13}C instead of ^{12}C was used. This was purpose-synthesised using methane containing 100 % ^{13}C in a method similar to that originally published by Li *et al.* in a hot-walled tube furnace of 4 cm diameter on the same type of copper as used in chapter 3.[35] The heavier isotope changes the position of the G peak from 1583 cm^{-1} to 1525 cm^{-1}, a position where the perylene does not have any signal intensity and therefore decouples the G and Per-c signals.[112] A sandwich with molecule **II** made from this heavier graphene is shown in figure 5.4d). The G peak intensity histogram (figure 5.4i)) shows only a 1.76-fold increase of signal strength for the sandwiched regions, similar to the pure-graphene control. Hence the graphene is unaffected by this additional enhancement and it is only molecule **II**'s signal strength that is affected.

For SERS even a small change in structure or energy can have a huge impact on the enhancement and the difference from a protonated acid group may suffice to bring such a change about. The perylene bisimide molecules were deposited from a pH 7 solution which likely left their carboxylic acid groups partially deprotonated. By transferring in low pH the acid groups were expected to be protonated, providing a slightly different molecule into the sandwich. Transferring molecule **II**

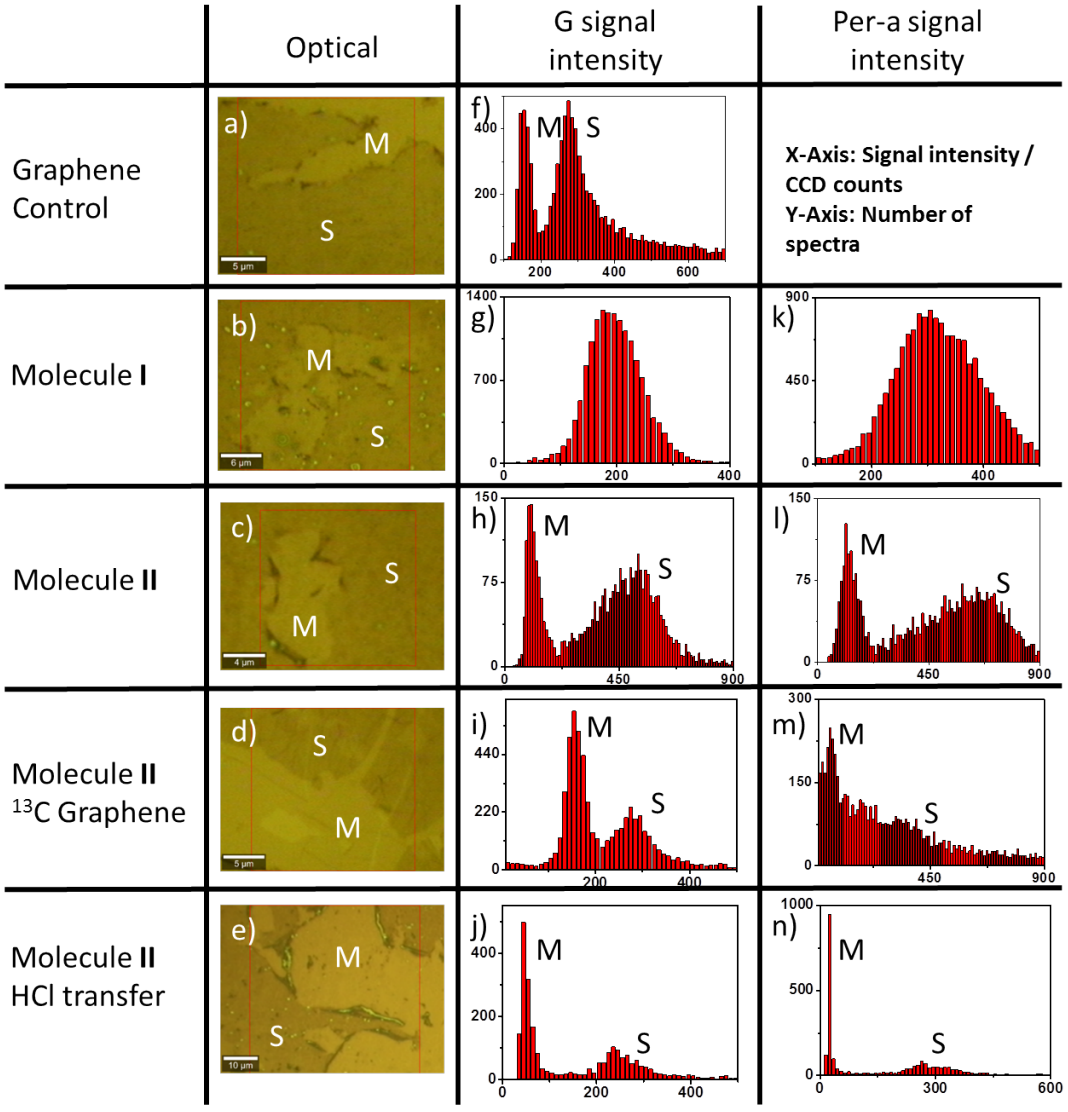

FIGURE 5.4: Areas analysed by scanning Raman spectroscopy and histograms of peak intensities. a)-e) Optical images of the areas scanned which show both monolayer and stacked areas and allow for side-by-side comparison. Monolayer graphene areas are indicated by **M**, turbostratically stacked areas are marked with **S**. f)-j) Histograms of G peak intensities around 1580 cm^{-1} except for the ^{13}C sample in i) where the signal is situated at 1525 cm^{-1}. k)-n) The Per signal histograms show the distribution of signal intensity for the peak situated at ∼1300 cm^{-1} (Per-a) which tends to have the same intensity as the one at 1380 cm^{-1}. On both the G peak and Per-a peak histograms the origin of features is marked with **M** or **S** to indicate what region in the corresponding optical image it stems from.

this way left the stack much more damaged (figure 5.4e)). It also appears to have given an even greater intensity enhancement of both signals investigated. The G & Per-c signal region (figure 5.4j)) showed an enhancement of factor 5.13 for the sandwiched regions and the Per-a & Per-b an enhancement factor of 11.3 (figure 5.4n)). However, that ratio may be exaggerated as the signal of lower intensity was very weak and hence provides more room for error.

It was not possible to identify any theory published to date that can provide a straightforward explanation for the effect observed here. Many recent publications about SERS and GERS stress the importance of aligning the molecule's HOMO or LUMO energy levels with the graphene's Dirac point and/or Fermi level (if different) in order to gain strong Raman signal enhancement.[109] The two molecules tested in this study were structurally very similar but not identical and therefore electronic energy level differences are likely to be the cause of this. This is also supported by the change in enhancement upon full protonation of the carboxylic acid groups of molecule **II**. The protonation results in a small alteration in electronic structure that lead to a vast change in the enhancement amplitude which is in line with an energy-level alignment theory. It could also be possible that the different environments of the two graphene sheets (SiO_2 for the bottom one, polymer residue for the top one) created a favourable Raman enhancing environment for molecule **II** and not molecule **I** but that is purely speculative and, like the previous argument, requires theoretical studies.

5.4 Conclusion

In summary, this chapter presents a new type of GERS effect. It is generated by "sandwiching" molecules between two graphene layers. This effect works in addition to other GERS effects and increases of factors up to 11 were observed. However, though strongly exhibited for one molecule, it is completely absent for a different yet structurally similar molecule. Currently no straightforward theory explaining this effect could be identified but once this effect is understood it can

be used to improve analysis of sensitive molecules that can be protected inside graphene sandwiches.

Chapter 6

Layer-selective and seeded ALD of Al_2O_3 on MoS_2 and WS_2

This chapter describes a study of Al_2O_3 ALD on TMDs. Parts of the chapter's contents have been published in the paper "Atomic layer deposition on 2D transition metal chalcogenides: Layer dependent reactivity and seeding with organic ad-layers", *Chemical Communications*, **2015**, *published online 24 Sep 2015* [185]

6.1 Introduction

The outstanding properties of TMDs make them candidates for exciting future technologies and their integration into existing semiconductor technology is of major interest (see section 1.2).[41,46] This integration requires them to be fully CMOS processable which is not trivial. One prerequisite for this is reliable and scalable synthesis, an area that has seen many improvements over recent years and enabled the fabrication of many interesting devices, but only on a laboratory scale.[44,186–188] Another CMOS requirement is the deposition of subsequent layers on top of the TMD. This is necessary for applying gate dielectrics or passivation layers in order to ensure performance stability. Achieving reliable deposition on 2D layers is non-trivial as any impact, for example from sputtering or a chemical

functionalisation technique like PECVD, will result in alteration if not destruction of the TMD's electronic structure. So far it has been shown that encapsulation of the 2D TMD by mechanical exfoliation and deposition of hexagonal boron nitride yields the best preservation of its electronic properties but this approach is not scalable.[48] Maybe it will be possible to use large-area CVD grown h-BN to the same effect but that remains yet to be shown.

Encapsulation of MoS_2 and WS_2 devices for protection from oxygen and moisture is vital. It is not a popular fact and very few publications mention it but these materials are thermodynamically unstable with respect to oxygen and will decompose over relatively short time frames of a few days to weeks.[189] As shown in chapter 4, graphene may someday make a good barrier but is not there yet. A material that is a good barrier is Al_2O_3. Deposition of thin layers of Al_2O_3 may be a very good method of protecting these materials.

Atomic layer deposition (see section 2.2) can very precisely and conformally deposit thin films at Ångström control levels.[190,191] It is a very commonly used technique in microchip fabrication and is one of the main technologies that enabled the rapid shrinking of transistors over time. Therefore it is a technique with which TMDs have to be compatible to allow their integration into technology. A major obstacle to achieving this compatibility is the inert basal plane of most 2D materials which prevents the ALD precursors from anchoring and sticking to the surface as it is not possible to form a covalent chemical bond to the substrate. Using a wetting layer would be the normal approach in this case but the wetting agent for Al_2O_3 is usually ozone which may damage the TMDs as they are thermodynamically unstable with respect to oxygen and water so a different agent has to be used which is discussed later. Several attempts of Al_2O_3 ALD on TMDs have been made already by researchers but while great successes were reported, those have not shown great reproducibility, even under apparently similar conditions. Hence no reliable process has been shown to date.[192–194]

On graphene, similar problems were initially encountered. Its unreactive nature leads to deposition at grain boundaries only or irregular deposition at best.[195]

Transferred graphene has polymer residue which can function as anchor but is not reliable.[155] One method that workes is ALD on CVD grown graphene that was still on the metal catalyst. The polar water, one of the precursors in Al_2O_3 ALD, can physisorb on that system and lead to the start of the reaction.[196] Alternatively ozone can be used as wetting agent and start the reaction.[197] Many studies showed that deposition of small organic molecules with -OH and -COOH groups works well as wetting layer but those may lead to doping and have to be handled with care.[198,199]

The work presented here deals with two aspects of Al_2O_3 ALD on MoS_2 and WS_2. Firstly, it is established that the adsorption dependent ALD of Al_2O_3 from TMA and H_2O is layer-selective on single crystalline TMDs under certain conditions. Secondly, to ensure uniform deposition for cases when layer-selectivity is not desired, the TMDs can be non-covalently functionalised with perylene bisimides which provide anchor units to start the ALD and enable non-discriminate deposition.

6.2 Experimental

Single crystalline layers of MoS_2 and WS_2 were grown on 300 nm Si/SiO_2 substrates and provided by Maria O'Brien according to the exprimental conditions outlined in her publication.[51] These samples showed the characteristic triangular shape and consisted of mostly monolayer except for the flake centre which occasionally exhibited an onset of multilayer growth as shown in figure 6.1. The flake diameters varied from few μm up to 100 μm while the monolayers were 0.7 nm thick and each subsequent layer added another 0.7 nm. ALD was performed using TMA and H_2O precursors, with 0.5 s exposure followed by 20 s N_2 flow at 60 sccm. 27 cycles were used, aiming for a 3 nm thick coating. This occurred at a temperature of 80 °C.

For the reactions when a wetting layer was applied, perylene bisimides were deposited by dip-coating the TMD into a 0.1 wt% pH7 phosphate-buffered aqueous

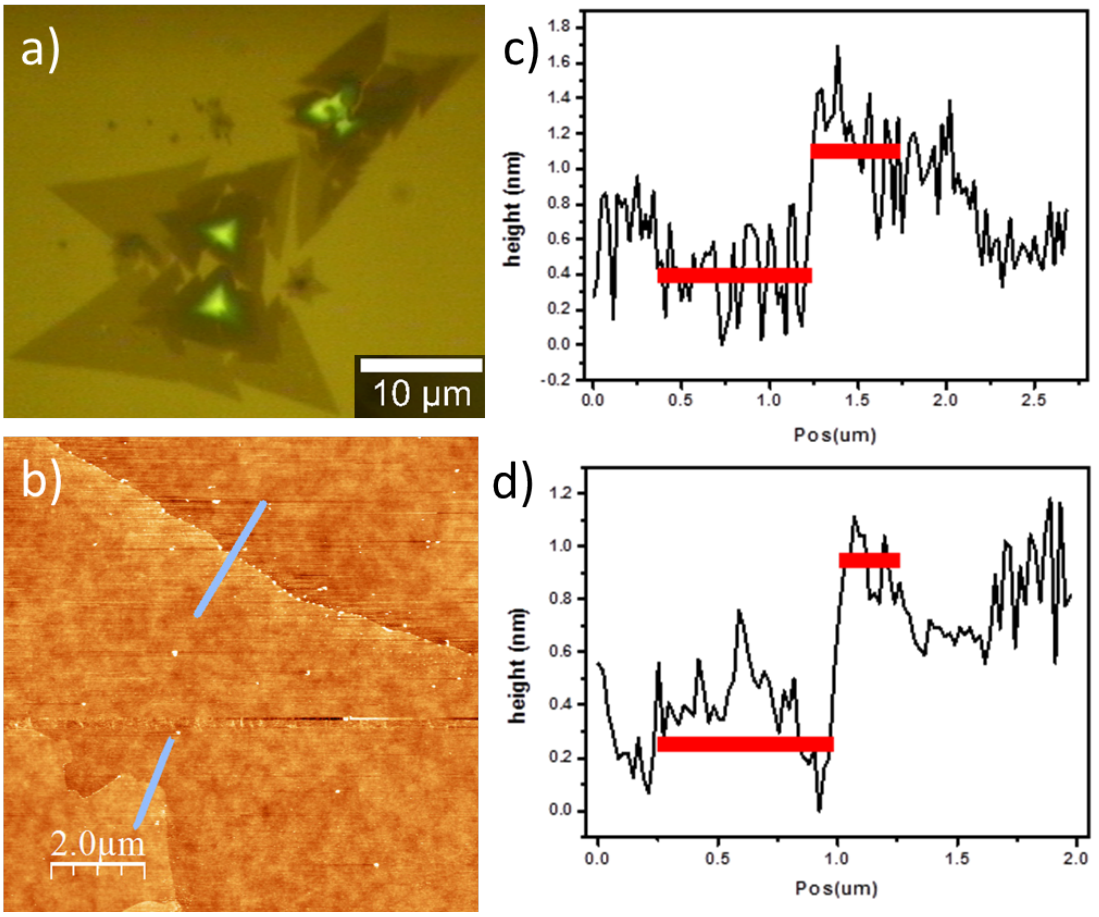

FIGURE 6.1: Representative WS_2 flake used in this study. a) Optical image of triangular flakes on Si/SiO_2. They are mostly monolayer but more centres are found at the flake centres. b) Topography AFM scan of part of a flake. c) and d) show the line profiles of the lines marked in b) and show step heights of 0.7 nm, corresponding to the literature step heights for WS_2.

solution containing the perylene bisimides and subsequent washing with water to remove physisorbed multilayers.[182,183]

6.3 Results & Discussion

6.3.1 Layer-selective ALD

In figure 6.2a) an AFM image of a triangular WS_2 flake after 3 nm Al_2O_3 non-seeded ALD is presented. It is apparent that the triangular flake (dark region) is lower than the surrounding substrate. This is more clearly illustrated by the

line scan in figure 6.2b). The step height between the substrate and the flake is ∼2.3 nm after deposition, perfectly corresponding to the difference between 3 nm Al_2O_3 and 0.7 nm WS_2 flake height. Hence it is evident that no Al_2O_3 deposition occurred on the TMD monolayer. The double layered centre of the flake increased in height to ∼3.7 nm with respect to the monolayer region, corresponding perfectly to 0.7nm flake height plus 3 nm Al_2O_3. The edge of the monolayer was decorated with Al_2O_3 nanoparticles which can be attributed to dangling bonds and defects which are more reactive. It may be possible that the deposition of Al_2O_3 on the bilayer part was in a Volmer-Weber mechanism, where individual nanoparticles are seeded on the surface and slowly grow together, rather than a Franck-van-der-Merve growth which is uniform film growth. However, the nanoparticles would have to be closer spaced than the AFM tip's lateral resolution in order to appear uniform which is a distance of about 30 nm all across the surface. Certainty would be found either by doing STM or conductive AFM measurements.

This selectivity was found to exist for both MoS_2 and WS_2 single crystals grown via CVD. The absence of growth on the monolayer is partially expected as it is also observed for graphene. However, the complete coverage of the TMD bilayer is unexpected as even a thick HOPG crystal, does not allow for Al_2O_3 growth under those conditions.[200] The selectivity is attributed to two factors: Firstly, the films used must be extremely clean and crystalline. Any defects would act as nucleation centres and a single dangling bond would be enough to seed Al_2O_3 deposition as is observed at the flake edges. The fact that the films were processed on their growth substrate and did not require transfer eliminates the possibility of polymer residue, something that may account for the discrepancies between published studies on mechanically exfoliated TMDs.

Secondly, TMDs undergo a significant change in electronic structure when going from bulk to multilayers and then single layer.[42,45] There is a change from an indirect optical bandgap of 1.2 eV and 1.3 eV to a direct bandgap of 1.9 eV and 2 eV for MoS_2 and WS_2, respectively.[201,202] Therefore the initially adsorption-based ALD may be so heavily influenced by this difference in underlying electronic structure that it is significanly different for monolayers in comparison to bulk. However,

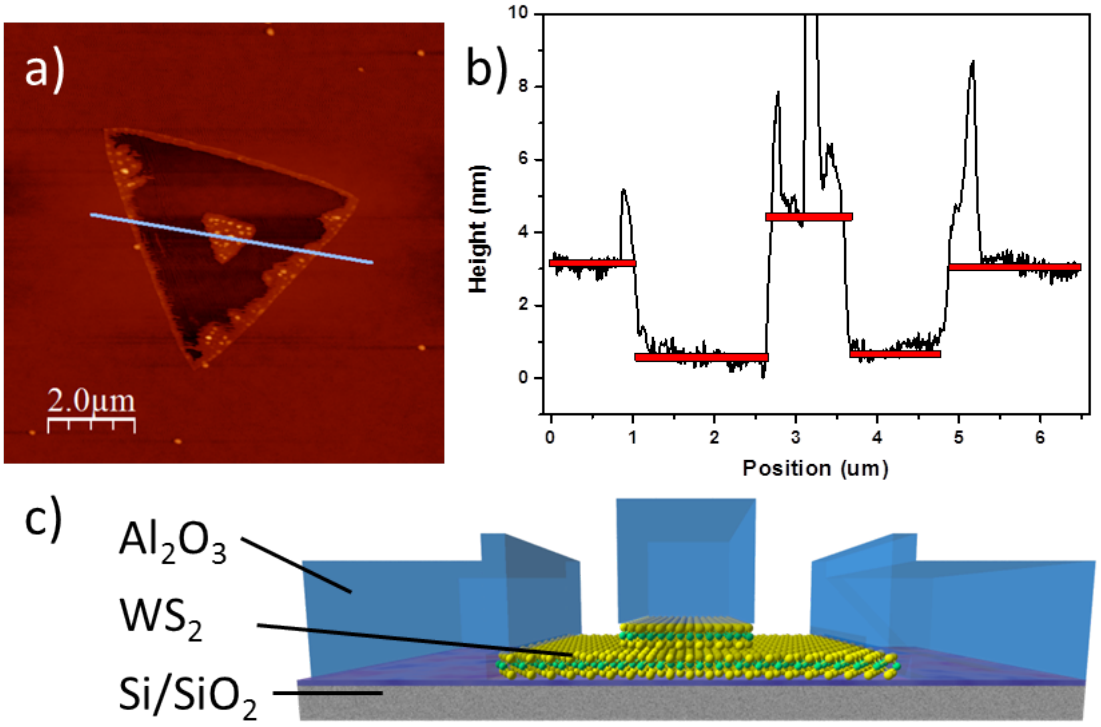

FIGURE 6.2: Topography of a WS_2 flake after standard ALD. a) The topography map shows that the flake is now lying lower than the surrounding substrate. b) The topography line scan across the flake shows that the surrounding substrate of Si/SiO_2 is 2.3 nm higher than the monolayer regions and the flake centre is 3.7 nm higher than the monolayer. c) This shows a schematic explanation of the topography scan in b).

this is just one theory and the exact mechanism and adsorption energies will have to be theoretically modelled. For a start, a Lennard-Jones potential could suffice to indicate whether or not the polar water or the non-polar TMA show different adsorption characteristics on MoS_2 and WS_2 monolayer vs. bilayer. If that is not sufficient a more complicated model will have to be used.

This selectivity can be a significant advantage: Covering all layers but the monolayer with a dielectric leaves only the material with the direct bandgap exposed. This provides a novel pathway to select monolayer regions and can be used for vertical device fabrication and selective chemistry.

Raman spectroscopy can investigate some impacts on the TMDs electronic structure from this deposition effect as doping, partial substitution or destruction of the material can lead to peak shifts in its spectrum. Both MoS_2 and WS_2 have two closely spaced peaks in the region of 400 cm^{-1}, shown for MoS_2 in figure 6.3d).

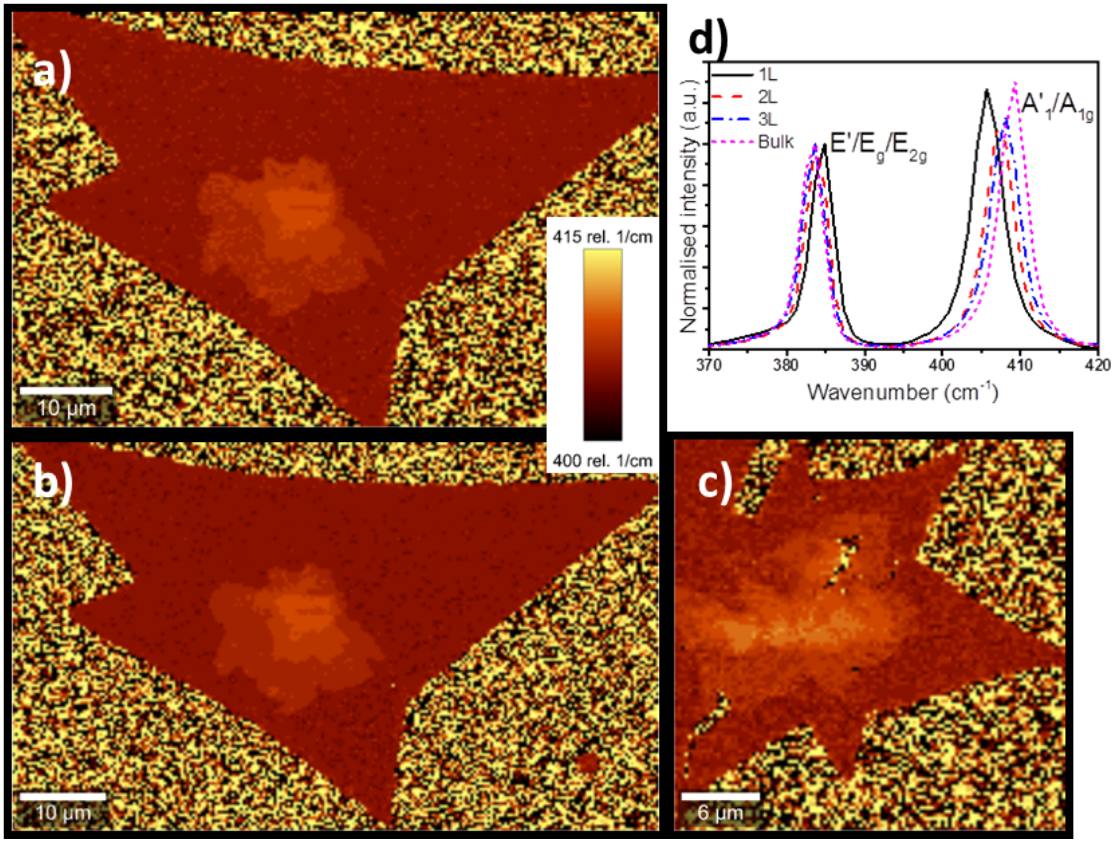

FIGURE 6.3: Scanning Raman spectroscopy of MoS_2. a) The peak position of the A'$_1$ Raman signal of pristine MoS_2. b) Scan of the same flake as in a) after application of 27 cycles ALD. There is no easily visible change. c) Position of the A'$_1$ peak after application of perylene bisimide and 27 cycles ALD. There appears to be a small blueshift but this is at the spectrometer's resolution limit. d) Raman spectrum of MoS_2 indicating the different regions, monolayer, bilayer, trilayer and bulk.

Any changes in molecular or electronic structure due to Al_2O_3 deposition will result in an alteration of these two signals. More specifically, a shift in the position of the A'$_1$/A$_{1g}$ peak indicates electronic doping.[43,99] Figure 6.3a) shows a map of the position of the A'$_1$/A$_{1g}$ peak maximum for a sample straight out of synthesis. The peak shift with layer number is very well visible and according to literature. In figure 6.3b) the same flake is scanned after exposure to 27 cycles ALD. No significant change is visible so the electronic structure of both the multilayer centre (covered with Al_2O_3) and the monolayer flake (not covered with Al_2O_3) appears unperturbed. However, the spectrometer's resolution is only $\sim$1 cm^{-1} so smaller changes may have gone undetected.

6.3.2 Seeded ALD

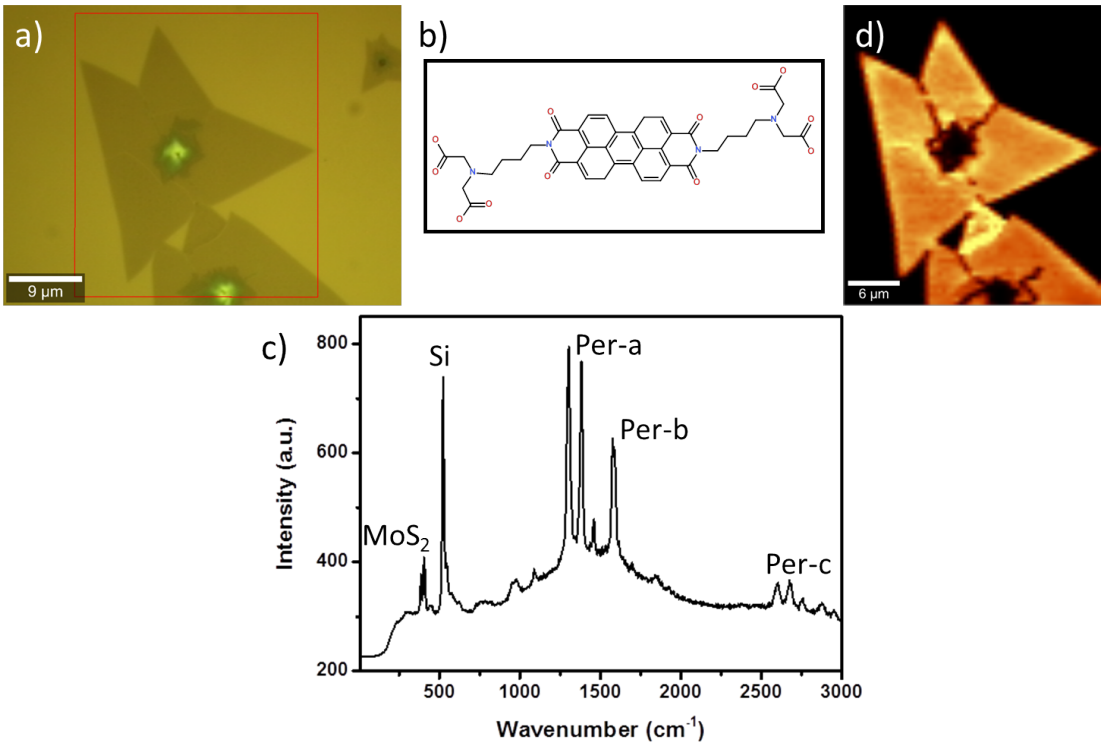

FIGURE 6.4: Raman spectroscopy of the perylene bisimide functionalised MoS_2. a) Optical micrograph of the MoS_2 flake investigated after functionalisation. b) Structure of the perylene bisimide used for functionalisation. c) Average Raman spectrum of the area outlined in red in a). The individual peaks are identified as the signals from MoS_2, Si and the perylene, confirming the perylene's presence. d) A map of the Per-a signal intensity shows that it is strongly present on the MoS_2 flakes. No perylene signal is observed from the SiO_2 surface.

The selective deposition of Al_2O_3 on TMDs is a very important discovery and enables new types of devices previously impossible. For example, it allows for CVD growth of large areas of TMD, subsequent coverage of the non-direct bandgap parts and then uniform contacting of the monolayer to make a vertical, optically active device like a LED or photodiode. However, deposition of uniform dielectrics on monolayer TMDs is desired for passivation and some electronic device fabrication. For those kind of devices the selectivity is a hinderance, especially if monolayer devices are required. Non-covalent functionalisation of TMD basal planes with molecules that contain $-$OH and $-$COOH units that can react with TMA and thereby seed the reaction for Al_2O_3 are a solution to this problem.[190,203]

Seeding with perylene bisimides has been reported on graphene and they have been shown to form stable layers on it (as also shown in chapter 5).[198,204] This makes them good canditates for doing this work on TMDs. The perylene derivative used in this study is shown in figure 6.4b). It has long end-groups with $-COOH$ groups that can seed the deposition and is easily deposited by dip-coating.[199] The successful functionalisation is confirmed by Raman spectroscopy, shown in figure 6.4c). In figure 6.4c) it is observed that the perylene signal is homogeneous on the MoS_2 monolayers but no perylene signal from the SiO_2 substrate is observed.

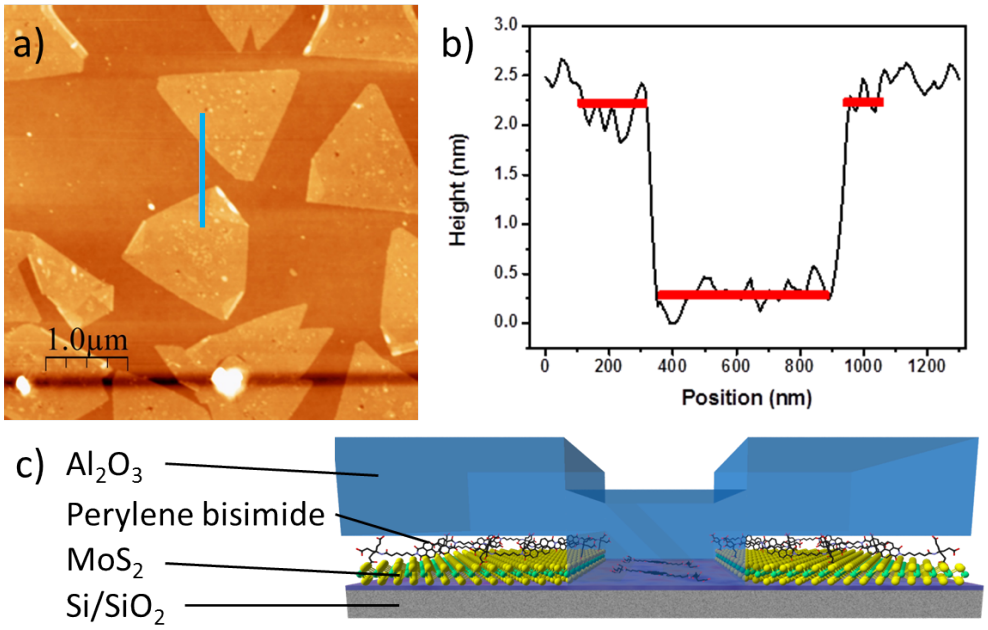

FIGURE 6.5: Analysis of MoS_2 flakes after seeded ALD. a) AFM topography scan of MoS_2 monolayer flakes after perylene-seeded ALD. b) Cross-section of the topology along the blue line in a). The step height is 1.9 nm. c) Schematic representation of what the surface cross-section looks like.

As shown in figure 6.5a), ALD on a perylene-functionalised sample leads to a continuous deposition of Al_2O_3 on all layers of MoS_2, regardless of the number of layers underneath. The topography scan shows the triangles above the substrate, as would be expected. The topological cross-section in figure 6.5b) reveals that the step height between MoS_2 flake and SiO_2 substrate is not 0.7 nm any more but $\sim$1.9 nm. This is consistent across the whole surface of the TMD and shows

that the perylene coating is homogeneous, leading to the suggested surface cross-section shown in figure 6.5c). The additional height difference of 1.2 nm implies that there is more perylene bisimide on the TMDs than on SiO_2 and that it may be in an upright conformation rather than lying flat as its structure may suggest. This will require further investigation, ideally by STM.

Raman mapping the MoS_2's A'_1/A_{1g} peak (figure 6.3c)) after ALD shows that the TMD is not damaged by the deposition and retains its characteristics although there is a minor blueshift of $\sim$1 cm^{-1}, potentially indicating p-doping.[205] As this is at the spectrometer's resolution limit it is uncertain. However, in order to ascertain the real impact on the electronic properties, electric measurements on a FET or Hall bar device are required. This is not trivial but will provide the ultimate proof as to whether this way of protecting TMDs is valuable or not.

6.4 Conclusions

Overall, the study represented in this chapter is the first observation of selective chemistry on monolayer TMD surfaces over their multilayer counterparts. It shows that this can be used to selectively deposit Al_2O_3, providing a method of masking all areas but monolayer MoS_2 or WS_2. Furthermore, an easily accessible method of non-covalent functionalisation with a perylene bisimide derivative allows for reliable ALD of Al_2O_3 on monolayer TMDs without significant damage to their electronic integrity as assessed by Raman spectroscopy. These two findings provide significant advancement in the knowledge necessary for fully integrating TMDs in real devices.

Chapter 7

Conclusions and future outlook

This thesis mainly presented studies regarding graphene. Only chapter 6 does not concern studies involving graphene. An initial study involved the synthesis of graphene via CVD. The aim of the study was to reduce the temperature of the graphene growth on copper from 1035 °C in order to reduce copper sublimation and make the growth more accessible to tools that cannot reach >1000 °C. Ethene was employed as a more reactive carbon precursor than methane and the parameter space of the tool was navigated using statistical methods which focused on optimising the width of the graphene's Raman 2D signal. Quality analysis was performed with Raman spectroscopy, SEM and electrical characterisation. In the end, large-area, uniform, reproducible graphene was synthesised at 850 °C with flake sizes of 1 μm diameter, a 2.75/1 2D/G Raman signal intensity ratio on SiO_2 and hole and electron mobilities of 1100 $cm^2V^{-1}s^{-1}$ and 700 $cm^2V^{-1}s^{-1}$, respectively, which is very promising for many applications. A pre-growth patterning method using Al_2O_3 deposited by ALD was also developed and used successfully.

This enabled the facile fabrication of GFETs which yielded the charge-carrier mobilities. Stripes of graphene, 10 μm wide but several cm long were made that way and provided as transparent, flexible, biocompatible electrodes for neural studies which unfortunately did not proceed.

This large-area graphene was subsequently employed to make gas barriers. Following some improvements of the transfer process made by colleagues, the graphene was successfully stacked in a way that avoided polymer residues between layers and yielded an air-tight configuration. Oxygen permeation studies found that a 5 cm^2 graphene film of ∼1 nm thickness performed on par with 150 μm PET. Normalised to thickness, this yielded an inherent barrier performance of 1.10×10^{-7} barrer which is as good as if not better than commonly used barrier materials like SiO_2 and Al_2O_3. This is in stark contrast to any findings that had been published and represented an improvement of a factor of 5000 over the state of the art, strongly contradicting studies that had concluded that graphene would not make a good large-area barrier film. Even though graphene barriers are more expensive to produce than SiO_2 or Al_2O_3 barriers, its combination of transparency, flexibility, electrical and thermal conductivity and biocompatibility gives it a distinct advantage over these materials and may hence lead to the incorporation of graphene into specialised devices. On the mass-production market it is unlikely to find an application simply because of the cost and upscalability issues beyond a few m^2.

This usefulness was demonstrated in the making of OLEDs. Together with Philips corporation as part of the Grafol project graphene stacks were shown to outperform ITO as OLED electrode. Stacked electrodes were slightly better than monolayer electrodes in terms of performance but much better in terms of device fabrication yield. The use of cellulose acetate as transfer polymer enabled a very flat transfer which did not require a planarisation layer, saving an expensive step that is often necessary when dealing with transferred graphene.

The modifications in stacking methods developed for the barrier studies provide a simple method for intercalating species between graphene layers. Intercalating perylene bisimide derivatives led to some very interesting and previously unobserved effects in the Raman spectra of these perylenes: Intercalation led to a significant enhancement of one perylene's Raman spectrum by a factor of ∼4, and up to ∼11 with some modification, whereas a similar but slighly different perylene did not show this effect. This is unexpected as both perylene derivatives studied already showed a graphene enhanced effect but only one could be enhanced even

further. Slight modifications of the enhanced species by fully protonating its carboxylic acid end groups led to an even greater enhancement, implying that this effect is highly sensitive to structural changes. Theoretical studies will be required to fully explain this effect in future. More molecular species also need to be tested to investigate whether this effect is the exception or the rule. Such a study is currently being executed.

The final section of this thesis focuses on ALD of Al_2O_3 on MoS_2 and WS_2, materials that will play an important part in future technologies. Their integration into modern technologies requires compatibility with processes like ALD. This study found that, when using pristine single-crystal monolayer films grown by CVD, Al_2O_3 cannot been grown on the TMDs by ALD from TMA and H_2O. Only on two or more layers does the material deposit in the expected fashion. This provides a unique chemical pathway for extracting the monolayer regions from a mixture of layered regions. These can be used for vertical device structures and other applications that require the direct-gap monolayer only. Total coverage can also be achieved by seeding the reaction with a perylene bisimide derivative with carboxylic acid groups. This molecule can non-covalently attach to the TMD and lead to reliable deposition of Al_2O_3, even on monolayer films. This work paves the way for vertical devices involving monolayer TMDs and passivation for electronic applications.

The message to take from this thesis is that it is indeed possible to upscale the use of graphene and TMDs into existing technology. Their potentially useful properties like high conductivity, chemical inertness, extremely high sensitivity, odd quantum effects and barrier feasibility were discovered and confirmed several years ago but their integration is slow. The work presented here shows that this integration is possible and there are still many fundamental things to learn. That said, these materials face a lot of competition and materials like silicon and III-V semiconductors have a significant headstart of 40 years which may never be caught up. However, we will never know if we do not try.

Some immediate, mid-term future work emerges from this thesis: In particular, the Raman effects observed in chapter 5 leave many open questions. Theoretical modelling should provide some answers in terms of band alignment and resonance that may lead to the effect. A study concerning many more species of intercalated molecules will also give a greater insight into whether this effect is common or exceptional. The work leading on from the selectively masked TMDs in chapter 6 also shows great potential for future work. Vertical heterojunctions involving TMDs are an important field of study and this selective masking of multilayer is a key enabler for making large areas of such heterojunctions. Additionally, the reliable encapsulation of TMDs after seeded ALD levels the path for work on electronic devices. The feasibility of graphene-based barriers is still not very clear and is worthy of further investigation. Films with larger flakes may make even better barriers and find applications in specialised devices like biomedical systems.

Altogether it can be said that this thesis is a step forward in the realisation of 2D devices in our lives.

Bibliography

[1] A. K. Geim and K. S. Novoselov, *Nature Materials*, 2007, **6**, 183–191.

[2] P. R. Wallace, *Physical Review*, 1947, **71**, 622–634.

[3] K. S. Novoselov, A. K. Geim, S. V. Morozov, D. Jiang, Y. Zhang, S. V. Dubonos, I. V. Grigorieva and A. A. Firsov, *Science*, 2004, **306**, 666–669.

[4] K. S. Novoselov, D. Jiang, F. Schedin, T. J. Booth, V. V. Khotkevich, S. V. Morozov and A. K. Geim, *Proc Natl Acad Sci U S A*, 2005, **102**, 10451–3.

[5] C. for Physics of the Royal Swedish Academy of Sciences, *Scientific background on the Nobel Prize in physics 2010: Graphene*, Royal swedish academy of sciences technical report, 2010.

[6] S. V. Morozov, K. S. Novoselov, M. I. Katsnelson, F. Schedin, D. C. Elias, J. A. Jaszczak and A. K. Geim, *Physical Review Letters*, 2008, **100**, 016602.

[7] A. A. Balandin, S. Ghosh, W. Z. Bao, I. Calizo, D. Teweldebrhan, F. Miao and C. N. Lau, *Nano Letters*, 2008, **8**, 902–907.

[8] R. R. Nair, P. Blake, A. N. Grigorenko, K. S. Novoselov, T. J. Booth, T. Stauber, N. M. R. Peres and A. K. Geim, *Science*, 2008, **320**, 1308–1308.

[9] C. Lee, X. D. Wei, J. W. Kysar and J. Hone, *Science*, 2008, **321**, 385–388.

[10] K. S. Novoselov, A. K. Geim, S. V. Morozov, D. Jiang, M. I. Katsnelson, I. V. Grigorieva, S. V. Dubonos and A. A. Firsov, *Nature*, 2005, **438**, 197–200.

[11] Y. B. Zhang, Y. W. Tan, H. L. Stormer and P. Kim, *Nature*, 2005, **438**, 201–204.

[12] K. Novoselov and A. Geim, *Materials Technology*, 2007, **22**, 178–179.

[13] F. Schedin, A. K. Geim, S. V. Morozov, E. W. Hill, P. Blake, M. I. Katsnelson and K. S. Novoselov, *Nature Materials*, 2007, **6**, 652–655.

[14] J. S. Bunch, S. S. Verbridge, J. S. Alden, A. M. van der Zande, J. M. Parpia, H. G. Craighead and P. L. McEuen, *Nano Letters*, 2008, **8**, 2458–2462.

[15] K. S. Novoselov, V. I. Fal'ko, L. Colombo, P. R. Gellert, M. G. Schwab and K. Kim, *Nature*, 2012, **490**, 192–200.

[16] V. Georgakilas, M. Otyepka, A. B. Bourlinos, V. Chandra, N. Kim, K. C. Kemp, P. Hobza, R. Zboril and K. S. Kim, *Chemical Reviews*, 2012, **112**, 6156–6214.

[17] N. S. Green and M. L. Norton, *Analytica Chimica Acta*, 2015, **853**, 127 – 142.

[18] V. Chabot, D. Higgins, A. Yu, X. Xiao, Z. Chen and J. Zhang, *Energy Environ. Sci.*, 2014, **7**, 1564–1596.

[19] D. Chen, H. Feng and J. Li, *Chemical Reviews*, 2012, **112**, 6027–6053.

[20] I. Forbeaux, J. M. Themlin and J. M. Debever, *Physical Review B*, 1998, **58**, 16396–16406.

[21] C. Berger, Z. Song, T. Li, X. Li, A. Y. Ogbazghi, R. Feng, Z. Dai, A. N. Marchenkov, E. H. Conrad, P. N. First and W. A. de Heer, *The Journal of Physical Chemistry B*, 2004, **108**, 19912–19916.

[22] K. V. Emtsev, F. Speck, T. Seyller, L. Ley and J. D. Riley, *Phys. Rev. B*, 2008, **77**, 155303.

[23] K. V. Emtsev, A. Bostwick, K. Horn, J. Jobst, G. L. Kellogg, L. Ley, J. L. McChesney, T. Ohta, S. A. Reshanov, J. Rohrl, E. Rotenberg, A. K. Schmid, D. Waldmann, H. B. Weber and T. Seyller, *Nat Mater*, 2009, **8**, 203–207.

[24] A. Tzalenchuk, S. Lara-Avila, A. Kalaboukhov, S. Paolillo, M. Syvajarvi, R. Yakimova, O. Kazakova, T. J. B. M. Janssen, V. Fal'ko and S. Kubatkin, *Nat Nano*, 2010, **5**, 186–189.

[25] Y. Hernandez, V. Nicolosi, M. Lotya, F. M. Blighe, Z. Y. Sun, S. De, I. T. McGovern, B. Holland, M. Byrne, Y. K. Gun'ko, J. J. Boland, P. Niraj, G. Duesberg, S. Krishnamurthy, R. Goodhue, J. Hutchison, V. Scardaci, A. C. Ferrari and J. N. Coleman, *Nature Nanotechnology*, 2008, **3**, 563–568.

[26] U. Khan, A. O'Neill, M. Lotya, S. De and J. N. Coleman, *Small*, 2010, **6**, 864–871.

[27] U. Khan, H. Porwal, A. O'Neill, K. Nawaz, P. May and J. N. Coleman, *Langmuir*, 2011, **27**, 9077–82.

[28] H. Kim, A. A. Abdala and C. W. Macosko, *Macromolecules*, 2010, **43**, 6515–6530.

[29] S. Stankovich, D. A. Dikin, G. H. B. Dommett, K. M. Kohlhaas, E. J. Zimney, E. A. Stach, R. D. Piner, S. T. Nguyen and R. S. Ruoff, *Nature*, 2006, **442**, 282–286.

[30] S. Stankovich, D. A. Dikin, R. D. Piner, K. A. Kohlhaas, A. Kleinhammes, Y. Jia, Y. Wu, S. T. Nguyen and R. S. Ruoff, *Carbon*, 2007, **45**, 1558–1565.

[31] G. Eda, G. Fanchini and M. Chhowalla, *Nature Nanotechnology*, 2008, **3**, 270–274.

[32] D. Li, M. B. Muller, S. Gilje, R. B. Kaner and G. G. Wallace, *Nature Nanotechnology*, 2008, **3**, 101–105.

[33] Z. Yan, J. Lin, Z. W. Peng, Z. Z. Sun, Y. Zhu, L. Li, C. S. Xiang, E. L. Samuel, C. Kittrell and J. M. Tour, *Acs Nano*, 2012, **6**, 9110–9117.

[34] K. S. Kim, Y. Zhao, H. Jang, S. Y. Lee, J. M. Kim, K. S. Kim, J. H. Ahn, P. Kim, J. Y. Choi and B. H. Hong, *Nature*, 2009, **457**, 706–710.

[35] X. Li, W. Cai, J. An, S. Kim, J. Nah, D. Yang, R. Piner, A. Velamakanni, I. Jung, E. Tutuc, S. K. Banerjee, L. Colombo and R. S. Ruoff, *Science*, 2009, **324**, 1312–4.

[36] T. A. Land, T. Michely, R. J. Behm, J. C. Hemminger and G. Comsa, *Surface Science*, 1992, **264**, 261–270.

[37] J. Coraux, A. T. N'Diaye, C. Busse and T. Michely, *Nano Letters*, 2008, **8**, 565–570.

[38] J. Wintterlin and M. L. Bocquet, *Surface Science*, 2009, **603**, 1841–1852.

[39] S. Bae, H. Kim, Y. Lee, X. F. Xu, J. S. Park, Y. Zheng, J. Balakrishnan, T. Lei, H. R. Kim, Y. I. Song, Y. J. Kim, K. S. Kim, B. Ozyilmaz, J. H. Ahn, B. H. Hong and S. Iijima, *Nature Nanotechnology*, 2010, **5**, 574–578.

[40] C. Wirtz, K. Lee, T. Hallam and G. S. Duesberg, *Chemical Physics Letters*, 2014, **595**, 192–196.

[41] A. C. Ferrari, F. Bonaccorso, V. Fal'ko, K. S. Novoselov, S. Roche, P. Boggild, S. Borini, F. H. L. Koppens, V. Palermo, N. Pugno, J. A. Garrido, R. Sordan, A. Bianco, L. Ballerini, M. Prato, E. Lidorikis, J. Kivioja, C. Marinelli, T. Ryhanen, A. Morpurgo, J. N. Coleman, V. Nicolosi, L. Colombo, A. Fert, M. Garcia-Hernandez, A. Bachtold, G. F. Schneider, F. Guinea, C. Dekker, M. Barbone, Z. Sun, C. Galiotis, A. N. Grigorenko, G. Konstantatos, A. Kis, M. Katsnelson, L. Vandersypen, A. Loiseau, V. Morandi, D. Neumaier, E. Treossi, V. Pellegrini, M. Polini, A. Tredicucci, G. M. Williams, B. Hee Hong, J.-H. Ahn, J. Min Kim, H. Zirath, B. J. van Wees, H. van der Zant, L. Occhipinti, A. Di Matteo, I. A. Kinloch, T. Seyller, E. Quesnel, X. Feng, K. Teo, N. Rupesinghe, P. Hakonen, S. R. T. Neil, Q. Tannock, T. Lofwander and J. Kinaret, *Nanoscale*, 2015, **7**, 4598–4810.

[42] K. F. Mak, C. Lee, J. Hone, J. Shan and T. F. Heinz, *Physical Review Letters*, 2010, **105**, 136805.

[43] H. Li, Q. Zhang, C. C. R. Yap, B. K. Tay, T. H. T. Edwin, A. Olivier and D. Baillargeat, *Advanced Functional Materials*, 2012, **22**, 1385–1390.

[44] H. R. Gutiérrez, N. Perea-López, A. L. Elías, A. Berkdemir, B. Wang, R. Lv, F. López-Urías, V. H. Crespi, H. Terrones and M. Terrones, *Nano Letters*, 2013, **13**, 3447–3454.

[45] W. Zhao, Z. Ghorannevis, L. Chu, M. Toh, C. Kloc, P.-H. Tan and G. Eda, *ACS Nano*, 2013, **7**, 791–797.

[46] D. Jariwala, V. K. Sangwan, L. J. Lauhon, T. J. Marks and M. C. Hersam, *ACS Nano*, 2014, **8**, 1102–1120.

[47] R. Kappera, D. Voiry, S. E. Yalcin, B. Branch, G. Gupta, A. D. Mohite and M. Chhowalla, *Nat Mater*, 2014, **13**, 1128–1134.

[48] T. Roy, M. Tosun, J. S. Kang, A. B. Sachid, S. B. Desai, M. Hettick, C. C. Hu and A. Javey, *ACS Nano*, 2014, **8**, 6259–6264.

[49] R. J. Smith, P. J. King, M. Lotya, C. Wirtz, U. Khan, S. De, A. O'Neill, G. S. Duesberg, J. C. Grunlan, G. Moriarty, J. Chen, J. Z. Wang, A. I. Minett, V. Nicolosi and J. N. Coleman, *Advanced Materials*, 2011, **23**, 3944–3948.

[50] J. N. Coleman, M. Lotya, A. O'Neill, S. D. Bergin, P. J. King, U. Khan, K. Young, A. Gaucher, S. De, R. J. Smith, I. V. Shvets, S. K. Arora, G. Stanton, H. Y. Kim, K. Lee, G. T. Kim, G. S. Duesberg, T. Hallam, J. J. Boland, J. J. Wang, J. F. Donegan, J. C. Grunlan, G. Moriarty, A. Shmeliov, R. J. Nicholls, J. M. Perkins, E. M. Grieveson, K. Theuwissen, D. W. McComb, P. D. Nellist and V. Nicolosi, *Science*, 2011, **331**, 568–571.

[51] M. O'Brien, N. McEvoy, T. Hallam, H.-Y. Kim, N. C. Berner, D. Hanlon, K. Lee, J. N. Coleman and G. S. Duesberg, *Sci. Rep.*, 2014, **4**, 7374.

[52] R. Gatensby, N. McEvoy, K. Lee, T. Hallam, N. C. Berner, E. Rezvani, S. Winters, M. O'Brien and G. S. Duesberg, *Applied Surface Science*, 2014, **297**, 139–146.

[53] A. Splendiani, L. Sun, Y. Zhang, T. Li, J. Kim, C.-Y. Chim, G. Galli and F. Wang, *Nano Letters*, 2010, **10**, 1271–1275.

[54] C. Yim, M. O'Brien, N. McEvoy, S. Riazimehr, H. Schafer-Eberwein, A. Bablich, R. Pawar, G. Iannaccone, C. Downing, G. Fiori, M. C. Lemme and G. S. Duesberg, *Sci. Rep.*, 2014, **4**, 5458.

[55] F. H. L. Koppens, T. Mueller, P. Avouris, A. C. Ferrari, M. S. Vitiello and M. Polini, *Nat Nano*, 2014, **9**, 780–793.

[56] M. M. Furchi, D. K. Polyushkin, A. Pospischil and T. Mueller, *Nano Letters*, 2014, **14**, 6165–6170.

[57] S. Das, H.-Y. Chen, A. V. Penumatcha and J. Appenzeller, *Nano letters*, 2012, **13**, 100–105.

[58] M. Tosun, S. Chuang, H. Fang, A. B. Sachid, M. Hettick, Y. Lin, Y. Zeng and A. Javey, *ACS Nano*, 2014, **8**, 4948–4953.

[59] K. Lee, R. Gatensby, N. McEvoy, T. Hallam and G. S. Duesberg, *Advanced Materials*, 2013, **25**, 6699–6702.

[60] B. Liu, L. Chen, G. Liu, A. N. Abbas, M. Fathi and C. Zhou, *ACS Nano*, 2014, **8**, 5304–5314.

[61] N. V. Kozhemyakina, J. M. Englert, G. A. Yang, E. Spiecker, C. D. Schmidt, F. Hauke and A. Hirsch, *Advanced Materials*, 2010, **22**, 5483–5487.

[62] C. Backes, C. D. Schmidt, K. Rosenlehner, F. Hauke, J. N. Coleman and A. Hirsch, *Advanced Materials*, 2010, **22**, 788–802.

[63] C. C. Hofmann, S. M. Lindner, M. Ruppert, A. Hirsch, S. A. Haque, M. Thelakkat and J. Kohler, *Physical Chemistry Chemical Physics*, 2010, **12**, 14485–14491.

[64] C. Backes, F. Hauke and A. Hirsch, *Advanced Materials*, 2011, **23**, 2588–2601.

[65] A. Hirsch, J. M. Englert and F. Hauke, *Accounts of Chemical Research*, 2013, **46**, 87–96.

[66] R. C. Jaeger, *Introduction to Microelectronic Fabrication*, Prentice Hall, Upper Saddle River, New Jersey 07458, 2002, vol. 5.

[67] H. Ueta, M. Saida, C. Nakai, Y. Yamada, M. Sasaki and S. Yamamoto, *Surface Science*, 2004, **560**, 183–190.

[68] S. Kumar, N. McEvoy, T. Lutz, G. P. Keeley, V. Nicolosi, C. P. Murray, W. J. Blau and G. S. Duesberg, *Chemical Communications*, 2010, **46**, 1422–1424.

[69] A. Reina, X. T. Jia, J. Ho, D. Nezich, H. B. Son, V. Bulovic, M. S. Dresselhaus and J. Kong, *Nano Letters*, 2009, **9**, 30–35.

[70] R. S. Weatherup, B. C. Bayer, R. Blume, C. Ducati, C. Baehtz, R. Schlogl and S. Hofmann, *Nano Letters*, 2011, **11**, 4154–4160.

[71] R. S. Weatherup, C. Baehtz, B. Dlubak, B. C. Bayer, P. R. Kidambi, R. Blume, R. Schloegl and S. Hofmann, *Nano Letters*, 2013, **13**, 4624–4631.

[72] R. B. McLellan, *Scripta Metallurgica*, 1969, **3**, 389–391.

[73] M. Losurdo, M. M. Giangregorio, P. Capezzuto and G. Bruno, *Physical Chemistry Chemical Physics*, 2011, **13**, 20836–20843.

[74] G. H. Han, F. Gunes, J. J. Bae, E. S. Kim, S. J. Chae, H. J. Shin, J. Y. Choi, D. Pribat and Y. H. Lee, *Nano Lett*, 2011, **11**, 4144–8.

[75] E. Sperry, G. Scholl, P. Langdon, W. Meyer and A. Bregman, *Metal Finishing: Preparation, Electroplating, Coating*, Metal Industry Publishing Company, 1949.

[76] Y. Zhang, Z. Li, P. Kim, L. Y. Zhang and C. W. Zhou, *Acs Nano*, 2012, **6**, 126–132.

[77] Z. T. Luo, Y. Lu, D. W. Singer, M. E. Berck, L. A. Somers, B. R. Goldsmith and A. T. C. Johnson, *Chemistry of Materials*, 2011, **23**, 1441–1447.

[78] A. Srivastava, C. Galande, L. Ci, L. Song, C. Rai, D. Jariwala, K. F. Kelly and P. M. Ajayan, *Chemistry of Materials*, 2010, **22**, 3457–3461.

[79] Y. Yao, Z. Li, Z. Lin, K.-S. Moon, J. Agar and C. Wong, *The Journal of Physical Chemistry C*, 2011, **115**, 5232–5238.

[80] A. Guermoune, T. Chari, F. Popescu, S. S. Sabri, J. Guillemette, H. S. Skulason, T. Szkopek and M. Siaj, *Carbon*, 2011, **49**, 4204–4210.

[81] J. Chan, A. Venugopal, A. Pirkle, S. McDonnell, D. Hinojos, C. W. Magnuson, R. S. Ruoff, L. Colombo, R. M. Wallace and E. M. Vogel, *Acs Nano*, 2012, **6**, 3224–3229.

[82] P. R. Kidambi, B. C. Bayer, R. Blume, Z.-J. Wang, C. Baehtz, R. S. Weatherup, M.-G. Willinger, R. Schloegl and S. Hofmann, *Nano Letters*, 2013, **13**, 4769–4778.

[83] J. W. Suk, A. Kitt, C. W. Magnuson, Y. F. Hao, S. Ahmed, J. H. An, A. K. Swan, B. B. Goldberg and R. S. Ruoff, *Acs Nano*, 2011, **5**, 6916–6924.

[84] T. Hallam, N. C. Berner, C. Yim and G. S. Duesberg, *Advanced Materials Interfaces*, 2014, **1**, n/a–n/a.

[85] S. Kumar, E. Rezvani, V. Nicolosi and G. S. Duesberg, *Nanotechnology*, 2012, **23**, 145302.

[86] T. Dieing, O. Hollricher and J. Toporski, *Confocal Raman Spectroscopy*, Springer Berlin - Heidelberg, 2011, vol. 158.

[87] J. Filik, *Spectroscopy Europe*, 2005, **17**, 10.

[88] A. C. Ferrari, J. C. Meyer, V. Scardaci, C. Casiraghi, M. Lazzeri, F. Mauri, S. Piscanec, D. Jiang, K. S. Novoselov, S. Roth and A. K. Geim, *Physical Review Letters*, 2006, **97**, 187401.

[89] A. C. Ferrari, *Solid State Communications*, 2007, **143**, 47–57.

[90] A. Das, S. Pisana, B. Chakraborty, S. Piscanec, S. K. Saha, U. V. Waghmare, K. S. Novoselov, H. R. Krishnamurthy, A. K. Geim, A. C. Ferrari and A. K. Sood, *Nature Nanotechnology*, 2008, **3**, 210–215.

[91] C. Casiraghi, A. Hartschuh, H. Qian, S. Piscanec, C. Georgi, A. Fasoli, K. S. Novoselov, D. M. Basko and A. C. Ferrari, *Nano Letters*, 2009, **9**, 1433–1441.

[92] Y. y. Wang, Z. h. Ni, T. Yu, Z. X. Shen, H. m. Wang, Y. h. Wu, W. Chen and A. T. Shen Wee, *The Journal of Physical Chemistry C*, 2008, **112**, 10637–10640.

[93] D. Graf, F. Molitor, K. Ensslin, C. Stampfer, A. Jungen, C. Hierold and L. Wirtz, *Nano Letters*, 2007, **7**, 238–242.

[94] A. C. Ferrari and D. M. Basko, *Nat Nano*, 2013, **8**, 235–246.

[95] J. L. Verble and T. J. Wieting, *Phys. Rev. Lett.*, 1970, **25**, 362–365.

[96] T. J. Wieting and J. L. Verble, *Phys. Rev. B*, 1971, **3**, 4286–4292.

[97] X. Zhang, W. P. Han, J. B. Wu, S. Milana, Y. Lu, Q. Q. Li, A. C. Ferrari and P. H. Tan, *Physical Review B*, 2013, **87**, 115413.

[98] L. Yang, X. Cui, J. Zhang, K. Wang, M. Shen, S. Zeng, S. A. Dayeh, L. Feng and B. Xiang, *Sci. Rep.*, 2014, **4**, 5649.

[99] B. Chakraborty, A. Bera, D. V. S. Muthu, S. Bhowmick, U. V. Waghmare and A. K. Sood, *Physical Review B*, 2012, **85**, 161403.

[100] A. Otto, in *Surface-enhanced Raman scattering: "Classical" and "Chemical" origins*, ed. M. Cardona and G. Güntherodt, Springer Berlin Heidelberg, 1984, vol. 54, ch. 6, pp. 289–418.

[101] B. Ren, Q. J. Huang, W. B. Cai, B. W. Mao, F. M. Liu and Z. Q. Tian, *Journal of Electroanalytical Chemistry*, 1996, **415**, 175–178.

[102] Z. Q. Tian, B. Ren and D. Y. Wu, *Journal of Physical Chemistry B*, 2002, **106**, 9463–9483.

[103] S. M. Nie and S. R. Emery, *Science*, 1997, **275**, 1102–1106.

[104] E. C. Le Ru, M. Meyer and P. G. Etchegoin, *Journal of Physical Chemistry B*, 2006, **110**, 1944–1948.

[105] E. C. Le Ru, E. Blackie, M. Meyer and P. G. Etchegoin, *Journal of Physical Chemistry C*, 2007, **111**, 13794–13803.

[106] E. J. Blackie, E. C. Le Ru and P. G. Etchegoin, *Journal of the American Chemical Society*, 2009, **131**, 14466–14472.

[107] G. Duesberg, W. Blau, H. Byrne, J. Muster, M. Burghard and S. Roth, *Chemical Physics Letters*, 1999, **310**, 8 – 14.

[108] G. Schatz, M. Young and R. Van Duyne, in *Electromagnetic Mechanism of SERS*, ed. K. Kneipp, M. Moskovits and H. Kneipp, Springer Berlin Heidelberg, 2006, vol. 103, ch. 2, pp. 19–45.

[109] E. B. Barros and M. S. Dresselhaus, *Physical Review B*, 2014, **90**, 035443.

[110] L. Ju, B. Geng, J. Horng, C. Girit, M. Martin, Z. Hao, H. A. Bechtel, X. Liang, A. Zettl, Y. R. Shen *et al.*, *Nature nanotechnology*, 2011, **6**, 630–634.

[111] J. R. Lombardi, R. L. Birke, T. H. Lu and J. Xu, *Journal of Chemical Physics*, 1986, **84**, 4174–4180.

[112] M. Kalbac, H. Farhat, J. Kong, P. Janda, L. Kavan and M. S. Dresselhaus, *Nano Letters*, 2011, **11**, 1957–1963.

[113] D. Basko, *New Journal of Physics*, 2009, **11**, 095011.

[114] X. Ling, W. Fang, Y.-H. Lee, P. T. Araujo, X. Zhang, J. F. Rodriguez-Nieva, Y. Lin, J. Zhang, J. Kong and M. S. Dresselhaus, *Nano Letters*, 2014, **14**, 3033–3040.

[115] S. Huang, X. Ling, L. Liang, Y. Song, W. Fang, J. Zhang, J. Kong, V. Meunier and M. S. Dresselhaus, *Nano Letters*, 2015, **15**, 2892–2901.

[116] X. Ling, J. Wu, L. Xie and J. Zhang, *The Journal of Physical Chemistry C*, 2013, **117**, 2369–2376.

[117] X. Ling and J. Zhang, *Small*, 2010, **6**, 2020–2025.

[118] X. X. Yu, H. B. Cai, W. H. Zhang, X. J. Li, N. Pan, Y. Luo, X. P. Wang and J. G. Hou, *Acs Nano*, 2011, **5**, 952–958.

[119] S. Huh, J. Park, Y. S. Kim, K. S. Kim, B. H. Hong and J. M. Nam, *Acs Nano*, 2011, **5**, 9799–9806.

[120] X. Ling, J. X. Wu, W. G. Xu and J. Zhang, *Small*, 2012, **8**, 1365–1372.

[121] P. J. Goodhew, J. Humphreys and R. Beanland, *Electron microscopy and analysis*, CRC Press, 2000.

[122] M. Prutton, *Introduction to surface physics*, Clarendon Press, 1994.

[123] D. Woodruff and T. Delchar, *Modern Techniques of Surface Science*, Cambridge University Press, 1994.

[124] H. Hertz, *Annalen der Physik*, 1887, **267**, 983–1000.

[125] A. Einstein, *Annalen der Physik*, 1905, **322**, 132–148.

[126] A. Atkinson, A. Donev and R. Tobias, *Optimum Experimental Designs, With SAS*, OUP Oxford, 2007, vol. 34, p. 511.

[127] G. Binnig, C. F. Quate and C. Gerber, *Phys. Rev. Lett.*, 1986, **56**, 930–933.

[128] A. Fick, *Annalen der Physik*, 1855, **170**, 59–86.

[129] K. Müllen and U. Scherf, *Organic Light Emitting Devices: Synthesis, Properties and Applications*, Wiley, 2006.

[130] J. Meyer, P. R. Kidambi, B. C. Bayer, C. Weijtens, A. Kuhn, A. Centeno, A. Pesquera, A. Zurutuza, J. Robertson and S. Hofmann, *Scientific Reports*, 2014, **4**, 5380.

[131] Y. Wang, X. Chen, Y. Zhong, F. Zhu and K. P. Loh, *Applied Physics Letters*, 2009, **95**, –.

[132] H. Park, P. R. Brown, V. Bulović and J. Kong, *Nano Letters*, 2012, **12**, 133–140.

[133] Y. Wang, S. W. Tong, X. F. Xu, B. Ozyilmaz and K. P. Loh, *Advanced Materials*, 2011, **23**, 1514–1518.

[134] A. Kuruvila, P. R. Kidambi, J. Kling, J. B. Wagner, J. Robertson, S. Hofmann and J. Meyer, *J. Mater. Chem. C*, 2014, **2**, 6940–6945.

[135] J. Wu, M. Agrawal, H. A. Becerril, Z. Bao, Z. Liu, Y. Chen and P. Peumans, *ACS Nano*, 2010, **4**, 43–48.

[136] T. Sun, Z. L. Wang, Z. J. Shi, G. Z. Ran, W. J. Xu, Z. Y. Wang, Y. Z. Li, L. Dai and G. G. Qin, *Applied Physics Letters*, 2010, **96**, –.

[137] T. H. Han, Y. Lee, M. R. Choi, S. H. Woo, S. H. Bae, B. H. Hong, J. H. Ahn and T. W. Lee, *Nature Photonics*, 2012, **6**, 105–110.

[138] R. K. Singh Raman, P. Chakraborty Banerjee, D. E. Lobo, H. Gullapalli, M. Sumandasa, A. Kumar, L. Choudhary, R. Tkacz, P. M. Ajayan and M. Majumder, *Carbon*, 2012, **50**, 4040–4045.

[139] D. Prasai, J. C. Tuberquia, R. R. Harl, G. K. Jennings and K. I. Bolotin, *Acs Nano*, 2012, **6**, 1102–1108.

[140] X. Wang, L. J. Zhi and K. Mullen, *Nano Letters*, 2008, **8**, 323–327.

[141] N. Petrone, C. R. Dean, I. Meric, A. M. van der Zande, P. Y. Huang, L. Wang, D. Muller, K. L. Shepard and J. Hone, *Nano Lett*, 2012, **12**, 2751–6.

[142] G. A. Lopez and E. Mittemeijer, *Scripta Materialia*, 2004, **51**, 1–5.

[143] X. Li, C. W. Magnuson, A. Venugopal, R. M. Tromp, J. B. Hannon, E. M. Vogel, L. Colombo and R. S. Ruoff, *Journal of the American Chemical Society*, 2011, **133**, 2816–2819.

[144] H. N. Hersh, *Journal of the American Chemical Society*, 1953, **75**, 1529–1531.

[145] W. M. Haynes, *CRC handbook of chemistry and physics*, CRC press, 2014.

[146] B. Zhang, W. H. Lee, R. Piner, I. Kholmanov, Y. Wu, H. Li, H. Ji and R. S. Ruoff, *Acs Nano*, 2012, **6**, 2471–2476.

[147] Z. C. Li, P. Wu, C. X. Wang, X. D. Fan, W. H. Zhang, X. F. Zhai, C. G. Zeng, Z. Y. Li, J. L. Yang and J. G. Hou, *Acs Nano*, 2011, **5**, 3385–3390.

[148] N. S. Safron, M. Kim, P. Gopalan and M. S. Arnold, *Advanced Materials*, 2012, **24**, 1041–1045.

[149] G. Aichmayr, A. Avellan, G. S. Duesberg, F. Kreupl, S. Kudelka and M. Liebau, VLSI Technology, 2007 IEEE Symposium on, 2007, pp. 186–187.

[150] A. Kukovecz, D. Méhn, E. Nemes-Nagy, R. Szabó and I. Kiricsi, *Carbon*, 2005, **43**, 2842–2849.

[151] L. Cançado, A. Reina, J. Kong and M. Dresselhaus, *Physical Review B*, 2008, **77**, 245408.

[152] J. S. Park, A. Reina, R. Saito, J. Kong, G. Dresselhaus and M. S. Dresselhaus, *Carbon*, 2009, **47**, 1303–1310.

[153] F. Tuinstra and J. L. Koenig, *Journal of Chemical Physics*, 1970, **53**, 1126–1130.

[154] A. Pirkle, J. Chan, A. Venugopal, D. Hinojos, C. W. Magnuson, S. McDonnell, L. Colombo, E. M. Vogel, R. S. Ruoff and R. M. Wallace, *Applied Physics Letters*, 2011, **99**, 122108.

[155] N. Peltekis, S. Kumar, N. McEvoy, K. Lee, A. Weidlich and G. S. Duesberg, *Carbon*, 2012, **50**, 395–403.

[156] K. Lee, H.-Y. Kim, M. Lotya, J. N. Coleman, G.-T. Kim and G. S. Duesberg, *Advanced Materials*, 2011, **23**, 4178–4182.

[157] O. V. Yazyev and S. G. Louie, *Nature Materials*, 2010, **9**, 806–809.

[158] N. M. R. Peres, F. Guinea and A. H. C. Neto, *Physical Review B*, 2006, **73**, 125411.

[159] A. W. Tsen, L. Brown, M. P. Levendorf, F. Ghahari, P. Y. Huang, R. W. Havener, C. S. Ruiz-Vargas, D. A. Muller, P. Kim and J. Park, *Science*, 2012, **336**, 1143–1146.

[160] C. Wirtz, N. C. Berner and G. S. Duesberg, *Advanced Materials Interfaces*, 2015, n/a–n/a.

[161] R. Sack, *Human Territoriality: Its Theory and History*, Cambridge University Press, 1986.

[162] O. Leenaerts, B. Partoens and F. M. Peeters, *Applied Physics Letters*, 2008, **93**, 193107.

[163] H. Kim, Y. Miura and C. W. Macosko, *Chemistry of Materials*, 2010, **22**, 3441–3450.

[164] H. D. Huang, P. G. Ren, J. Chen, W. Q. Zhang, X. Ji and Z. M. Li, *Journal of Membrane Science*, 2012, **409**, 156–163.

[165] Y.-H. Yang, L. Bolling, M. A. Priolo and J. C. Grunlan, *Advanced Materials*, 2013, **25**, 503–508.

[166] H. W. Kim, H. W. Yoon, S.-M. Yoon, B. M. Yoo, B. K. Ahn, Y. H. Cho, H. J. Shin, H. Yang, U. Paik, S. Kwon, J.-Y. Choi and H. B. Park, *Science*, 2013, **342**, 91–95.

[167] K. Choi, S. Nam, Y. Lee, M. Lee, J. Jang, S. J. Kim, Y. J. Jeong, H. Kim, S. Bae, J.-B. Yoo, S. M. Cho, J.-B. Choi, H. K. Chung, J.-H. Ahn, C. E. Park and B. H. Hong, *ACS Nano*, 2015, **9**, 5818–5824.

[168] T. Masuda, E. Isobe, T. Higashimura and K. Takada, *Journal of the American Chemical Society*, 1983, **105**, 7473–7474.

[169] G. L. Graff, R. E. Williford and P. E. Burrows, *Journal of Applied Physics*, 2004, **96**, 1840–1849.

[170] V. Siracusa, *International Journal of Polymer Science*, 2012, **2012**, 11.

[171] T.-C. Chen, J. B. Hannon, N. Li, S. Oida, D. K. Sadana and G. S. Tulevski, *Doped graphene transparent conductive electrode*, 2012, US Patent App. 13/626,411.

[172] H.-j. Shin, J.-Y. Choi, J.-r. Ahn and J.-t. Seo, *Graphene-layered structure, method of preparing the same, and transparent electrode and transistor including graphene-layered structure*, 2014, US Patent 8,679,951.

[173] T. G. Kim and H.-D. Kim, *Organic light emitting device having transparent electrode where conducting filaments formed and method of manufacturing the same*, 2013, US Patent App. 14/429,439.

[174] B. Özyilmaz, G. X. Ni and Y. Zheng, *Transparent conductor*, 2011, US Patent App. 13/882,451.

[175] J. Hwang, H. Kyw Choi, J. Moon, T. Yong Kim, J.-W. Shin, C. Woong Joo, J.-H. Han, D.-H. Cho, J. Woo Huh, S.-Y. Choi, J.-I. Lee and H. Yong Chu, *Applied Physics Letters*, 2012, **100**, –.

[176] H. Chatham, *Surface and Coatings Technology*, 1996, **78**, 1–9.

[177] S. Cros, M. Firon, S. Lenfant, P. Trouslard and L. Beck, *Nuclear Instruments and Methods in Physics Research Section B: Beam Interactions with Materials and Atoms*, 2006, **251**, 257 – 260.

[178] J. S. Lewis and M. S. Weaver, *Selected Topics in Quantum Electronics, IEEE Journal of*, 2004, **10**, 45–57.

[179] N. Inagaki, S. Tasaka and H. Hiramatsu, *Journal of Applied Polymer Science*, 1999, **71**, 2091–2100.

[180] D.-Y. Wang, I.-S. Huang, P.-H. Ho, S.-S. Li, Y.-C. Yeh, D.-W. Wang, W.-L. Chen, Y.-Y. Lee, Y.-M. Chang, C.-C. Chen, C.-T. Liang and C.-W. Chen, *Advanced Materials*, 2013, **25**, 4521–4526.

[181] M. Q. Tian, M. Furuki, I. Iwasa, Y. Sato, L. S. Pu and S. Tatsuura, *Journal of Physical Chemistry B*, 2002, **106**, 4370–4376.

[182] S. Winters, N. C. Berner, R. Mishra, K. C. Dumbgen, C. Backes, M. Hegner, A. Hirsch and G. S. Duesberg, *Chem. Commun.*, 2015, –.

[183] N. C. Berner, S. Winters, C. Backes, C. Yim, K. C. Dumbgen, I. Kaminska, S. Mackowski, A. A. Cafolla, A. Hirsch and G. S. Duesberg, *Nanoscale*, 2015, **7**, 16337–16342.

[184] L. M. Malard, M. A. Pimenta, G. Dresselhaus and M. S. Dresselhaus, *Physics Reports*, 2009, **473**, 51–87.

[185] C. Wirtz, T. Hallam, C. P. Cullen, N. C. Berner, M. O'Brien, M. Marcia, A. Hirsch and G. S. Duesberg, *Chem. Commun.*, 2015, –.

[186] Y. Gong, J. Lin, X. Wang, G. Shi, S. Lei, Z. Lin, X. Zou, G. Ye, R. Vajtai, B. I. Yakobson, H. Terrones, M. Terrones, B. Tay, J. Lou, S. T. Pantelides, Z. Liu, W. Zhou and P. M. Ajayan, *Nat Mater*, 2014, **13**, 1135–1142.

[187] X. Duan, C. Wang, J. C. Shaw, R. Cheng, Y. Chen, H. Li, X. Wu, Y. Tang, Q. Zhang, A. Pan, J. Jiang, R. Yu, Y. Huang and X. Duan, *Nat Nano*, 2014, **9**, 1024–1030.

[188] A. M. van der Zande, P. Y. Huang, D. A. Chenet, T. C. Berkelbach, Y. You, G.-H. Lee, T. F. Heinz, D. R. Reichman, D. A. Muller and J. C. Hone, *Nat Mater*, 2013, **12**, 554–561.

[189] B. Visic, R. Dominko, M. K. Gunde, N. Hauptman, S. D. Skapin and M. Remskar, *Nanoscale research letters*, 2011, **6**, 1–6.

[190] S. M. George, *Chemical Reviews*, 2010, **110**, 111–131.

[191] R. L. Puurunen, *Journal of Applied Physics*, 2005, **97**, 121301.

[192] H. Liu, K. Xu, X. Zhang and P. D. Ye, *Applied Physics Letters*, 2012, **100**, 152115.

[193] J. Yang, S. Kim, W. Choi, S. H. Park, Y. Jung, M. H. Cho and H. Kim, *Acs Applied Materials & Interfaces*, 2013, **5**, 4739–4744.

[194] L. X. Cheng, X. Y. Qin, A. T. Lucero, A. Azcatl, J. Huang, R. M. Wallace, K. Cho and J. Kim, *Acs Applied Materials & Interfaces*, 2014, **6**, 11834–11838.

[195] X. R. Wang, S. M. Tabakman and H. J. Dai, *Journal of the American Chemical Society*, 2008, **130**, 8152–8153.

[196] B. Dlubak, P. R. Kidambi, R. S. Weatherup, S. Hofmann and J. Robertson, *Applied Physics Letters*, 2012, **100**, 173113.

[197] M.-B. Martin, B. Dlubak, R. S. Weatherup, H. Yang, C. Deranlot, K. Bouzehouane, F. Petroff, A. Anane, S. Hofmann, J. Robertson, A. Fert and P. Seneor, *ACS Nano*, 2014, **8**, 7890–7895.

[198] J. M. P. Alaboson, Q. H. Wang, J. D. Emery, A. L. Lipson, M. J. Bedzyk, J. W. Elam, M. J. Pellin and M. C. Hersam, *ACS Nano*, 2011, **5**, 5223–5232.

[199] M. Li, M. Dai and Y. J. Chabal, *Langmuir*, 2009, **25**, 1911–1914.

[200] Y. Obeng, *Graphene and Emerging Materials for Post-CMOS Applications*, Electrochemical Society, 2009.

[201] A. M. Goldberg, A. R. Beal, F. A. Lévy and E. A. Davis, *Philosophical Magazine*, 1975, **32**, 367–378.

[202] A. L. Elías, N. Perea-López, A. Castro-Beltrán, A. Berkdemir, R. Lv, S. Feng, A. D. Long, T. Hayashi, Y. A. Kim, M. Endo, H. R. Gutiérrez, N. R. Pradhan, L. Balicas, T. E. Mallouk, F. López-Urías, H. Terrones and M. Terrones, *ACS Nano*, 2013, **7**, 5235–5242.

[203] X. R. Wang, S. M. Tabakman and H. J. Dai, *Journal of the American Chemical Society*, 2008, **130**, 8152–8153.

[204] M. Marcia, P. Singh, F. Hauke, M. Maggini and A. Hirsch, *Org. Biomol. Chem.*, 2014, **12**, 7045–7058.

[205] Y. Shi, J.-K. Huang, L. Jin, Y.-T. Hsu, S. F. Yu, L.-J. Li and H. Y. Yang, *Sci. Rep.*, 2013, **3**, 1839.